

One-dimensional Bose gas on an atom chip

One-dimensional Bose gas on an atom chip >> Aaldert van Amerongen >> 2008

>> Aaldert van Amerongen

Uitnodiging

Voor het bijwonen van
de openbare verdediging
van mijn proefschrift

One-dimensional Bose gas on an atom chip

Vrijdag 30 mei
14.00 uur

Paranimfen: Tesse Stek en
Michelangelo Vargas-Rivera

In de Agnietenkapel van de
Universiteit van Amsterdam

Oudezijds Voorburgwal 231

Na afloop is er een receptie

>> Aaldert van Amerongen
Tweede Jan Steenstraat 11E
1073 VK Amsterdam
06 12754451

One-dimensional Bose gas
on an atom chip

One-dimensional Bose gas on an atom chip

ACADEMISCH PROEFSCHRIFT

ter verkrijging van de graad van doctor
aan de Universiteit van Amsterdam
op gezag van de Rector Magnificus
prof. dr. D.C. van den Boom
ten overstaan van een door het college voor promoties ingestelde
commissie, in het openbaar te verdedigen in de Agnietenkapel
op vrijdag 30 mei 2008, te 14:00 uur

door

Aaldert Hidde van Amerongen

geboren te Amsterdam

Promotiecommissie:

Promotor: prof. dr. J.T.M. Walraven
Copromotor: dr. N.J. van Druten

Overige leden: prof. dr. A. Aspect
prof. dr. M.S. Golden
prof. dr. H.B. van Linden van den Heuvell
prof. dr. K.J. Schoutens
prof. dr. G.V. Shlyapnikov
dr. R.J.C. Spreeuw
prof. dr. P. van der Straten

Faculteit der Natuurwetenschappen, Wiskunde en Informatica

ISBN: 978-90-9022841-9

The work described in this thesis was carried out in the group “Quantum Gases & Quantum Information”, at the Van der Waals-Zeeman Instituut of the University of Amsterdam, Valckenierstraat 65, 1018 XE Amsterdam, The Netherlands, where a limited number of copies of this thesis is available.

A digital version of this thesis can be downloaded from <http://www.science.uva.nl/research/aplp>

Funding was also provided by NWO (VIDI grant N.J. van Druten), FOM (Projectruimte and program 'Quantum Gases') and the EU (Marie Curie Research and Training Network 'Atom Chips').

Contents

1	Introduction	1
1.1	1D Bose gas	1
1.2	Integrated atom optics	3
1.3	This thesis	4
2	Theoretical background	5
2.1	Introduction	5
2.2	Magnetic trapping	6
2.3	Ideal Bose gas	8
2.3.1	Ideal Bose gas harmonically trapped in 3D and 1D	10
2.3.2	Ideal Bose gas in the 3D-1D cross-over	11
2.4	Weakly interacting (quasi-)condensate	11
2.4.1	Mean-field 3D	12
2.4.2	Mean-field 1D	13
2.4.3	Mean-field 3D-1D crossover	13
2.4.4	Excitations in elongated quasi-condensates	14
2.5	Exact solutions in 1D	15
2.5.1	Tonks-Girardeau	15
2.5.2	Lieb-Liniger	17
2.5.3	Yang-Yang	18
2.6	Overview of ultracold Bose gas regimes	20
2.6.1	Regimes for $T = 0$	20
2.6.2	Regimes in 1D	21
2.7	Previous models for $T > 0$	22
2.7.1	Semi-ideal Bose gas	22
2.7.2	Self-consistent Hartree-Fock	22
2.8	Evaporative cooling	23
3	Experimental Setup	27
3.1	Introduction	27
3.2	Design considerations	28
3.3	Microtrap for cold atoms	31
3.3.1	Layout and construction	33
3.4	Thermal properties of the microtrap	37
3.4.1	Thermal conduction – analytic approach	38
3.4.2	Thermal conduction – Finite Element Method	40
3.5	Vacuum system	42
3.6	Dispenser pulsed atom source	44

3.7	Magnetic field coils	46
3.8	Lasers	48
3.9	Imaging system	51
3.10	Experimental control	54
	3.10.1 Output control	55
	3.10.2 Radio frequency source	55
3.11	Concluding remarks	56
4	Realizing Bose-Einstein condensation	57
4.1	Introduction	57
4.2	Trapping and cooling sequence	57
	4.2.1 MOT	58
	4.2.2 Compressed MOT	58
	4.2.3 Optical pumping	59
	4.2.4 Minitrap	59
	4.2.5 Z-trap – compression	60
	4.2.6 Reaching BEC by evaporative cooling	60
	4.2.7 BEC in the 3D-1D cross-over	61
4.3	Potential roughness	62
5	Focusing phase-fluctuating condensates	65
5.1	Introduction	65
5.2	Gaussian and nonideal optical beams and ABCD matrices	67
	5.2.1 Paraxial wave equation and Huygens-Fresnel integral	67
	5.2.2 Nonideal beam	69
5.3	Atom optics and ABCD matrices	70
	5.3.1 Schrödinger equation and Wigner function	70
	5.3.2 ABCD matrices for matter waves	72
	5.3.3 Temperature of a focused non-interacting gas	76
5.4	Quasi-condensate as nonideal atomic beam	77
5.5	Weakly interacting condensate in a time dependent trap	79
5.6	Experiments	82
5.7	Discussion	87
5.8	Conclusion and outlook	89
6	Yang-Yang thermodynamics on an atom chip	91
6.1	Introduction	91
6.2	Methods	93
6.3	<i>In situ</i> density profiles	93
6.4	<i>In focus</i> density profiles	94
6.5	Analysis and discussion	95
6.6	Conclusion and outlook	96
	References	99

Summary	111
Samenvatting	113
Nawoord	115

1 Introduction

A Bose-Einstein condensate can be viewed as a macroscopic quantum mechanical matter-wave. The constituent bosons (particles with integer spin) are cold enough to let their de Broglie wavelengths overlap. As a result of Bose statistics [1, 2] the system has gone through a phase transition: The particles gather in a single quantum ground state and act coherently. Bose-Einstein condensation (BEC) is related to superfluidity and to superconductivity. Superconductivity, vanishing electrical resistance in a conductor at low temperature, was discovered by Kamerlingh-Onnes [3] as a result of his development of advanced cooling techniques that led to the liquefaction of helium in 1908 [4]. It was Kapitza who first used the term superfluidity to characterize the frictionless flow observed in liquid helium below a temperature of 2.2 K (known as the λ -point), observed by him [5] and separately by Allen and Misener [6] in 1938. That same year also marked the start of vivid developments in theory when Fritz London [7] hypothesized on a relation between the behavior of liquid helium below the λ -point and BEC, and Tisza [8] connected BEC to superfluidity, for a review see [9]. Important steps towards cooling matter to even lower temperatures were made in the 1980s [10–12] with the development of magnetic trapping and evaporative cooling techniques for atomic hydrogen.

In 1995, after the introduction of laser cooling for alkali atoms [13–16], Bose-Einstein condensates of rubidium and sodium in the gas phase were realized [17, 18]. The crisp images of these macroscopic matter-waves generated huge enthusiasm amongst experimental and theoretical physicists. In the same year, also evidence for BEC in Li was reported [19] (see also [20–22]). This was especially intriguing because it showed that in a trap a BEC with *attractive* interactions can be stable, unlike the situation for a uniform gas. Experiments on Bose-Einstein condensates provide ample possibility to develop and test theory for macroscopic quantum phenomena also relevant for the description of superfluidity and superconductivity [7, 23–25].

1.1 1D Bose gas

The key ingredient for the quantum phenomena of BEC, superfluidity and superconductivity is long-range order of the phase of the macroscopic wavefunction (see [25, 26] and [27] p.31). Long-range order appears in a three-dimensional homogeneous system of bosons at finite temperature. Mermin and Wagner [28] and

Hohenberg [29] proved that in lower-dimensional systems the situation is significantly different: In two dimensions (2D) phase coherence does only exist at $T = 0$ and in one dimension (1D) phase order decays algebraically even at zero temperature. From these considerations it was established that BEC at finite temperature does not exist in 2D and 1D. The study of lower-dimensional quantum degenerate systems could promote better understanding of often complex ordering phenomena and was therefore pursued in experiments soon after the first alkali BEC's were realized. For example in 2D the locally coherent Bose gas supports vortex-antivortex pairs whose unbinding leads to the Kosterlitz-Thouless transition [30]. Experimentally, lower dimensional systems can be realized by strongly confining atoms to their motional ground state in one or two dimensions using magnetic or optical trapping, while applying a very weak harmonic potential in the residual dimension(s).

In contrast to the homogeneous case, BEC in 2D and 1D does occur in a trap [31]. Ketterle and van Druten [32] studied lower-dimensional systems of a finite number of non-interacting bosons, in the presence of external harmonic confinement and found that the transition temperature increases for lower dimensions. For experimentally realistic parameters, one-dimensionally trapped atoms exhibit interactions. These interactions in 1D can be modelled using the 3D atomic scattering length [33]. Petrov, Shlyapnikov and Walraven [34] included atomic interactions in their description and identified several, at that time experimentally unexplored, regimes of quantum degeneracy in trapped 1D gases. The 1D Bose gas is of particular interest because exact solutions for the many-body eigenstates can be obtained [35]. Furthermore, the finite-temperature equilibrium can be studied using the exact Yang-Yang thermodynamic formalism [36–38], a method also known as the thermodynamic Bethe Ansatz. The 1D regime in ultracold atomic Bose gases was first reached in experiments in the year 2001 [39–41]. Peculiarly, in 1D atoms become more *strongly* interacting for *decreasing* density. In the low density limit one has a Tonks-Girardeau gas of impenetrable bosons that was first realized using optical trapping in 2004 [42, 43].

In the experiments described in this thesis we magnetically trap atoms in a tube-like geometry. This ‘waveguide’ for atoms is created using the magnetic field from current carrying wires on a microchip. Using this ‘atom chip’ [44, 45] we realize a trapped one-dimensional Bose gas in the weakly interacting regime. Due to the finite-temperature we have a system that can be described as a degenerate 1D gas in thermal contact with a surrounding 3D thermal gas. Even for the lowest temperatures reached (~ 100 nK) finite-temperature effects reduce the phase coherence and we observe a BEC with a fluctuating phase. When we lower the atomic density, at constant temperature, the system becomes more strongly interacting and reduction of the phase-order destroys the condensate. We observe in this process, for the first time, a gas that obeys the exact Yang-Yang thermodynamics [46].

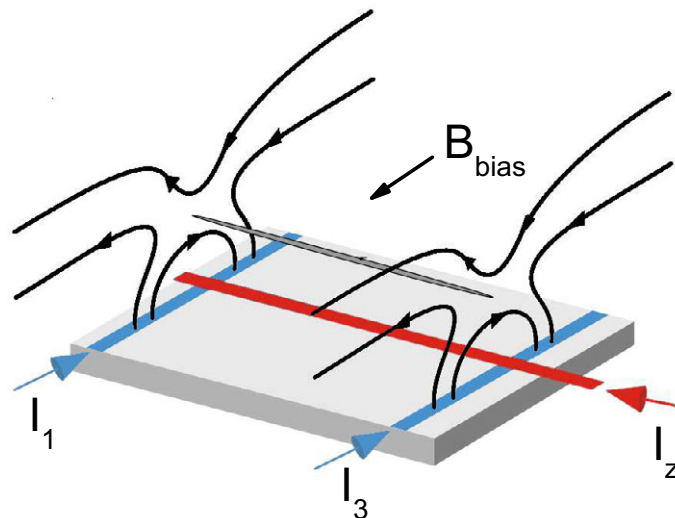


Figure 1.1: Waveguide potential for atoms. A waveguide is created when the circular magnetic field of a chip wire (I) is compensated with a perpendicular bias magnetic field B_{bias} . Three-dimensional confinement is achieved by creating end-caps with currents I_1 and I_3 .

1.2 Integrated atom optics

Rapid developments in microfabrication techniques enable spectacular advances in fundamental physics. The ‘atom-chip’ [44,45] is an example of a device that enables us to manipulate matter waves on the nanometer scale using integrated circuits. The idea of an atom chip was launched in 1995 by Weinstein and Libbrecht [47], the authors proposed to trap ultracold atoms in the magnetic field of micropatterned conductors, thus having them hover only micrometers away from the chip surface. Thermal insulation of the ultracold atoms is assured by placing the chip in an ultra high vacuum environment. Later that same year, the first BECs in atomic gases [17,18] were realized using large electromagnet-based traps. In 2001 two groups independently made a next step and created a BEC on a chip [44,45]. With the realization of an atomic matter wave on a chip the field of ‘integrated atom optics’ was born. At the time of writing more than a dozen labs worldwide do experiments with BECs on a chip, for a recent review see [48]. An introductory account of the Amsterdam work on atom chips can be found in [49].

Atoms can be magnetically trapped when their magnetic moment is anti-parallel to the local magnetic field. The trapping potential is proportional to the magnetic field strength. The simplest chip trap is a waveguide, illustrated in Fig. 1.1, that is created when the circular magnetic field of a chip wire (I) is compensated with a perpendicular bias magnetic field. End-caps are realized with currents I_1 and I_3 . With short distances between the trapped atoms and the current source, field gradients are large, hence microtraps can provide much stronger confinement than conventional electromagnet traps. Therefore the chip trap is ideally suited to study

atoms confined to one-dimension. The versatility of integrated atom traps can be extended using radio-frequency dressed potentials [50] a technique that we have recently explored in our setup [51]. Another promising recent development is the use of permanent magnetic material to trap atoms on a chip. Such traps do not suffer from ohmic heating and thus allow for the integration of large arrays of traps with a very high density [52].

1.3 This thesis

The outline of this thesis is as follows. Chapter 2 provides some theoretical background relevant to the experiments described in this thesis. The emphasis is on the description of a Bose gas confined to one dimension. In Ch. 3 the experimental setup is outlined. Details are given of the design and construction of the microtrap. Ch. 4 describes how we realize Bose-Einstein condensates in our microtrap. Subsequently, in Ch. 5, we treat a condensate as a macroscopic wave and use theory borrowed from optics to study atom coherence. In particular, we describe how we extract the temperature of an elongated quasi-condensate by measuring its width after focusing. Finally, in Ch. 6 experiments are compared to exact theory that goes beyond the macroscopic condensate description. The first observation of exact Yang-Yang thermodynamics on an atom chip is described.

2 Theoretical background

2.1 Introduction

This chapter provides some theoretical background to the subsequent experimental chapters. The experimentally important concepts of magnetic trapping and evaporative cooling are briefly described. The main part of this chapter provides a summary of theory for the one-dimensional (1D) Bose gas at low temperature (and the cross-over to it from a 3D trapped gas) that is relevant for our experiment.

The 1D Bose system has attracted much interest because it has properties significantly different from that in higher dimensions. Counterintuitively, repulsive bosons in 1D become more *strongly* interacting with *decreasing* density. The theoretical description of such a many-particle system with strong interactions is challenging: As interactions increase in importance theoretical approaches that treat the gas as non interacting (ideal Bose gas) or weakly interacting (mean-field) break down. Already in the 1960s theorists were able to do much better, however. Helped by the simple symmetry of the 1D geometry Girardeau, Lieb and Liniger, and Yang and Yang were able to construct exact solutions for the many-body quantum system. Solutions were found for impenetrable bosons, known as the Tonks-Girardeau (TG) gas, by Girardeau [53] and for bosons with finite delta-function interaction by Lieb and Liniger [35] [54], using a Bethe Ansatz [55]. The model of 1D delta interacting bosons is integrable and therefore exactly solvable. Yang and Yang found analytic integral equations for the thermodynamics of the Lieb-Liniger gas [36] at any finite temperature and interaction strength. Their method is also known as the thermodynamic Bethe Ansatz.

With the spectacular advances in experiments with ultracold atomic gases in the 1990s this theoretical work became of experimental relevance and the first 1D condensates were realized in 2001 [39–41]. The importance of exactly solvable models for experiments with quantum gases was first pointed out by Olshanii in 1998 [33]. Until recently, however, most experimental attention was to the zero-temperature case of the Lieb-Liniger gas. In particular, there was a run to reach the strongly interacting Tonks-Girardeau (TG) gas. The TG regime was reached experimentally in 2004 in two groups. The group of Immanuel Bloch used a 2D optical lattice and added a weak periodic potential along the third axis to increase the effective mass of the bosons [42]. David Weiss and coworkers used a different laser scheme that removed the need for the complicating third periodic potential [43, 56–58]. It

was the paper by Kheruntsyan and coworkers [59] of 2003 that elaborated on the connection between Yang-Yang thermodynamics and cold atom experiments, the authors could identify new physical regimes using their exact calculations of the local pair correlation function.

Besides the strictly one-dimensional case, in practice many experiments [39, 50, 60] are performed in the cross-over from a three-dimensional to a one-dimensional system. Moreover, one works in a trap as opposed to the homogeneous case. The dimensional cross-over is of crucial importance in the description of our experimental data and is therefore given special attention in this chapter. In experiments on our trapped cold atomic clouds we turn two knobs: atom number and temperature. By turning these knobs we probe a variety of different physical regimes that are mostly separated by smooth cross-overs rather than sharp phase transitions. Besides the only true phase transition that we encounter: Bose-Einstein condensation, three cross-overs are met:

- cross-over from a three-dimensional to a one-dimensional system,
- cross-over from a decoherent to a coherent atomic sample in 1D,
- cross-over from a weakly interacting to a strongly interacting gas in 1D.

The outline of this chapter is as follows. Section 2.2 introduces the basics of magnetic trapping. In Sec. 2.3 the commonly used approach to the ideal Bose gas and the phenomenon of Bose-Einstein condensation is summarized. We discuss the homogeneous and trapped cases in 3D and 1D as well as the dimensional cross-over. Section 2.4 deals with weakly interacting (quasi-)condensates in 3D, in 1D and in the dimensional cross-over. Phase-fluctuating condensates, and the relation between the phase coherence length and the temperature of a quasi-condensate are studied in Sec. 2.4.4. Section 2.5 is dedicated to the exact results for 1D repulsive bosons by Tonks-Girardeau, Lieb-Liniger and Yang-Yang. In section 2.5.3 we present a new finite-temperature model that explains our experimentally obtained data very well (see also Ch. 6). The weakly interacting 1D gas is treated using the exact Yang-Yang thermodynamic solutions thus incorporating both the cross-over from a decoherent to a coherent system and the cross-over from weak to strong interactions. In Sec. 2.6 we give an overview of the discussed regimes that can be characterized by the three parameters: interaction strength, radial confinement and temperature. These parameters span a three dimensional space. We specifically describe two subspaces: (a) interaction strength versus radial confinement at $T = 0$ (Sec. 2.6.1); (b) interaction strength versus temperature in the 1D limit (Sec. 2.6.2). Section 2.7 briefly touches on previous models for finite-temperature degenerate systems. Finally, in Sec. 2.8 we give some theoretical background for the experimentally important tool of evaporative cooling.

2.2 Magnetic trapping

Magnetic trapping is due to the Zeeman effect: The energy of the atomic state depends on the magnetic field due to the interaction of the magnetic moment of the

atom with the magnetic field, for a detailed description see e.g. [61–63]. A Zeeman sublevel of an atom with given total electronic angular momentum J and nuclear spin I can be labelled by the projection m_F of the total atomic spin $\mathbf{F} \equiv \mathbf{I} + \mathbf{J}$ on the axis of the field \mathbf{B} and by the total F ranging from $|I - J|$ to $I + J$. We are specifically dealing with the electronic ground state ($J = S = 1/2$) of ^{87}Rb ($I = 3/2$) so that $F = 1$ or $F = 2$. For these states the Zeeman energy shift can be calculated with the Breit-Rabi formula [63]. For the special case of atoms in the doubly polarized state ($F = 2, m_F = 2$) the Breit-Rabi formula yields a linear Zeeman shift

$$U(B) = U(0) + 2g_F\mu_B|\mathbf{B}|, \quad (2.1)$$

where $g_F \equiv (g_J + 3g_I)/4$, with $g_J = 2.00233113(20)$ [61] the fine structure Landé g-factor, $g_I = -0.0009951414(10)$ [61] the nuclear g-factor, $U(0)$ the energy in zero field and μ_B being the Bohr magneton. Because of the increasing energy in Eq. (2.1) with increasing magnetic field, atoms in the state ($F = 2, m_F = 2$) are “low-field seekers” that can be trapped in a local magnetic-field minimum. The other Zeeman states for ^{87}Rb that can be magnetically trapped for moderate field values are $F = 2, m_F = 1$ and $F = 1, m_F = -1$. In a region of small magnetic field the precession of the atomic magnetic moment is so slow that the changing field direction as a result of the atomic motion cannot be followed adiabatically. Atoms traversing such a region can undergo a so-called Majorana spin-flip to an untrapped state. To avoid this loss mechanism access of the atoms to low magnetic field regions should be prevented by arranging a non-zero magnetic field strength at the potential minimum.

To describe the thermodynamics of a trapped gas it is convenient for future reference to approximate the confining potential as a power-law trap of the general form [31]

$$U(x, y, z) = a_x|x|^{1/\delta_1} + a_y|y|^{1/\delta_2} + a_z|z|^{1/\delta_3}, \quad (2.2)$$

where

$$\delta = \sum_i \delta_i, \quad (2.3)$$

with $\delta = 0$ for 3D box-like, $\delta = 3/2$ for 3D harmonic and $\delta = 3$ for a spherical-quadrupole trap. The lowest order, and therefore tightest, magnetic trapping potential that has a non-zero minimum is 3D harmonic and can be written as

$$U(x, y, z) = U_0 + \frac{1}{2}m\omega_x^2x^2 + \frac{1}{2}m\omega_y^2y^2 + \frac{1}{2}m\omega_z^2z^2, \quad (2.4)$$

where ω_i is the single-particle oscillator frequency and m is the atomic mass.

A magnetic-field configuration that is 3D harmonic near the minimum was introduced by Ioffe [64] for plasma confinement. It was first proposed and used by Pritchard [65] to trap neutral atoms and is known as the Ioffe-Pritchard (IP) trap. Following Luiten [66] we define $\alpha = (\partial B_\perp/\partial\rho)_{x=x_0}$ and $\beta = (\partial^2 B_x(0, 0, x)/\partial x^2)_{x=x_0}$, and write the magnetic field for the IP configuration in polar coordinates

$$\begin{aligned} B_\perp(\rho, \phi, x) &= \alpha\rho \sin(2\phi) - \frac{1}{2}\beta\rho(x - x_0), \\ B_\phi(\rho, \phi, x) &= \alpha\rho \cos(2\phi), \\ B_\parallel(\rho, \phi, x) &= B_0 + \frac{1}{2}\beta(x - x_0)^2 - \frac{1}{4}\beta\rho^2. \end{aligned} \quad (2.5)$$

Indeed the magnetic field is approximately harmonic close to the center of the IP trap, for magnetic field values close to B_0 (the value of the magnetic field in the trap bottom). The harmonic approximation is valid for trapped atom clouds with a temperature much lower than $\mu_B B_0/k_B$. Using equations (2.1), (2.4) and (2.5) we find the trap frequencies in axial and radial direction

$$\omega_{\parallel} = \sqrt{\frac{\mu_B g_F m_F}{m}} \beta, \quad (2.6)$$

$$\omega_{\perp} = \sqrt{\frac{\mu_B g_F m_F}{m} \left(\frac{\alpha^2}{B_0} - \frac{\beta}{2} \right)} \quad (2.7)$$

In the high-temperature limit, if the thermal energy of atoms in a IP-trap is much larger than the energy corresponding to the trap bottom, $k_B T \gg \mu_B B_0$, we can approximate the IP potential, resulting from Eq. (2.1) and Eq. (2.5), in the two radial directions by a linear and in the axial direction by a harmonic shape. The factor δ , Eq. (2.3), equals 5/2 in this case.

Strong trapping forces are generated by high magnetic field gradients. Weinstein and Librecht [47] realized that when creating a trapping field at a distance r from a wire that carries a current I , the field gradient scales as I/r^2 . Microtraps thus provide an advantage over conventional electromagnets to tightly confine atoms.

The simplest wire-based trap is illustrated in Fig. 1.1. A current-carrying wire (along x) whose magnetic field is compensated by a homogeneous field B_{bias} (along y) forms a waveguide. Around the minimum (r_0), the field in the radial direction (yz -plane) is quadrupolar. This waveguide can be closed at the end points by adding two perpendicular current-carrying wires (along y) thus creating an **H**. End caps can also be made by bending the leads of the x -wire in the y -direction to create a **Z** shape. One can estimate the field gradient of such a trap using the field for an infinitely thin wire

$$r_0 = \frac{\mu_0 I}{2\pi B_{\text{bias}}}, \quad (2.8)$$

$$B'(r_0) = -\frac{\mu_0 I}{2\pi r_0^2}, \quad (2.9)$$

with $\mu_0 = 4\pi \cdot 10^{-7} \text{NA}^{-2}$. For example, with a current of 1 A and $B_{\text{bias}} = 100$ G we have $r_0 = 20 \mu\text{m}$ and a huge gradient $B'(r_0) = 5 \cdot 10^4$ G/cm.

2.3 Ideal Bose gas

In the ideal-gas description, atoms are considered as non-interacting quantum-mechanical particles. For homogenous ultracold dilute Bose gases in 3D this description can be found in textbooks such as [67]. This treatment has been extended for power-law potentials [31, 68], and for lower dimensional systems [32, 69].

In a 3D homogenous gas of bosons the average occupation number N_i of states with energy ε_i obeys Bose statistics

$$N_i = \frac{1}{e^{\beta(\varepsilon_i - \mu)} - 1} = \frac{ze^{-\beta\varepsilon_i}}{1 - ze^{-\beta\varepsilon_i}}, \quad (2.10)$$

where $\beta = (k_B T)^{-1}$. The fugacity z and the chemical potential μ are related by $z = e^{\beta\mu}$. The total atom number N is found by summing over all quantum states i

$$N = \sum_{i=0}^{\infty} N_i. \quad (2.11)$$

This sum diverges for $z \rightarrow 1$ because the term $N_0 = z/(1 - z)$ diverges in the thermodynamic limit (we take $\varepsilon_0 = 0$ from here on). Splitting off the diverging term N_0 , replacing the rest of the sum by an integral (one state per phase space element $\Delta\mathbf{r}\Delta\mathbf{p} = h^3$) the equation of state for N atoms occupying a volume V becomes

$$\frac{N}{V} = \frac{4\pi}{h^3} \int_0^{\infty} dp p^2 \frac{1}{z^{-1}e^{\beta p^2/2m} - 1} + \frac{1}{V} \frac{z}{1 - z}. \quad (2.12)$$

This can be written in the form [67]

$$n(z, T) = \frac{1}{\Lambda_T^3} g_{3/2}(z) + \frac{N_0}{V}, \quad (2.13)$$

where $n = N/V$ is the particle density,

$$\Lambda_T = \sqrt{2\pi\hbar^2/mk_B T}, \quad (2.14)$$

is the thermal de Broglie wavelength and $g_{3/2}$ is the Bose or Polylog function defined by

$$g_\alpha(z) = \sum_{j=1}^{\infty} z^j / j^\alpha. \quad (2.15)$$

For the ground-state particle density we have

$$\frac{N_0}{V} = n_0 = \frac{1}{V} \frac{z}{1 - z} \quad (2.16)$$

and for the density in the excited states

$$n_e = \frac{1}{\Lambda_T^3} g_{3/2}(z). \quad (2.17)$$

Note that $g_{3/2}(z)$ is finite for $z \rightarrow 1$ ($g_{3/2}(1) = 2.612\dots$), and thus n_e is limited, $n_e \leq g_{3/2}(1)/\Lambda_T^3$. At a given density, for low enough temperature, μ tends to zero from below and we have $z \rightarrow 1$; the Bose gas is saturated. All extra particles added at constant temperature will be accommodated in the ground state. The ground state becomes macroscopically occupied giving rise to the phenomenon of

Bose-Einstein condensation. At the transition, the critical density and temperature are

$$n_c = \frac{1}{\Lambda_T^3} g_{3/2}(1), \quad (2.18)$$

$$T_c = \frac{2\pi\hbar^2}{mk_B} \left(\frac{n}{g_{3/2}(1)} \right)^{2/3}. \quad (2.19)$$

A phase space density can be defined as the number of particles occupying a volume equal to the de Broglie wavelength cubed

$$\Phi = n\Lambda_T^3. \quad (2.20)$$

At the critical point the phase space density is $\Phi = g_{3/2}(1)$. We make use of Eq. (2.19) to write down the temperature dependence of the fraction of particles in the ground state

$$\frac{N_0}{N} = 1 - \left(\frac{T}{T_c} \right)^{3/2}. \quad (2.21)$$

Homogeneous 2D and 1D ideal gas

Unlike the 3D case, for a 2D system in the thermodynamic limit the population of the ground state remains microscopic for decreasing temperatures down to $T \rightarrow 0$. One can say that there is no BEC in a finite-temperature ideal homogeneous 2D Bose gas. Similarly in 1D, in the thermodynamic limit the population of the ground state remains microscopic for any T indicating the absence of BEC in this system.

One can define a degeneracy temperature T_d for lower-dimensional systems that indicates the transition from the classical regime to the regime where a quantum treatment is needed because the thermal de Broglie wavelength starts to exceed the average interparticle separation. For a homogeneous Bose gas in 1D the semiclassical approach yields

$$n(z, T) = \frac{1}{\Lambda_T} g_{1/2}(z), \quad (2.22)$$

the 1D equivalent of Eq. (2.13) for 3D. Note that $g_{1/2}(z)$ diverges as $z \rightarrow 1$, consistent with the absence of a macroscopically occupied ground state in 1D in the semiclassical approximation. Degeneracy for a one-dimensional homogeneous Bose gas is thus reached for

$$T_d = \frac{\hbar^2 n_1^2}{2mk_B}, \quad (2.23)$$

where n_1 is the 1D density.

2.3.1 Ideal Bose gas harmonically trapped in 3D and 1D

We now turn to the D-dimensional ideal Bose gas in the presence of external harmonic confinement $V_{\text{ext}}(\mathbf{r}) = \sum_{i=1}^D m\omega_i^2 r_i^2/2$. We assume $k_B T \gg \hbar\omega_i$, consequently

we can use the semiclassical approximation and replace the sum in Eq. (2.11) by an integral. The semiclassical energy of the atoms trapped in the external potential is

$$\varepsilon(\mathbf{r}, \mathbf{p}) = \frac{\mathbf{p}^2}{2m} + V_{\text{ext}}(\mathbf{r}). \quad (2.24)$$

The density distribution of the thermal atoms as a function of position and momentum respectively is then obtained by integration (over momentum and position respectively) yielding

$$n(\mathbf{r}) = \frac{1}{\Lambda_T^D} g_{D/2} [ze^{-\beta V_{\text{ext}}(\mathbf{r})}], \quad (2.25)$$

$$n(\mathbf{p}) = \frac{1}{(m\bar{\omega}\Lambda_T)^D} g_{D/2} [ze^{-\beta p^2/2m}], \quad (2.26)$$

where $\bar{\omega} = (\prod_{i=1}^D \omega_i)^{1/D}$.

It was shown in [32] that upon lowering the dimension the critical temperature becomes higher. The expression for the critical temperature in a 1D trapped gas obtained in [32] is

$$N = \frac{k_B T_c}{\hbar\omega} \ln \frac{2k_B T_c}{\hbar\omega}. \quad (2.27)$$

2.3.2 Ideal Bose gas in the 3D-1D cross-over

If the 3D harmonic trap is highly anisotropic and needle shaped with $\omega_{\perp} \gg \omega_{\parallel}$ and $k_B T \approx \hbar\omega_{\perp}$ we have a cross-over from 3D to 1D for the ideal Bose gas. Only a few radial quantum states are occupied, therefore radially we can no longer use the semiclassical approximation from Sec. 2.3.1. In this cross-over case we sum explicitly over the radially excited states j of the harmonic oscillator with degeneracy $(j+1)$. For the axial direction we use the local density approximation (LDA): We treat the gas as locally homogeneous with a spatially varying chemical potential $\mu(x) = \mu - m\omega^2 x^2/2$ [70]. The resulting axial atomic density n_l is

$$n_l(x) = \sum_{j=0}^{\infty} (j+1) \frac{1}{\Lambda_T} g_{1/2} [e^{\beta(\mu(x) - j\hbar\omega_{\perp})}]. \quad (2.28)$$

2.4 Weakly interacting (quasi-)condensate

Consider a harmonically trapped gas in the low temperature limit far below the condensation temperature: $T \ll T_c$ and $N_0/N \rightarrow 1$, i.e. we have an almost pure Bose-Einstein condensate. Nearly all particles occupy the ground state and the atomic density becomes high. When the interaction energy exceeds the harmonic oscillator level splitting we can no longer neglect the effect of interatomic interactions.

Bogoliubov [71] adopted a mean-field approach to approximate the many-body wavefunction for the weakly interacting Bose gas, in order to obtain the excitation

spectrum for the zero-temperature limit (see Sec. 2.4.4). For an inter-particle separation that is much larger than the range of the atomic interaction potential and for low collision energies atomic interactions can be described using only s-wave scattering. The mean-field interaction energy can then be written as $\mu = ng$, where n is the 3D atomic density and g the coupling constant

$$g = \frac{4\pi\hbar^2 a}{m}, \quad (2.29)$$

where a is the s-wave atomic scattering length ($a = 5.24$ nm for ^{87}Rb in the state $F = 2, m_F = 2$ [72]). The Gross-Pitaevski (GP) equation is a mean-field expression for the ground-state wavefunction ψ

$$\left[-\frac{\hbar^2}{2m}\nabla^2 + V_{\text{ext}}(\mathbf{r}) + g|\psi(\mathbf{r})|^2 \right] \psi(\mathbf{r}) = \mu\psi(\mathbf{r}), \quad (2.30)$$

where $V_{\text{ext}}(\mathbf{r})$ is an external confining potential. Equation (2.30) is a non-linear Schrödinger equation, normalized as

$$N = \int d\mathbf{r} |\psi(\mathbf{r})|^2. \quad (2.31)$$

A Bose-Einstein condensate in the 3D mean-field regime is characterized by long-range order of the phase. The correlation length $l_c = \hbar/\sqrt{mng}$, the typical length scale associated with the atomic interaction energy, should be much smaller than the decay length of the phase coherence for any mean-field theory to hold.

2.4.1 Mean-field in three dimensions

We take the external potential in Eq. (2.30) to be a 3D isotropic harmonic trap $V_{\text{ext}}(\mathbf{r}) = m\omega^2\mathbf{r}^2/2$. A trapped Bose-Einstein condensate in the mean-field regime can be treated in the local density approximation (LDA) provided $\mu \gg \hbar\omega$. In this limit, the atomic density changes on a length scale much larger than that of the correlations in the gas, consequently we can treat the gas as locally homogeneous with a spatially varying chemical potential [70]. This amounts to neglecting the first (kinetic energy) term in Eq. (2.30); the mean-field energy of the trapped condensate exactly compensates the external potential energy. We have, for the spatial region where $V_{\text{ext}} < \mu_{TF}$, a cloud with a parabolic Thomas-Fermi (TF) profile in all three directions

$$n_{TF}(\mathbf{r}) = \frac{\mu_{TF} - V_{\text{ext}}(\mathbf{r})}{g}, \quad (2.32)$$

and $n_{TF} = 0$ elsewhere. The peak chemical potential μ_{TF} is determined by the total particle number N_0 . For a harmonic potential, the result is

$$\mu_{TF} = \frac{\hbar\omega}{2} \left(\frac{15N_0 a}{l} \right)^{2/5}, \quad (2.33)$$

where $l = \sqrt{\hbar/m\omega}$ is the ground-state size.

2.4.2 Mean-field 1D

If in an ultracold gas under strong radial confinement the thermal energy drops below the radial level splitting ($k_B T \ll \hbar\omega_\perp$), the atomic motion in transverse directions is frozen and we speak of a one-dimensional system. For temperatures much lower than the degeneracy temperature ($T \ll T_d$) [Eq. (2.23)], and sufficiently high density we have a weakly interacting gas that can be treated similarly to the 3D case using a mean-field theory. The resulting 1D system exhibits quasi-long-range order of the phase at zero temperature (the phase coherence decays algebraically) [34]. Therefore we do not speak of a true condensate but rather of a quasi-condensate (under sufficient axial harmonic confinement full phase coherence can be regained, see Sec. 2.4.4). We can now write for the 1D mean-field interaction energy $\mu \approx g_1 n_1 \ll \hbar\omega_\perp$, where we use the effective 1D coupling found by Olshanii [33]

$$g_1 = \frac{2\hbar^2 a}{ml_\perp^2} \left(1 - \mathcal{C} \frac{a}{\sqrt{2}l_\perp} \right)^{-1}, \quad (2.34)$$

with the constant $\mathcal{C} = 1.4603\dots$ [33] and the transverse oscillator length $l_\perp = \sqrt{\hbar/m\omega_\perp}$. In our experimental situation $l_\perp \gg a$ and the second term on the right-hand-side of Eq. (2.34) is a small correction. This 1D mean-field gas has the shape of the harmonic-oscillator ground state in the transverse direction. Along the axis we can use the LDA and find the parabolic Thomas-Fermi shape for the harmonically trapped case.

2.4.3 Mean-field 3D-1D crossover

The dimensional cross-over at $T = 0$ for a quasi-condensate with $\mu \approx \hbar\omega_\perp$ was treated in the mean-field regime by Menotti and Stringari [73] and by Gerbier [74]. The cross-over is approached from the 3D side where the chemical potential is much higher than the axial level splitting ($\mu \gg \hbar\omega_\parallel$): The condensate is in the GP regime and the density profile is parabolic both in axial and radial directions. Upon reduction of the linear density and consequently of the chemical potential we pass the dimensional cross-over regime ($\mu \approx \hbar\omega_\perp$) and reach the regime $\mu \ll \hbar\omega_\perp$. This results in a shape change of the radial density profile from parabolic when $\mu \gg \hbar\omega_\perp$ to the gaussian shape of the harmonic oscillator ground state for $\mu \ll \hbar\omega_\perp$. As long as $\mu \gg \hbar\omega_\parallel$ the *axial* shape stays parabolic. The characteristics of the condensate change gradually when going from elongated 3D to 1D. There is no transition point but a transition region. Gerbier [74] found a simple interpolation for the calculation of the chemical potential across the transition

$$\mu = \hbar\omega_\perp \left(\sqrt{1 + 4an_l} - 1 \right), \quad (2.35)$$

where the local linear density n_l is used without information on the axial potential. This approximate function Eq. (2.35) yields values that were found to be very accurate in comparison with exact numerical results obtained by Menotti [75]. The linear density profile in the external axial potential $V_{\text{ext}} = m\omega_x^2 x^2/2$ can be found in

the local density approximation using¹

$$n(x) = \frac{1}{4a} \frac{V_{\text{ext}}(L) - V_{\text{ext}}(x)}{\hbar\omega_{\perp}} \left[\frac{V_{\text{ext}}(L) - V_{\text{ext}}(x)}{\hbar\omega_{\perp}} + 2 \right], \quad (2.36)$$

$$L = \frac{l_x^2}{l_{\perp}} \sqrt{\frac{2\mu}{\hbar\omega_{\perp}}}, \quad (2.37)$$

where $l_{x,\perp} = \sqrt{\hbar/m\omega_{x,\perp}}$. We can define a cross-over point by equating the chemical potential Eq. (2.35) to the transverse oscillator strength ($\mu_{\text{co}} = \hbar\omega_{\perp}$), yielding

$$n_{l,\text{co}} = \frac{3}{4a}. \quad (2.38)$$

For ^{87}Rb in the $F = 2, m_F = 2$ state ($a = 5.24$ nm) the cross-over to 1D is reached at a linear density $n_{l,\text{co}} \approx 150 \mu\text{m}^{-1}$.

2.4.4 Excitations in elongated quasi-condensates

This section follows the lines of the review article on low-dimensional trapped gases by Petrov and coworkers [76] and in particular their treatment of finite temperature excitations of condensates with fluctuating phase (quasi-condensates) in the 1D regime, that is relevant to the experiments described in this thesis. The treatment starts from the 1D case. Petrov *et al.* [77] showed that a similar treatment holds for elongated 3D condensates.

In the mean-field regime at $T = 0$ long range order decays algebraically [28, 29]. At finite T , the phase coherence decays exponentially with a characteristic phase coherence length l_{ϕ} . In a trap, if l_{ϕ} exceeds the condensate halflength L , we have a true condensate. While for $l_{\phi} < L$ we have a quasi-condensate with fluctuating phase. In a quasi-condensate at sufficiently low temperatures so that $l_{\phi} \gg l_c$ density fluctuations are suppressed by the atomic interactions. The appearing phase fluctuations at finite temperature stem from thermal excitations of elementary modes of oscillation along the axis of the cloud. Bogoliubov [71] derived the excitation spectrum of a homogeneous weakly interacting Bose gas at zero temperature. His treatment was generalized for the spatially non-uniform case by de Gennes [78]. The Bogoliubov-de Gennes equations yield the energies of the elementary excitations of phase and density of the condensate

$$\varepsilon(k) = \sqrt{E(k)[E(k) + 2\mu]}, \quad (2.39)$$

where $E(k) = \hbar^2 k^2 / 2m$ is the free-particle spectrum. The spectrum Eq. (2.39) is phonon-like for energies in the order of or smaller than μ . The energies are $\varepsilon(k) \approx c_s \hbar k$, with the speed of sound $c_s = \sqrt{\mu/m}$. For larger momenta the spectrum is particle like with $\varepsilon(k) \approx E(k) + \mu$. At low enough temperature, $T \ll T_d, \mu$, the assumption that density fluctuations are small is justified. Then the fluctuations of

¹In the 2004 article by Gerbier [74] there are a few typographical errors in the corresponding equations.

the phase alone follow the same phonon-like Bogoliubov-de Gennes equations [76]. The gas can be viewed as consisting of the sum of a macroscopic wave-function containing contributions with wave-vectors $k \ll 1/l_c$, with $l_c = \hbar/\sqrt{m\mu}$, and a small component including the contributions with $k \sim 1/l_c$.

Theory for excitations of quasi-condensates can be extended to include non-zero temperature in the Bogoliubov-Popov approach [79, 80]. Petrov *et al.* worked out the case of a harmonically trapped, phase-fluctuating condensate for 1D [34] and elongated 3D [77] systems. We repeat some of their results below.

Phase fluctuations originate from thermal excitations of Bogoliubov modes of oscillation along the condensate axis. The phase coherence length is inversely proportional to the quasi-condensate temperature, therefore l_ϕ can be used as a thermometer for phase fluctuating condensates

$$l_\phi = \frac{\hbar^2 n_1}{mk_B T}. \quad (2.40)$$

Below a temperature T_ϕ the phase coherence extends over the whole harmonically trapped cloud ($l_\phi = L$) and a true condensate is regained

$$T_\phi = \frac{\hbar^2 n_1}{mk_B L}. \quad (2.41)$$

The mean-field approach is not valid anymore at high temperatures or low densities such that $l_c \gtrsim l_\phi$. In that case the density fluctuates strongly like in a non-degenerate gas. It is important to point out here that these strong density fluctuations imply that the usual (perturbative) Bogoliubov approach to the degenerate gas must break down, since the Popov approximation (expanding the fluctuations around the average density) can no longer be relied upon. In the next section we will show that, luckily, for this regime exact solutions for the many-body wavefunction are known.

2.5 Exact solutions in 1D

This section discusses exactly solvable models for interacting bosons in 1D. Solutions were found for impenetrable bosons by Girardeau [53] and for bosons with finite delta-function interaction by Lieb and Liniger [35]. Remarkably, Yang and Yang found integral equations describing the thermodynamics of the Lieb-Liniger gas [36] at any finite temperature. Figure 2.1 shows a cartoon of atomic density distributions in 1D for $T = 0$ (adapted from Ref. [43]). For increasing values of the interaction parameter γ , the interatomic separation increases, and the size of the wave-functions decreases.

2.5.1 Tonks-Girardeau

For a system of impenetrable point-like bosons in 1D the wave-function and ground state energy were derived by Girardeau [53]. By definition impenetrability means

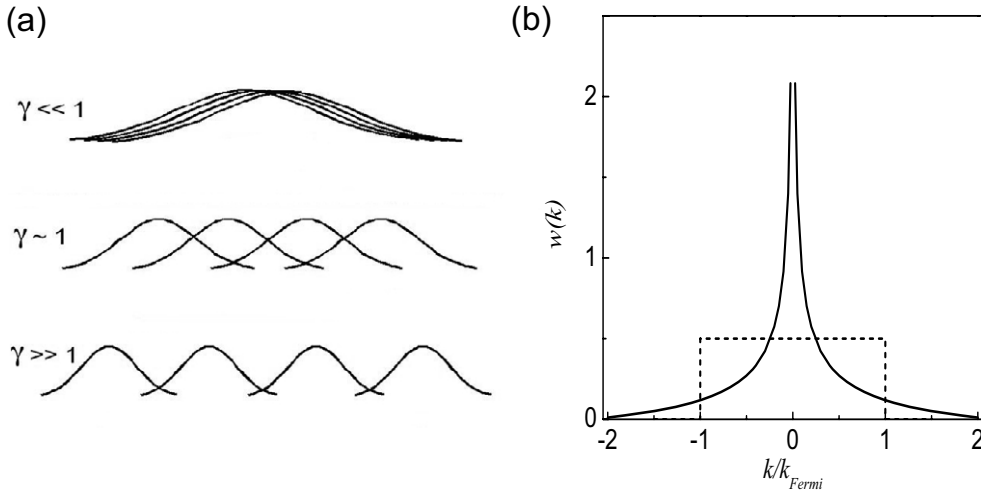


Figure 2.1: (a) Cartoon of atomic density distributions for the Lieb-Liniger gas at $T = 0$ [43]. For increasing values of the interaction parameter γ the interatomic separation increases and the size of the wave-functions decreases. Top: 1D quasi-condensate where atomic waves overlap. Middle: for decreasing density the atomic waves become more localized. Bottom: at very low density the atomic wave-functions exclude each other similar to ideal fermions, for $T = 0$ we have a Tonks-Girardeau gas. (b) Momentum distribution for a Tonks-Girardeau gas of impenetrable bosons at zero temperature (straight line). The corresponding distribution for an ideal Fermi gas is shown for comparison (dashed line). Adapted from Ref. [33].

that the wave-functions of two bosons vanishes when the two atoms are at the same position. Girardeau realized that this is just like the case of ideal fermions, in that case as a result of the exclusion principle. Consequently the ground-state wave-function for interacting bosons ψ^B can be mapped to a system of ideal free spinless fermions ψ^F by multiplying the Fermi wave-function by -1 upon particle exchange. For a ring of length L :

$$\psi^B = |\psi^F| \propto \prod_{j>l} |\sin[\pi L^{-1}(x_j - x_l)]|. \quad (2.42)$$

This wave-function varies smoothly everywhere except for the position where two particles meet, where it vanishes and has a cusp. While the density distribution of these “fermionized” bosons is identical to that of ideal fermions, their momentum distributions $w(k)$ are distinctly different. An analytic rigorous upper bound for $w(k)$ was first given by Lenard [81]. Later the long-range and short-range expansions for $w(k)$ were derived [82, 83]. Following Olshanii [33], we plot $w(k)$ in Fig. 2.1(b). For comparison the momentum distribution for the ideal Fermi case, with $k_F = \pi(N - 1)/L$, is also plotted.

2.5.2 Lieb-Liniger

Lieb and Liniger [35] found the ground-state wave-function for bosons with repulsive delta-function interaction of any strength on a one-dimensional ring (a box of length L with periodic boundary conditions). The Hamiltonian for the Lieb and Liniger system is

$$H = -\frac{\hbar^2}{2m} \sum_{j=1}^N \frac{\partial^2}{\partial x_j^2} + g_1 \sum_{i>j} \delta(x_i - x_j), \quad g_1 > 0. \quad (2.43)$$

The dimensionless ‘Lieb and Liniger’ parameter γ is then introduced

$$\gamma = \frac{mg_1}{\hbar^2 n_1}, \quad (2.44)$$

where $n_1 = N/L$. Using the Bethe Ansatz [55] Lieb and Liniger showed that the k ’s in the Ansatz satisfy

$$(-1)^{N-1} \exp(-ikL) = \exp \left[i \sum_{k'} \theta(k' - k) \right], \quad (2.45)$$

where θ is a phase shift obeying

$$\theta(k) = -2 \tan^{-1}(k/\gamma n_1), \quad -\pi < \theta < \pi. \quad (2.46)$$

Lieb [54] also analyzed the excitation spectrum of the Lieb-Liniger gas and found that besides a phonon-like ‘‘type I’’ excitation spectrum, a ‘‘type II’’ branch exist. While the type I excitations match the Bogoliubov phonon spectrum (Sec. 2.4.4) that is valid in the weak coupling limit, the type II excitations do not exist in the Bogoliubov approach. The new branch in the spectrum is associated with ‘‘hole-like’’ excitations: A hole is an omitted k value and is created when a particle with k_i is taken to k_N .

The 1D system shows a peculiar behavior: the system becomes more *strongly* interacting as the density *decreases*. This counter-intuitive effect can be qualitatively understood through the γ parameter. It can be interpreted as the ratio of the interaction energy $\epsilon_{\text{int}} = n_1 g_1$ to the characteristic kinetic energy of the atoms $\epsilon_{\text{kin}} \approx \hbar^2 n_1^2 / 2m$. Lowering the density, reduces the kinetic energy faster than the interaction energy, thus for low density ($\gamma \gg 1$) we have a strongly interacting gas (Tonks-Girardeau), while in the opposite limit for ($\gamma \ll 1$) we have a weakly interacting gas (1D mean-field).

A nice hybrid theoretical and numerical approach to calculate the excitation spectrum of the Lieb-Liniger gas was taken by Caux and Calabrese [84]. From their results for $0.25 < \gamma < 100$ it becomes clear that for *zero temperature* hole-like excitations are important only for $\gamma \gtrsim 1$. We shall see in the following that already at weak coupling ($\gamma \ll 1$) but for *finite temperature* deviations from the Bogoliubov treatment become important.

2.5.3 Yang-Yang

Yang and Yang [36] extended the Lieb-Liniger treatment to non-zero temperatures. Their method is also known as thermodynamic Bethe Ansatz [37, 38]. Yang and Yang included the effect of thermal excitations by allowing the existence of a whole collection of omitted momentum states (holes), with density $\rho_h(k)$ besides the density of occupied momentum states $\rho(k)$. Yang and Yang were then able to derive analytic expressions for the thermodynamics of this gas. Their main result is formed by the two integral equations

$$\epsilon(k) = -\mu + \frac{\hbar^2 k^2}{2m} - \frac{k_B T g_1}{2\pi} \int_{-\infty}^{\infty} \frac{dq}{(g_1 m / \hbar^2)^2 + (k - q)^2} \ln \{1 + \exp[-\epsilon(q)/k_B T]\}, \quad (2.47)$$

where ϵ is defined by

$$\rho_h / \rho = \exp[\epsilon(k)/k_B T], \quad (2.48)$$

and

$$2\pi f(k) = 1 + \frac{2g_1 m}{\hbar^2} \int_{-\infty}^{\infty} \frac{\rho(q) dq}{(g_1 m / \hbar^2)^2 + (k - q)^2}, \quad (2.49)$$

for

$$f(k) = \rho + \rho_h. \quad (2.50)$$

Equation (2.47), where μ is the chemical potential, can be solved for ϵ by iteration. Subsequently ρ can be obtained by iterating Eq. (2.49).

Extra information is obtained [59] by differentiating the free energy per particle FN^{-1} with respect to γ at constant density and temperature

$$g^{(2)} = \frac{2m}{\hbar^2 n_1^2} \left[\frac{\partial(FN^{-1}(\gamma, \tau))}{\partial\gamma} \right]_{n, \tau}, \quad (2.51)$$

where $g^{(2)}$ is the local pair correlation function that expresses the (normalized) probability to find two particles at the same position. In a mean-field condensate, interactions stabilize the density and $g^{(2)} \approx 1$. While ideal bosons experience “bunching” and have $g^{(2)} = 2$, the opposite holds for ideal fermions with $g^{(2)} = 0$ (“anti-bunching”). Fermionized bosons in the TG limit also have $g^{(2)} = 0$.

Figure 2.2(a) shows the numerical solution of the Yang-Yang equations for $1/\gamma \propto n_{YY}$ for different values of the dimensionless temperature parameter

$$t = \frac{2k_B T \hbar^2}{m g_1^2}. \quad (2.52)$$

We plot the values: $t=2000$ (red), $t=1000$ (black), $t=500$ (blue), (numerical data obtained by Kheruntsyan [59, 85]). The exact numerical result (solid lines) is compared with the behavior in the mean-field regime (dashed lines) and with the ideal Bose gas result (dotted lines). The Yang-Yang thermodynamic equations yield a smooth equation of state $n_{YY}(\mu, T)$, including the region around $\mu(x) = 0$. This deviates dramatically from both the ideal-gas description (diverging density as μ approaches zero from below, cf. Eq. (2.22)) and the quasi-condensate description

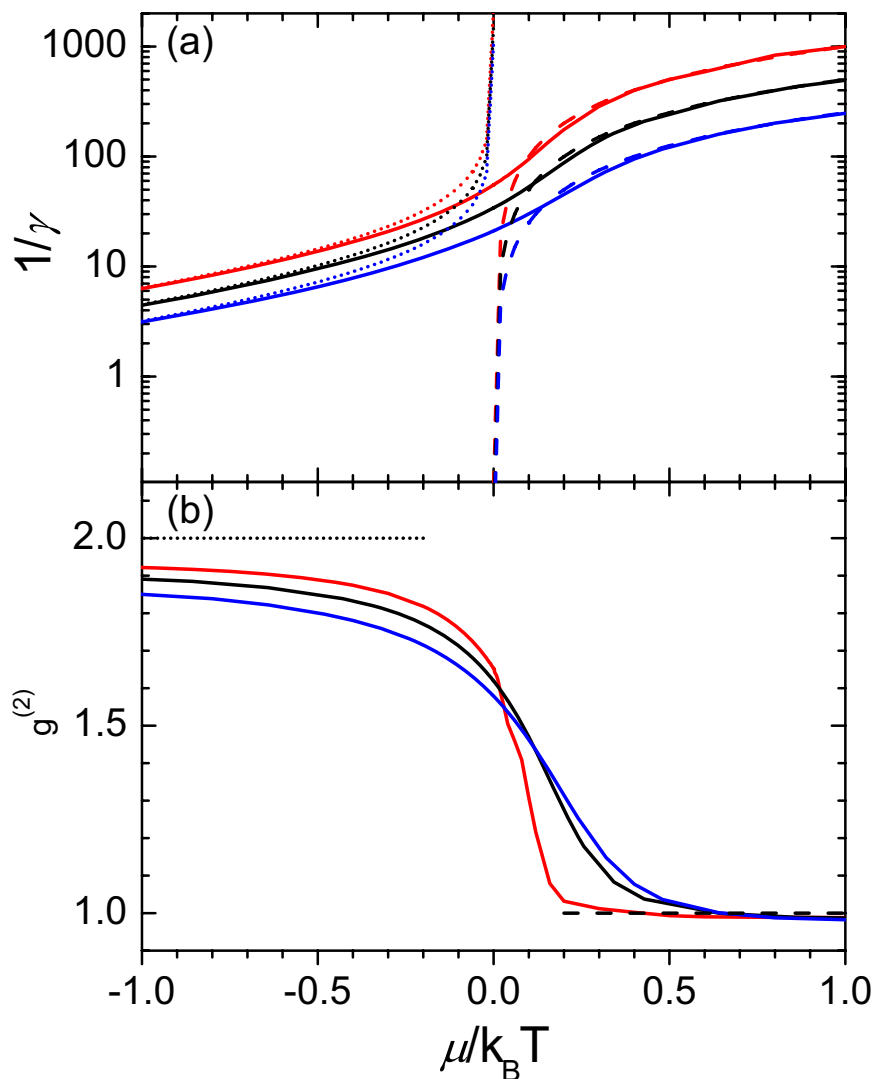


Figure 2.2: (a) Equation of state of the uniform weakly interacting 1D Bose gas for three different values of the temperature parameter $t = 2k_B T \hbar^2 / m g_1^2$: $t=2000$ (red); $t=1000$ (black); $t=500$ (blue). The exact numerical result (solid lines) is compared with the behavior in the mean-field regime (dashed lines) and with the ideal Bose gas result (dotted lines). (b) The local correlation $g^{(2)}$ versus $\mu/k_B T$ for the same values of t as above. The solid curves are exact numerical results, while the dashed line indicates the mean-field value and the dotted line the behavior of the ideal Bose gas.

($\mu = n_1 g_1$; vanishing density as μ approaches zero from above). Hence the exact solutions are crucial for a correct description of the Bose gas in the region around $\mu = 0$ as is described in more detail in Ch. 6.

Fig. 2.2(b) shows the local correlation $g^{(2)}$ versus $\mu/k_B T$ for the same values of t as above. The solid curves are exact numerical results, while the dashed line indicates the mean-field value and the dotted line the behavior of the ideal Bose

gas. The calculated value of the local pair correlation function $g^{(2)}$ varies smoothly between ≈ 1 and $\lesssim 2$ in the plotted range of μ . This differs from the ideal-gas value of 2 and the quasi-condensate value of ≈ 1 .

2.6 Overview of ultracold Bose gas regimes

2.6.1 Regimes for $T = 0$

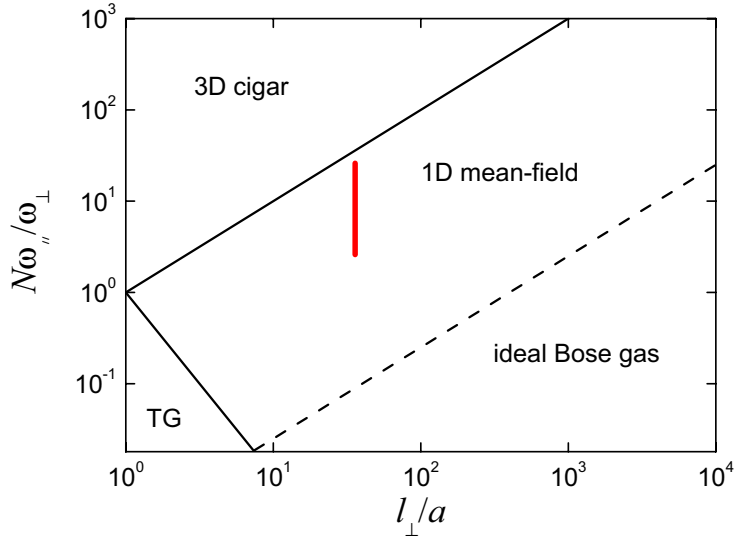


Figure 2.3: Phase diagram for $T = 0$, in the plane $N\omega_{\parallel}/\omega_{\perp}$ versus l_{\perp}/a , based on Fig. 1 of Ref. [73]. The dashed line indicates $N\omega_{\parallel}/\omega_{\perp} = (\omega_{\parallel}/\omega_{\perp})^{3/2}l_{\perp}/a$ for $\omega_{\parallel}/\omega_{\perp} = 1/400$. The red line indicates the parameter range covered in our experiment.

The transitions between the various regimes for the $T = 0$ case, that were summarized above, have been studied for a trapped gas by several authors [34, 73]. We follow here the approach by Menotti and Stringari [73]. These authors describe atoms trapped in an elongated harmonic trap with $\omega_{\perp} \gg \omega_{\parallel}$. The longitudinal confinement is weak and for high enough atom number N the atomic interaction energy largely exceeds the axial level splitting ($\mu \gg \hbar\omega_{\parallel}$) and the local density approximation can be used.

A schematic phase diagram is plotted in Fig. 2.3. The line $N\omega_{\parallel}/\omega_{\perp} = l_{\perp}/a$ indicates the cross-over from the 3D cigar from the 1D mean-field regime. Using $\mu = \hbar\omega_{\perp}$ in Eq. (2.36) it follows that this is equivalent to the criterium $n_l = 3/4a$ [74]. The line $N\omega_{\parallel}/\omega_{\perp} = (l_{\perp}/a)^{-2}$ indicates the cross-over from 1D mean-field to the Tonks-Girardeau gas. This demarkation, marked by $\gamma = 1$ in the homogeneous case, is found when the interaction energy equals the kinetic energy: $\pi^2\hbar^2n_1^2/2m = g_1n_1$ for the harmonically trapped case, solved in Ref. [73]. The dashed line indicates the cross-over from the parabolic 1D mean-field regime to the ideal gas or gaussian condensate regime where the axial level splitting is large compared to the

atomic interaction energy and the LDA can not be used. We draw the dashed line $N\omega_{\parallel}/\omega_{\perp} = (\omega_{\parallel}/\omega_{\perp})^{3/2}l_{\perp}/a$ for $\omega_{\parallel}/\omega_{\perp} = 1/400$, the aspect ratio of the trap used in Chapters 5 and 6. In our experiment we vary the number of atoms in the quasi-condensate between 10^3 and 10^4 , while $l_{\perp}/a = 36$. The covered range is indicated in red in Fig. 2.3. It is clear that the physics of one-dimensional atomic gases plays an important role in our experiments. Secondly, for our aspect ratio we do not reach the TG regime when the atom number is lowered.

2.6.2 Regimes in 1D

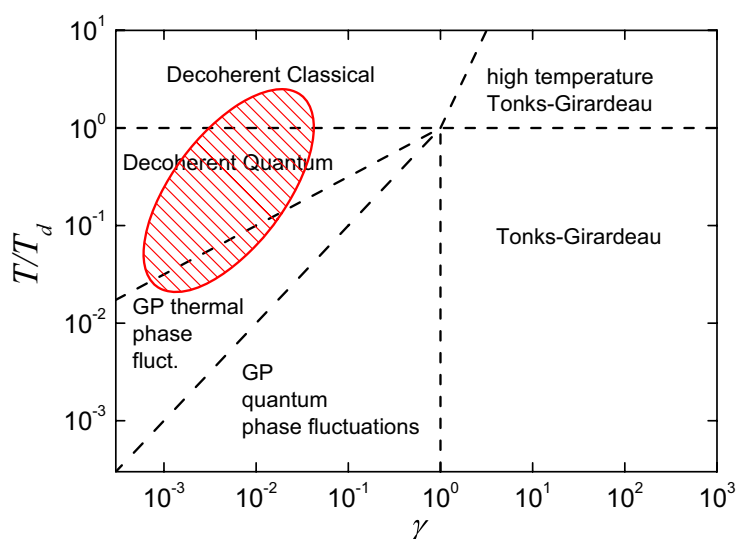


Figure 2.4: Diagram of states for the homogeneous 1D Bose gas in the plane T/T_d versus $\gamma = mg_1/\hbar^2 n_1$. The degeneracy temperature in 1D is given by $T_d = \hbar^2 n_1^2 / 2mk_B$. The area shaded in red indicates the parameter range covered in our experiment.

The system of delta-function interacting bosons in 1D can be effectively characterized by the combination of the dimensionless coupling parameter γ [Eq. (2.44)] and the reduced temperature $\tau = T/T_d$, with T_d the 1D degeneracy temperature [Eq. (2.23)]. Using the exact values of $g^{(2)}$ [Eq. (2.51)] Kheruntsyan and coworkers [70] have classified various physical regimes for the interacting Bose gas in 1D at finite temperature. The diagram of states is shown in Fig. 2.4. Above the degeneracy temperature two regimes are indicated. For small γ we are in the ‘decoherent classical’ or non-degenerate ideal Bose gas regime where $g^{(2)} \approx 2$. For large γ , strong interactions result in high temperature fermionization, characterized by $g^{(2)} \rightarrow 0$. Below the degeneracy temperature four regimes are distinguished. For $\gamma \gg 1$ we have a degenerate Tonks-Girardeau gas with $g^{(2)} \rightarrow 0$. For $\tau \ll \gamma \ll 1$ we have the mean-field regime and the finite temperature correction to the zero-temperature result for the local correlations is small: $g^{(2)} \approx 1$. In this regime quantum fluctuations of the phase dominate over thermal fluctuations. For higher temperatures

$\gamma \ll \tau \ll \sqrt{\gamma}$ we have a mean-field quasi-condensate characterized by thermal fluctuations of the phase, interactions stabilize the density so that $g^{(2)} \gtrsim 1$. If we increase the temperature further $\sqrt{\gamma} \ll \tau \ll 1$ phase coherence is destroyed and we enter the decoherent quantum regime with $g^{(2)} \lesssim 2$. The parameter range covered in the experiments described in this thesis, indicated in red, ranges from the classical regime via the decoherent quantum regime into the mean-field regime.

2.7 Previous models for $T > 0$

2.7.1 Semi-ideal Bose gas

In the situation of a three-dimensional harmonically trapped cloud ($k_B T, \mu \gg \hbar\omega$) just below the condensation temperature $T/T_c \lesssim 1$, the number of non-condensed atoms is large and can not be neglected. In a first approximation [86] we suppose that condensed and non-condensed fractions can be separated spatially because the spatial extent of the BEC is much smaller than that of the thermal cloud so the two parts do not have much spatial overlap. It is further assumed that the BEC is not influenced by the presence of the thermal atoms and maintains its TF profile [Eq. (2.32) and Eq. (2.33)]. The quantum saturated thermal cloud however is repelled by the mean-field interaction energy $2gn_{TF}(\mathbf{r})$ with the much denser condensate in the trap center. The factor 2 accounts for collisions between atoms in *different* quantum states. To find the density distribution of the thermal atoms for this case we use Eq. (2.25) with $D = 3$ that can be written as

$$n_T(\mathbf{r}) = \frac{1}{\Lambda_T^3} g_{3/2} \left[e^{\beta[\mu - V_{\text{eff}}(\mathbf{r})]} \right], \quad (2.53)$$

where we use the effective potential $V_{\text{eff}}(\mathbf{r}) - \mu = V_{\text{ext}}(\mathbf{r}) - \mu_{TF} + 2gn_{TF}(\mathbf{r})$.

2.7.2 Self-consistent Hartree-Fock

When dealing with the system as described in the previous section a more refined approximation can be made by taking into account not only the influence of the condensate on the thermal atoms but also vice versa. This problem can be solved numerically in an iterative process and is referred to as a self-consistent Hartree-Fock (HF) approach [87, 88]. The self-consistent potential for the thermal atoms is

$$V_{\text{eff}}(\mathbf{r}) - \mu = V_{\text{ext}}(\mathbf{r}) + 2gn_0(\mathbf{r}) + 2gn_T(\mathbf{r}) - \mu. \quad (2.54)$$

The condensate profile is affected by the density of the thermal atoms:

$$n_0(\mathbf{r}) = \max \left\{ 0, \frac{\mu - V_{\text{ext}}(\mathbf{r}) - 2gn_T(\mathbf{r})}{g} \right\}. \quad (2.55)$$

Fixing the total atom number fixes the chemical potential of the thermal fraction $\mu = gn_0(0) + 2gn_T(0)$. This self-consistent HF approach gives accurate results in

the 3D case [89] but has been shown to fail in the description of experimentally obtained profiles when the gas approaches the one-dimensional regime: $k_B T, \mu \simeq 2\hbar\omega_\perp$ [60]. The breakdown of this HF method when approaching the 1D regime and $\mu \approx 0$, can be seen as follows: In 1D, since $g_{1/2}(z) \rightarrow \infty$ as $\mu \uparrow 0$ (Sec. 2.3) for any peak density $n(0)$, one can always find a self-consistent HF solution, in the semiclassical approximation for the axial distribution, which has $n_0 = 0$, and $\mu < V_{\text{ext}}(0)$. Note also that the local value of the two particle correlation function $g^{(2)}$ differs significantly from both the values 2 and 1 assumed in this approach for the thermal atoms and the condensate atoms respectively (Fig. 2.2).

Luttinger liquid

Another mean-field approach, that will not be discussed further here, is employing the Luttinger liquid (see Haldane [90–93]). It is used mainly for strongly interacting systems and has the same region of validity as Bogoliubov-Popov: $l_\phi \gg l_c$. The Luttinger-liquid approach to one-dimensional Bose gases with delta-function interaction was discussed in detail by Cazalilla [94]. The method has been used successfully to describe the dynamics of phase fluctuations in mean-field condensates [95, 96].

2.8 Evaporative cooling

An important tool in atom cooling that provides the final increase in phase-space density that ultimately leads to Bose-Einstein condensation is evaporative cooling. In this process the high-energy tail of the Maxwell-Boltzmann velocity distribution of the trapped atoms is selectively removed, for example using radio-frequency (RF) induced spin flips. The remaining atoms collide elastically and re-thermalize. The energy per particle decreases and the sample is cooled. Theory describing the evaporative cooling process can be found in [97–100]. We repeat here only the key equations that can be used to calculate the efficiency of the evaporative cooling process. We add specific calculations for the case of the Ioffe-Pritchard trap in the high temperature limit with $\delta = 5/2$ that do not appear in the cited references. A treatment of the IP trap that is valid in the complete range from the high to the low temperature limit can be found in Ref. [100].

If the atomic density of trapped alkali atoms is not too high ($n < 10^{20} \text{ m}^{-3}$) three body collisions (that lead to losses via spin exchange) are rare and for typical experiments on alkali atoms the trap lifetime is limited by collisions with background gas. For a trap depth ϵ the truncation parameter is $\eta = \epsilon/k_B T$. Evaporative cooling works most effectively if the truncation parameter η is kept constant. This can be achieved by ramping down the trap barrier during the cooling process, so called forced evaporation. The timescale for evaporative cooling is set by the elastic collision time

$$\frac{1}{\tau_{\text{el}}} = \sqrt{2}n_0 v_{\text{th}} \sigma, \quad (2.56)$$

where $\sigma = 8\pi a^2$ is the s-wave collisional cross-section and $v_{\text{th}} = \sqrt{8k_B T/\pi m}$ the

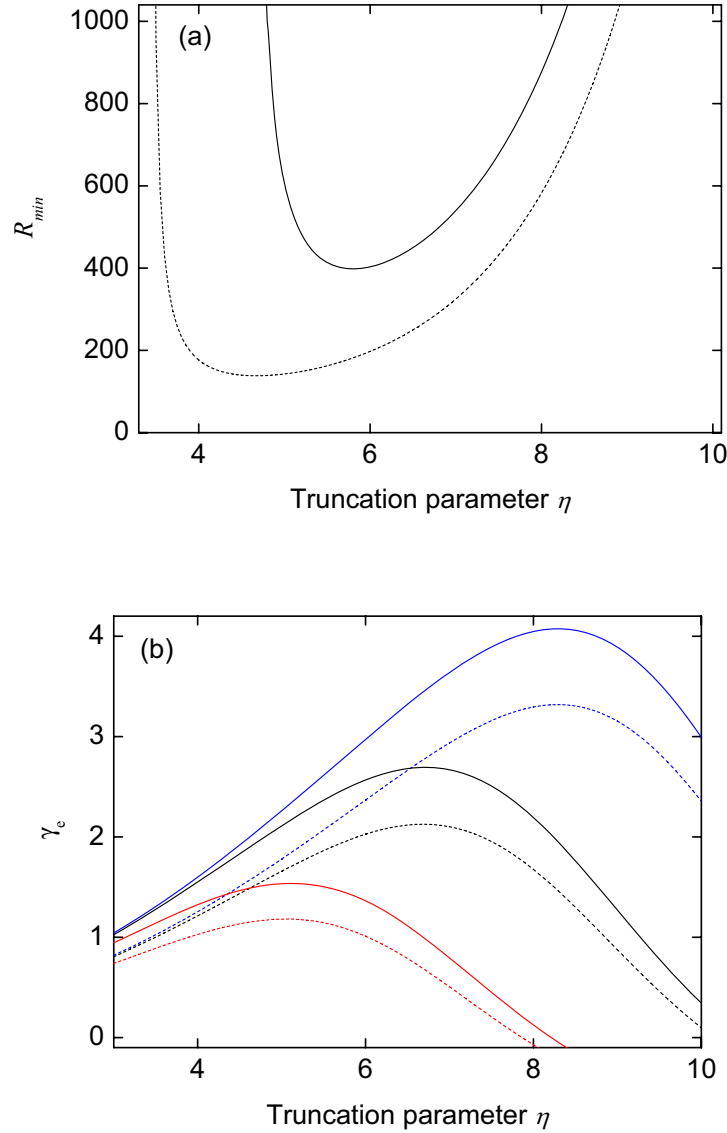


Figure 2.5: (a) Minimum value for the ratio of good to bad collisions plotted as a function of the truncation parameter. Comparison between the 3D parabolic potential ($\delta = 3/2$, solid line) and the 2D linear 1D harmonic potential ($\delta = 5/2$, dashed line). (b) The efficiency parameter of evaporative cooling γ versus the truncation parameter η for $\delta = 3/2$ (solid lines) and $\delta = 5/2$ (dashed lines). In each case, three different lines are given for ratio of good to bad collisions R of 5000 (blue), 1000 (black) and 200 (red).

thermal velocity. For efficient evaporative cooling the ratio R of “good” elastic collisions to “bad” collisions with background gas should exceed a minimal value $R = \tau_{\text{loss}}/\tau_{\text{el}} > R_{\text{min}}$, where τ_{loss} is the trap lifetime. If $R > R_{\text{min}}$ the collision rate increases with decreasing temperature and the regime of run-away evaporation is

entered. Run-away evaporation is most easily reached for steep traps where the density of states decreases rapidly with decreasing temperature as can be seen in the comparison between the 3D harmonic trap [$\delta = 3/2$, Eq. 2.2] and the steeper 1D harmonic 2D linear trap ($\delta = 5/2$) in Fig. 2.5(a). The minimal value for the ratio of good to bad collisions is given by

$$R_{\min}(\delta, \eta) = \frac{\lambda(\delta, \eta)}{\alpha(\delta, \eta)[\delta - 1/2] - 1}, \quad (2.57)$$

where α is the key parameter of the evaporative cooling process, which expresses the temperature decrease per particle lost, and λ is the ratio of the evaporation time to the elastic collision rate. The parameters α and λ can be calculated using the following expressions.

Used below are the incomplete gamma functions P and R , defined as (see appendix in Ref. [98])

$$P(a, \eta) = \frac{1}{\Gamma(a)} \int_0^\eta t^{a-1} e^{-t} dt, \quad (2.58)$$

$$R(a, \eta) = \frac{P(a+1, \eta)}{P(a, \eta)}, \quad (2.59)$$

where $\Gamma(a)$ is the Euler gamma function. The average energy of the escaping atoms is $(\eta + \kappa)k_B T$, where the parameter κ for the case of a power-law trap is

$$\kappa = 1 - \frac{P(7/2 + \delta, \eta)}{\eta P(3/2 + \delta, \eta) - (5/2 + \delta)P(5/2 + \delta, \eta)}. \quad (2.60)$$

This leads to an expression for α for forced evaporative cooling at constant η (see p. 194 of Ref. [99])

$$\alpha(\delta, \eta) = \frac{\eta + \kappa(\delta, \eta) - [3/2 + \tilde{\gamma}(\delta, \eta)]}{3/2 + \tilde{\gamma}(\delta, \eta) + \kappa(\delta, \eta)[\delta - \tilde{\gamma}(\delta, \eta)]}, \quad (2.61)$$

where the scaling parameter $\tilde{\gamma}$ [see Ref. [98], Eq. (99)] for a power-law trap is

$$\tilde{\gamma} = -\frac{3}{2} + \left(\frac{3}{2} + \delta\right) R(3/2 + \delta, \eta). \quad (2.62)$$

Finally, the parameter λ , expressing the ratio of the evaporation time to the elastic collision rate is given by

$$\lambda(\delta, \eta) = \left(1 - \left[\frac{3}{2} + \delta\right] [1 - R(3/2 + \delta, \eta)] \alpha(\delta, \eta)\right) \frac{\sqrt{2} \exp(\eta)}{\eta - (5/2 + \delta)R(3/2 + \delta, \eta)}. \quad (2.63)$$

Once the condition $R > R_{\min}$ is fulfilled it is useful to calculate the overall figure of merit for the effectiveness of the evaporation process given by the parameter $\gamma_{e,\text{tot}}$, that expresses the relative increase in phase space density with decreasing atom number

$$\gamma_{e,\text{tot}} = \frac{\ln(\Phi_{\text{final}}/\Phi_{\text{initial}})}{\ln(N_{\text{final}}/N_{\text{initial}})}. \quad (2.64)$$

This global parameter is maximal when $\gamma_e = -d(\ln \Phi)/d(\ln N)$ is optimized at all times. From Eq. (10) of Ref. [99] we find

$$\gamma_e(\delta, \eta, R) = \frac{\alpha(\delta, \eta)[\delta + 3/2]}{1 + \lambda(\delta, \eta)/R} - 1. \quad (2.65)$$

The calculated values of γ_e for the cases $\delta = 3/2$ and $\delta = 5/2$ are plotted in Fig. 2.5(b). In the case $\delta = 5/2$ for $R = 1000$ the overall maximal efficiency $\gamma_e = 2$, provided $\eta \approx 7$. This means that a typical gain of 6 orders of magnitude in phase space density costs 3 orders of magnitude in atom number.

3 Experimental Setup

3.1 Introduction

In this chapter the experimental setup is described. It begins with a general discussion of our design considerations followed by a description of the five main parts of the setup. The central and most innovative part of the experimental setup is formed by the microtrap that is treated with some detail.

The concept of the “atom chip” combines the advantages of scale reduction and reproducibility with the possibility to trap atoms under very strong confinement. The confining force for atoms is proportional to the gradient of the magnetic field strength. Figure 3.1 illustrates that chip traps can have very high gradients with a simple example: the side guide. This tube-like atom trap is created with a chip in the xy -plane at $z = 0$, when the field from a current I through a wire along x is compensated by a homogeneous bias field B_{bias} along y . A trap occurs at a distance z_0 from the chip surface. The trap position and the gradient of the magnetic field at that point are given by the Biot-Savart law, and can be written as

$$z_0 = \frac{\mu_0 I}{2\pi B_{\text{bias}}}, \quad (3.1)$$

$$\frac{\partial B}{\partial z} = \frac{\mu_0 I}{2\pi z^2}, \quad (3.2)$$

where μ_0 is the magnetic permeability of free space. For a current of 2 A and a bias field of 40 G, the trap is 100 μm away from the surface where the gradient is 4 kG/cm. Moreover this gradient grows quadratically with decreasing wire current at constant bias field. We exploit this feature to trap ultracold atoms at low density in extremely elongated traps to eventually reach the regime where the transverse atomic motion is frozen out due to the strong confinement and the low atomic interaction energy: the gas becomes one-dimensional. This 1D regime requires small atomic interaction energy that can be achieved by reducing the total number of trapped atoms and hence the linear density.

This chapter is organized as follows. After a general discussion on the design criteria in Sec. 3.2, we describe the design and construction of the microtrap in Sec. 3.3. Thermal properties of the microtrap are discussed in Sec. 3.4. In Sec. 3.5 the layout of our ultra-high vacuum system is given, Sec. 3.6 explains the dispenser

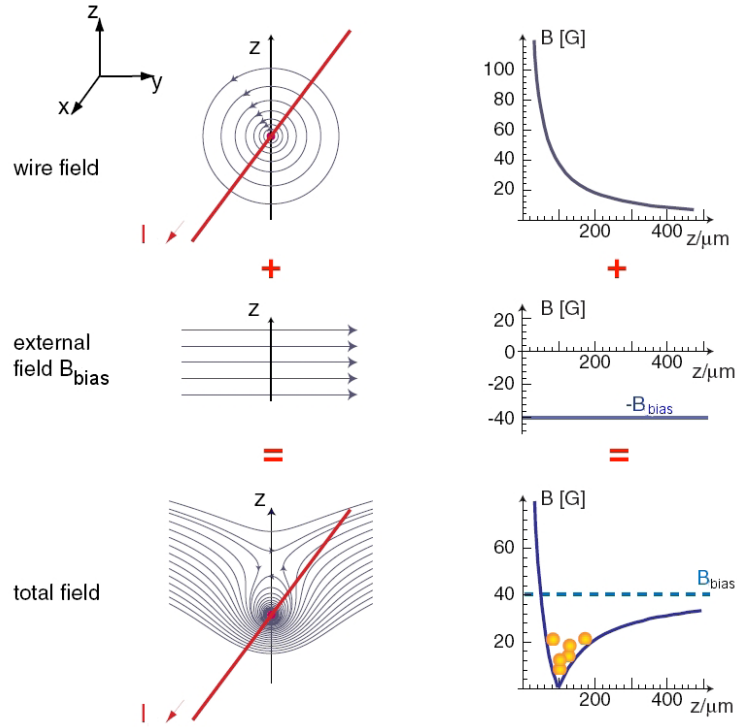


Figure 3.1: Creating a two-dimensional trap with a wire and an external field. Top: wire field, center: external field, bottom: resulting total field. The left-hand column shows magnetic field lines and the right-hand column gives the magnitude of the field at $y = 0$ for a wire current $I = 2$ A and an external field $B_{bias} = 40$ G. In this example, the trap forms at a distance $r_0 = 100 \mu\text{m}$ from the wire axis, and the gradient at the trap center is $|B'(r_0)| = 4$ kG/cm, assuming an infinitely thin wire (Fig. adapted from [101])

atom source. Sec. 3.7 deals with the design and control of the magnetic field coils around the vacuum system. An overview of the laser setup is given in Sec. 3.8. In Sec. 3.9 we give some details on the imaging system including a discussion of the achieved optical resolution and a signal-to-noise analysis. Section 3.10 covers the computer system used to control the experiment. Finally, concluding remarks are given in Sec. 3.11.

3.2 Design considerations

The design of the setup was inspired by two successful experiments on Bose-Einstein condensation in microelectronic traps performed in the year 2001 in the groups of Jacob Reichel in München and Claus Zimmermann in Tübingen [44, 45] and by the work of Schmiedmayer and his group at the university of Heidelberg [102]. Especially the München experiment was attractively simple albeit that only small condensates were obtained. For our design a relatively small number of atoms in the condensate

($\sim 10^4$) was enough to reach our first aim, the study of one-dimensional condensates. In this section some of our design choices that have led to the construction of a stable and productive setup are laid out. For the modelling of the magnetic field we used the *Mathematica* software (Wolfram) with the *radia* add-on that was written at the European Synchrotron Radiation Facility in Grenoble.¹

Single chamber

On a chip, thanks to the strong confinement, BECs can be produced an order of magnitude faster than with conventional traps, in only one second of evaporative cooling. The background-pressure-limited lifetime of a BEC at a pressure in the 10^{-10} mbar range is in the order of 10 s. Efficient loading of a magneto-optical-trap (MOT) requires a partial pressure of at least 10^{-9} mbar. Many experimental setups meet both requirements by connecting two vacuum chambers through a small aperture and maintaining the required pressure imbalance by differential pumping. In that case atoms are magneto-optically cooled at the high-pressure side and subsequently transferred to the low pressure region through the aperture, as was described for example in Kai Dieckmann's thesis [103]. The atoms can be transferred in a beam [14, 104–106] or as a cloud using a magnetic transfer scheme [107, 108]. On an atom chip however, ten times faster cooling, allows a ten times higher background pressure. This takes away the need to load a “BEC”-chamber from a separate “vapor”-chamber. Instead enough pressure difference can be attained by inducing a pressure gradient in time. This was done in ref. [109] by loading the MOT from a pulsed atom source and in ref. [110] using light induced atom desorption. We load our MOT by pulsing a rubidium dispenser. A few seconds after the end of the pulse the pressure has dropped sufficiently to reach BEC in the same vacuum compartment.

Free space versus mirror MOT

We have adopted the mirror-magneto-optical-trap (mirror-MOT) technique that was introduced by Reichel *et al.* [111]. The working of the mirror-MOT is identical to that of the standard 3D MOT [112] the only difference is that the laser beams in the plane of the MOT coils are reflected off a mirror (see Fig. 3.2). Upon reflection the circularly polarized light changes handedness thus maintaining the proper handedness with respect to the quadrupole magnetic field vectors. Using this method limited optical power (≈ 50 mW total) is sufficient to trap and cool enough atoms close to a surface to eventually reach BEC.

Stainless steel versus glass cell

In cold atom experiments worldwide virtually each lab has its own vacuum system and magnetic field coil design. The use of a small glass cell, to perform the main physics experiments in, is popular. It allows a dense packing of magnetic field coils

¹download free at www.esrf.eu/Accelerators/Groups/InsertionDevices/Software/Radia

close to the center of the experiment while sufficient optical access is maintained. In our case the multitude of electrical feedthroughs and the water feedthrough for cooling of the chip, required for our microtrap, makes the use of a single glass cell less straightforward. In the original Munich setup [44] the pumping speed was limited because the chip mount and current leads formed a bottle neck. Besides good access for pumping another advantage of a stainless-steel chamber is the easy use of double-sided AR coating on the windows (difficult for glass cells) that improves the imaging quality. Thirdly the application of wires *in vacuo* to produce strong magnetic-field gradients relaxes the requirements on the proximity of magnetic-field coils considerably. In our case the final reason to choose a stainless steel chamber was the availability of a finished nicely crafted vacuum chamber with an octagonal cross-section (180 mm diameter) that was produced in the Huygens Laboratory, Leiden, The Netherlands [113]. This chamber gives ample optical access and provides for the easy connection of many electrical feedthroughs.

A very elegant alternative approach was followed by the group of Jacob Reichel in a new generation of experimental setups where they have replaced the top cover of their cell with an already connected microchip [114] combining easy connection, good optical access and the possibility of cooling the chip without compromising the pumping speed.

Efficient and reproducible chips enable wider applicability

The development of efficient and reproducible “atom chips” could facilitate the quick setup of new cold-atom experiments world wide at a reduced cost. In this way more researchers could do experiments on ultracold atoms: physical systems that are governed completely by quantum mechanics. Such a development would bring the world of quantum mechanics closer to our daily experience.²

Advantages of scale reduction

Another advantage of the use of small current-carrying wires to trap atoms is the dynamical flexibility. It is easy to rapidly switch off 2 A of current in a chip wire because of the low resistance and low inductance. This is in sharp contrast to the high voltages needed to push down the hundreds of amperes of current in the large coils used in conventional BEC machines. The chip wires can be switched rapidly in about 30 μ s limited by the current source bandwidth, contrarily the magnetic bias fields that are generated by the outside coils have a relatively long switching time of 1.2 ms limited by the current source voltage. The chip setup allows also to economize on the lasers because small BEC’s are efficiently produced from modest initial atom numbers. There is no need for a high power tapered-amplifier diode or a titanium-sapphire laser. In our setup for example we use only three simple diode lasers. By keeping the laser setup small we reduce costs but we also reduce the man hours of maintenance. The complete setup involves only one optical table with

²An example of such an initiative is the on-line atom chip experiment in Germany (www.physnet.uni-hamburg.de/ilp/sengstock/en/ELearning.php).

room for both the lasers and the vacuum system with the atom chip, with a total footprint of only 4 m².

Formulation of design criteria

In the design process, that involved three successive test traps before reaching the final microtrap, we have identified the following essential elements:

- The magnetic trap should have a large enough capture volume,
- The trap should provide an adequate mode match with the optically cooled atom cloud.
- To start evaporative cooling the atomic collision rate should be raised. This is achieved by increasing the magnetic field gradient. During this compression the trap should always be deep enough so that the heated atoms are not squeezed out of the trap.

From these key requirements we can derive typical values for the currents to be used in the wire layers. The required currents in turn impose constraints on the thermal properties of the microtrap.

3.3 Microtrap for cold atoms

The core of the experimental setup is formed by the microtrap for cold atoms shown in Fig. 3.2(a). This trap consists of three layers of current-carrying wires. The surface layer is formed by a silicon substrate coated with a patterned gold layer. On this “atom chip” a Z-shaped wire is defined that is usually operated at a current of 2.25 A. Behind the substrate are two layers containing three parallel copper wires each, in the x and y -direction, respectively. These “miniwires” have a diameter of 300 μm and typically run at 10 A. The design and development of the microtrap assembly formed by the chip, the miniwires and their mount was the crucial and most innovative step in the buildup of our experimental setup.

Microtrap elements – mirror-MOT

For the effective implementation of a mirror-MOT the mirror should reflect the cooling laser beams under a 45° angle without birefringence. Metallic coatings are well suited for this purpose. Our metal of choice is gold because it has a high reflectivity of $\approx 98\%$ at 780 nm, it does not oxidize like silver or aluminium and it has a similarly high electrical conductivity necessary for the on-chip wires. The surface dimensions of the chip (16 \times 25 mm) are adjusted to the diameter of the MOT beams.

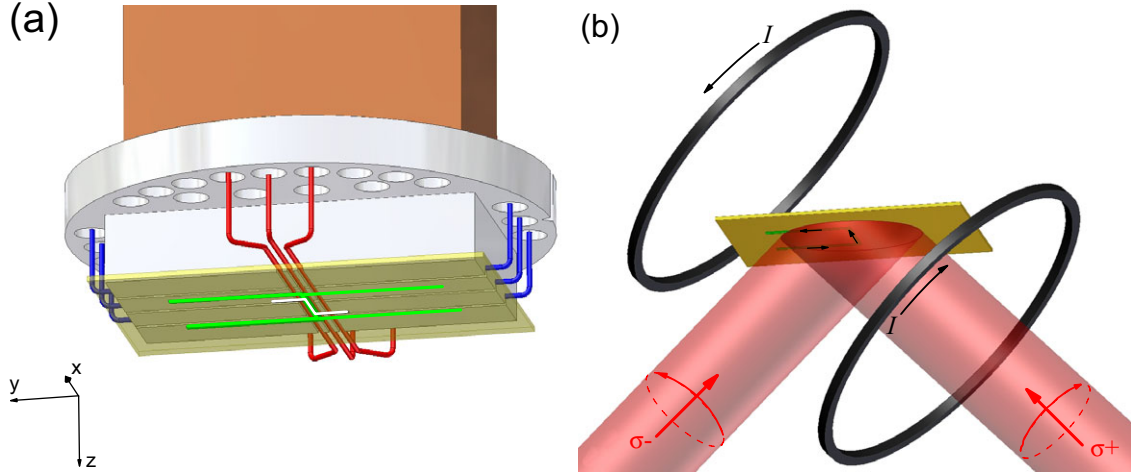


Figure 3.2: (a) Chip mount with orientation of the two layers of miniwires (blue and red), the orientation of the H-current is indicated in green and the position of the on-chip Z-wire in white. (b) Schematic of the mirror-magneto-optical-trap. Cooling light beams in the yz -plane reflect on the chip surface (beams along x are omitted for clarity). The handedness of the circular polarization is indicated with the red arrows (σ^+ and σ^- are defined in the propagation direction of the light). The course of the H-current is indicated in green. The quadrupole coils are shown in black. Black arrows indicate the current direction.

Microtrap elements – wire-MOT

We start the trapping and cooling process with a mirror-MOT stage where the quadrupole magnetic field is generated by the MOT coils (see 3.7). In a second step we replace this quadrupole field by a magnetic field that is generated by the miniwires, the wire-MOT stage. The proper magnetic field is essentially generated with a current I on the surface of the mirror that follows a H-shape (green line in Fig. 3.2) and a homogeneous bias field B_y along y . The central section of the H in the x -direction together with B_y form a side guide along x . We estimate the trap position and gradient using Eq. (3.1); with a current of 10 A along x [equally divided over three parallel red wires in Fig. 3.2(a)] and $B_y = 5$ G we find the trap minimum at $z_0 = 4$ mm where the gradient is 12.5 G/cm. The wire sections of the H that run in the y -direction provide a confining gradient along x . The currents in the “legs” of the H run in opposite directions. Therefore the magnetic field is zero in the trap center and the field lines point outwards in the xz -plane for positive z . In a volume of radius z_0 the magnetic field resembles the ideal quadrupole configuration for a MOT reasonably well. For $z_0 = 4$ mm this volume is comparable to the volume where the cool light beams intersect.

Microtrap elements – magnetic trap

After the optical cooling stages we magnetically trap the atoms in a Ioffe-Pritchard (IP) magnetic field configuration (see Sec. 2.2). For the IP field we invert the current in one of the miniwires along y [blue wires in Fig. 3.2(a)] thus turning the quadrupole field into an IP-field configuration. In the subsequent stage we transfer the atoms to the on-chip Z-wire [white wire in Fig. 3.2(a)] that provides a strongly confining potential. In this stage the miniwires are only used to give small corrections to the fields and gradients and eventually to generate the focusing pulse used for experiments described in Chapters 5 and 6.

3.3.1 Layout and construction

In the description of the wire pattern layout we refer to the frame of reference in Fig. 3.2, where the center of the chip surface is at the origin. A detailed drawing including the dimensions of the boron nitride ceramic disc is shown in Fig. 3.3(b). The 300- μm -diameter Kapton-coated copper miniwires run along x and y in two layers centered at $z = -0.5$ mm and $z = -0.8$ mm respectively. The spacing between the wires within one layer is 0.65 mm and 3 mm, for the wires along x and y respectively. These wire layers exactly fit in grooves in the boron-nitride ceramic disc that is machined with a CNC computer-controlled mill. An exploded view of the chip mount parts is shown in Fig. 3.3(a). We machine our ceramic disc from boron-nitride because it is as easily machinable as Macor but has a thermal conductivity that is 20 times higher.

All parts are bonded with Epo-tek H77 epoxy except for the silicon substrate that was glued to the boron-nitride ceramic with Epo-tek 377. The miniwires are electrically connected using standard vacuum-compatible sub-D-type gold plated connector pins. We strip the Kapton from the end of the miniwire and press it, along with a piece of bare copper, into the male pin. The resistance of the miniwires (including the connection to the male pins) is 10 m Ω . With a current of 10 A typically 1 W per wire is dissipated over the whole length of the wire resulting in negligible heating. At a current of 20 A the wire sections that are suspended in free space between the connector pins and the ceramic disc start to heat up moderately. All copper elements used in the microtrap assembly are made of oxygen-free high-conductance (OFHC) copper. The copper heat sink is connected with four bolts (M3) to the end cap of a stainless-steel (type 316L) rod with an outer (inner) diameter of 16 mm (8 mm). This rod is welded to a CF40 flange for insertion into the vacuum system. A polyvinyl chloride (PVC) tube of 6 mm diameter runs coaxially inside the stainless-steel rod. Cooling water enters the system through the inner (PVC) tube. Water flows out of the tube towards the stainless-steel to copper interface, where it removes heat from the microtrap assembly, before flowing back on the outside of the PVC tube. We typically run 0.1 l/min of tap water through the system.

The gold-coated silicon substrate or “atom chip” was produced using the facilities of the Amsterdam nanoCenter (located at AMOLF, the FOM Institute for Atomic

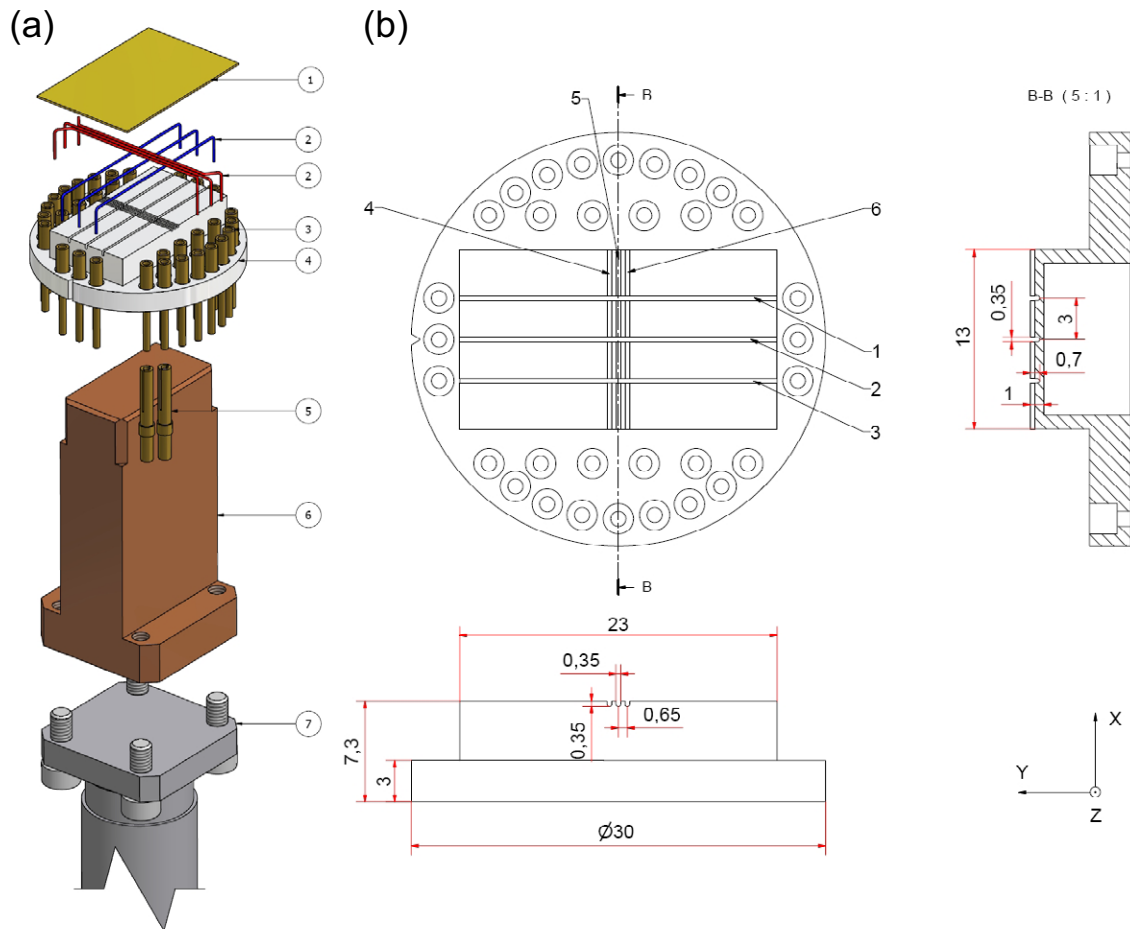


Figure 3.3: (a) Exploded view of chip mount. (1) silicon chip with gold layer; (2) miniwires; (3) connector pins (male); (4) Boron-Nitride ceramic element; (5) female connector pin; (6) copper heat sink; (7) water-cooled stainless steel rod. (b) Dimensions of boron-nitride ceramic disc. The exact position of the miniwires and their numbering is indicated. All sizes are in mm.

part	description	supplier
electrical feedthrough	Sub-D 15 pin	Allectra
D-sub connector pins (fe)male	gold plated	Allectra
Kapton insulated wires	1mm diameter	Allectra
Kapton insulated wires	0.3mm diameter	Allectra
boron-nitride ceramic	high purity grade	Saint Gobain
UHV compatible epoxy	low outgassing	Epo-tek H77/377

Table 3.1: Parts used in the microtrap assembly and their supplier.

and Molecular Physics). The production will be described in detail in the forthcoming thesis by J.J.P. van Es [115]. Here we describe the production process only briefly. Furthermore the treatment of the wire layout is restricted to the 125- μm -broad Z-wire that was used for all experiments described in this thesis. A few of the

eight other wires present on the chip were employed during the work described here. Especially one neighboring wire was used as an antenna to perform radio-frequency evaporative cooling. A 300- μm -thick high-purity silicon substrate is covered with two layers of different types of photo-resist resulting in a total layer thickness of $\sim 2 \mu\text{m}$. The resist is exposed to UV-light through an optically patterned mask (produced at MESA+, University of Twente, The Netherlands). Developing the double resist layer results in a resist pattern that has an undercut. A very smooth 1.8- μm thick gold layer is deposited onto the substrate using vapor deposition. A lift-off procedure, that is facilitated by the undercut in the resist, finally shows the wires that are defined by $\geq 5\text{-}\mu\text{m}$ -wide gaps in the gold layer. We use a Z-shaped wire because it is the most simple way to generate a IP field configuration with a single wire and a bias field [116]. In addition, such a Z trap can be easily compressed by increasing the bias field B_y . If we compress in this way, the trap is automatically deep enough and the heated atoms are not squeezed out. In our first chip design we incorporated only very elongated traps made of narrow wires, as a result the radial compression was too high and the axial trap depth too low to achieve high enough atom number and density to reach BEC. The Z-wire height is fixed at 1.8 μm by the chip production process. In choosing the width w and length d of the central section of the Z-wire we have to make a compromise between on the one hand high attainable trap frequencies (small w) and a large trapping volume (large d and large I) while ensuring on the other hand to keep the ohmic heating within bounds (small d , small I , large w). Our resulting Z-wire is shown in Fig. 3.4; it has a 3-mm-long 125- μm -wide central section with leads that fan out, thus limiting the total resistance to 0.7 Ω . This low resistance allows us to run a relatively high current of 2.25 A through the wire without overheating the chip thus ensuring a large enough trap volume.³ At this current and with a 40-G bias field the trap minimum sits at $z_0 = 90 \mu\text{m}$ where the gradient of the magnetic field is 3.7 kG/cm. An excellent starting point for evaporative cooling.

Assembly

In the assembly process special care is taken to create optimal epoxy adhesion layers. The two epoxy components were carefully weighted on a precision balance and mixed. We heat the mix to $\approx 40^\circ\text{C}$ to decrease the viscosity. This mixture is degassed in a desiccator for one minute. Keeping the epoxy for longer in vacuo harms the mixture because essential chemical components get extracted. The epoxy was cured in air at 150°C for 1 hour. During the warm up trajectory the epoxy becomes very fluid and tends to creep onto the mirror surface. To prevent this from happening the chip edges were designed to extend 1 mm over the supporting boron-nitride layer. In Fig. 3.5 we show some pictures taken during the construction process of the microtrap.⁴ The assembly process is performed in several curing stages. In

³An order of magnitude higher current density was reached with a total current of 1 A in a 5- μm -wide chipwire: $10^{11}\text{A}/\text{m}^2$.

⁴Large part of the chip mount production was performed by the fine-mechanical engineer W. van Aartsen at the University of Amsterdam.

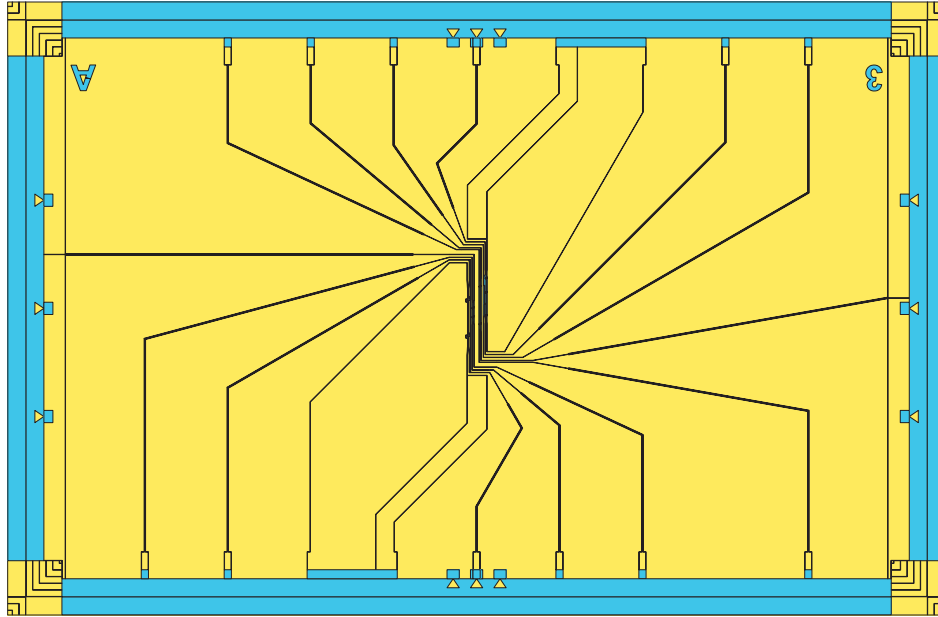


Figure 3.4: Layout of the chipwires, dimensions of the chip are $25 \times 16 \text{ mm}^2$.

the first curing stage the ceramic disc is glued onto the copper heat sink and the connector pins for the chip wires are glued in place. In the subsequent curing stage the miniwires and their connector pins are glued into the groves in the ceramic disc. After removing the excess epoxy with a mill and careful cleaning we place a drop of Epo-tek 377 in the middle of the ceramic disc and glue the microchip on it in the last curing stage. We press the chip in its exact position with a special mold and a weight that has only 3 needle-like contact points with the chip to do minimal damage to the very soft gold layer. The alignment error of the on-chip Z-wire with respect to the miniwires achieved in this way was smaller than $50 \mu\text{m}$. The eight on-chip wires are connected to the contact pins with $20 \mu\text{m}$ -diameter aluminium wires with a wire bonding technique.⁵ Each contact pad was bonded with 10 wires except for the Z-wire where we have used 14 wire bonds. The microtrap wires are then connected to a set of sub-D-type vacuum feedthroughs. The maximum bake-out temperature for the chip mount in the vacuum system is limited to $180 \text{ }^\circ\text{C}$ by the Kapton around the copper wires and the used epoxy. After bake out, the chip mount was compatible with ultra high vacuum conditions as expected; the experiment is operated at a pressure of 10^{-10} mbar.

⁵Wire bonding was performed by J. Rövekamp at the National institute for subatomic physics (NIKHEF) in Amsterdam.

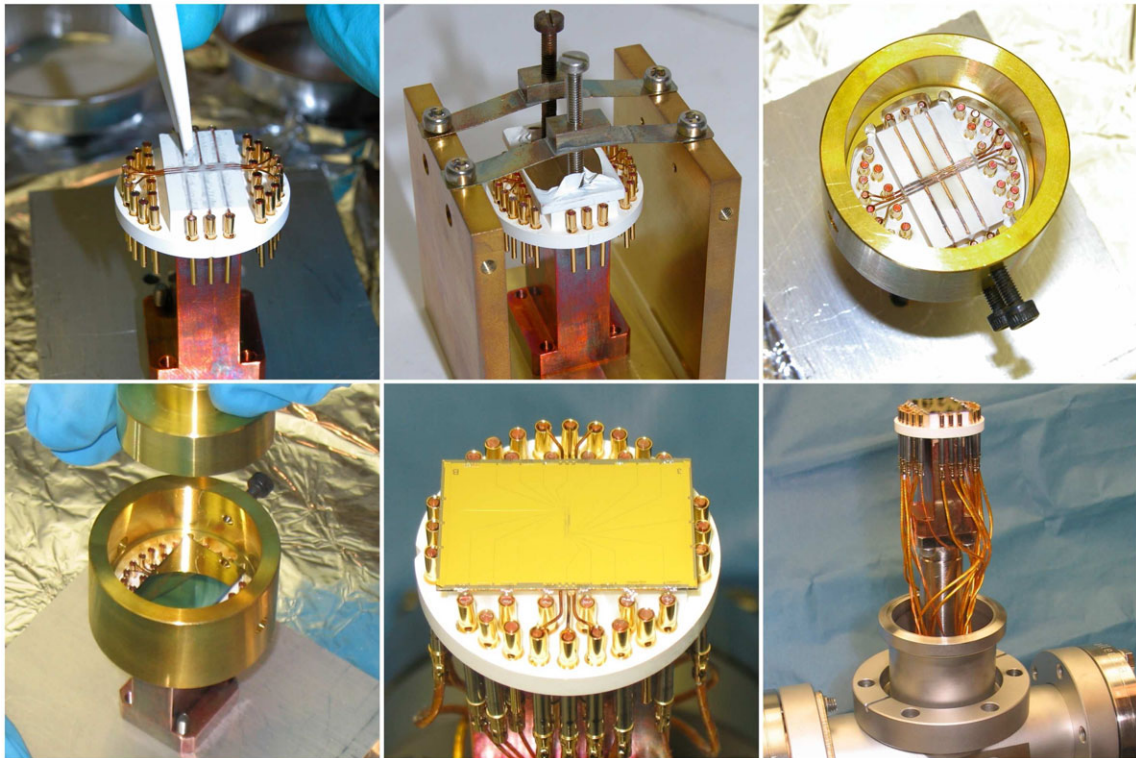


Figure 3.5: Snapshots of the construction process of the microtrap. Top row (from left to right): gluing the miniwires into the grooves in the boron-nitride ceramic. Miniwires are pressed in place for a curing stage. Microtrap assembly with another pressing mold just before the placement of the microchip. Lower row (from left to right) removing the weight that pressed the chip in place while curing. Resulting chip mount with all eight chipwires wire-bonded to their connector pins. View of the microchip assembly after complete wiring to the vacuum feedthroughs.

3.4 Thermal properties of the microtrap

For the design of the microtrap assembly an analysis of the thermal properties was performed. We measure a steady-state total thermal resistance of 10 K/W when we send a current through the on-chip Z-wire and cool with a water flow of 0.1 l/min. Measurements of the steady-state thermal resistance of the mount and of the heating as a function of time were reproduced by a Finite Element Method (FEM) simulation and were compared to an analytic study of the heat flow through the chip mount [117]. In Sec. 3.4.1 we use the heat equation to get an analytic handle on the FEM simulation results that are presented and discussed in Sec. 3.4.2.

3.4.1 Thermal conduction – analytic approach

Heat flow in a homogeneous medium, characterized by its specific heat c , density ρ and thermal conductivity σ , is described by the heat equation

$$\frac{\partial T}{\partial t} = \frac{c}{\rho\sigma} \nabla^2 T. \quad (3.3)$$

We look for solutions to this partial differential equation for a model system that represents the microtrap assembly. Figure 3.6 illustrates the dimensions used in describing the finite system of length l . The area S is equal to that of a heat source, in our case a gold layer of width w and length d of which the thickness h determines the resistance. In a system that is symmetric around an axis (z) the heat equation can be solved using Fourier series [118]. From the Fourier series we can obtain estimations of the thermal behavior in two limiting cases where the heat flow is approximately symmetric around z : (i) close to the wire in the regime $(l - z) < w \ll d$; (ii) for large distances $(l - z) \gg d$. We write the solution to the heat equation in one dimension. At position $z = l$, a constant power P is dissipated, while at $z = 0$ the temperature is kept constant

$$\delta T(z, t) = \frac{P}{\sigma S} z + \sum_{n=1}^{\infty} A_n \sin k_n z e^{-\gamma_n t}, \quad (3.4)$$

$$\gamma_n = \frac{\sigma}{\rho c} k_n^2, \quad k_n = \frac{(2n - 1)\pi}{2l}. \quad (3.5)$$

Here A_n are the Fourier coefficients and k_n the wavevectors. The first term in Eq. (3.4) gives the stationary solution for $t \rightarrow \infty$, while the temporal evolution is expressed through the relation between the relaxation constant γ_n and the wavevector k_n . From the relation Eq. (3.5) we see that the relaxation time γ_n^{-1} increases with the square of the wavelength $2\pi/k_n$ of the contributing Fourier component. Equation (3.4) gives access to comprehensive estimates for the stationary and dynamical thermal properties of our chip mount. These estimates can be used to gain insight in the more realistic FEM analysis.

(i): At small distances, close to the gold-silicon interface [$(l - z) < w \ll d$], we have the simple case of one-dimensional flow and the stationary term in Eq. (3.4) yields for the thermal resistance $R_t = \Delta z / \sigma S$ in a layer of thickness Δz . Let us assume that this homogeneous heat flow approximation holds for depths up to $w/2$. The thermal resistance of such a silicon layer is then 1 K/W with $w = 125 \mu\text{m}$. An estimate for the time constant for the heating of this layer can be found from Eq. (3.5). The Fourier component with the longest relaxation time $\gamma^{-1}(k)$ corresponds to $k = \pi/w$ and by inserting the values for silicon (Table 3.2) we find a relaxation time of $\sim 20 \mu\text{s}$. Thus, this thin silicon layer heats up on a timescale much faster than the timescale of the experiment and the steady-state value forms an inevitable lower bound on the thermal resistance if we use silicon as a substrate.

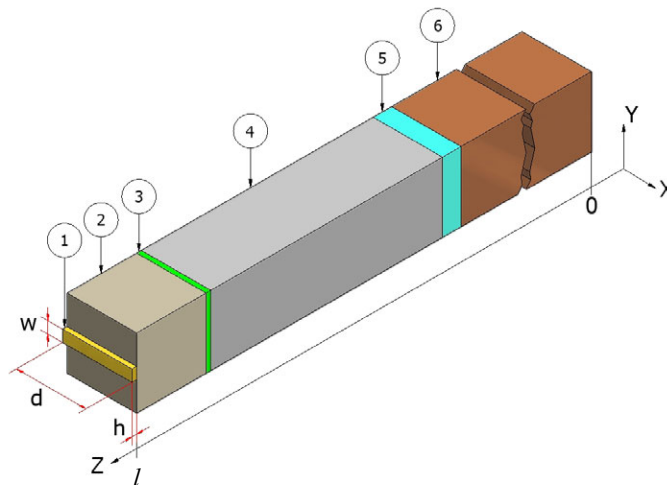


Figure 3.6: Schematic drawing (not to scale) of the chip mount indicating the layer structure and the dimensions used for the thermal analysis. Some properties of the layers are listed in Table 3.2. The dimensions can be found in Table 3.3.

Fig. 3.6	material	heat conductivity σ [W/Km]	specific heat c [J/kgK]	density ρ [kg/m ³]
(1)	gold	300	132	$19.3 \cdot 10^3$
(2)	silicon	148	710	2330
(3)	Epo-tek 377	0.2	$1.0 \cdot 10^3$	1175
(4)	Boron Nitride	27	1468	1900
(5)	Epo-tek H77	0.66	$1.0 \cdot 10^3$	$2.5 \cdot 10^3$
(6)	copper	400	385	8920

Table 3.2: some physical properties of the materials used for the fabrication of the microtrap.

(ii): In the limit of distances large compared to the radial dimensions $[(l - z) \gg d]$ we look at the heating of the total mount, also an approximately one-dimensional problem. An estimate for the heating time constant is found again from Eq. (3.5). The largest part of the mount is formed by the copper heat-sink of length 40 mm. We insert the values for copper (Table 3.2) and find a relaxation time of 6 seconds.

For intermediate distances $w \lesssim (l - z) \ll d$ the heat flow problem has to be treated in two dimensions. At this distance range (and within the silicon) the system can be approximated by a line-like heat source of infinite length on a silicon half-space substrate. The temperature increase at the gold silicon interface as a function of time is then given by the incomplete gamma function [119]

$$\delta T(t) = \frac{hw\rho_e j^2}{2\pi\sigma} \Gamma\left(0, \frac{cpw^2}{4\pi^2\sigma t}\right), \quad (3.6)$$

where j is the current density, ρ_e is the electrical resistivity, and h is the wire thickness. This function is plotted in Fig. 3.7(b).

3.4.2 Thermal conduction – Finite Element Method

For a more detailed three-dimensional study of the thermal properties of our chip mount design a finite element method (FEM) simulation was performed using the MSC-Marc software package [117]. The chip mount was modelled with 2500 elements where the smallest elements near the heat source have a size of $2 \mu\text{m}$. The chipwire was simulated by imposing an uniform heat load at the wire surface area of $125 \times 3000 \mu\text{m}^2$. The modelled layers from top to bottom and their respective thickness are listed in table 3.3. A three-dimensional image of a quarter section of the modelled mount with the equilibrium temperature distribution for 1 W heat load is shown in Fig. 3.7(a). The epoxy layers with their low thermal conductance form a distinct barrier for the heat flow to the next layer. The heating process after the heat load is turned on is also calculated dynamically. The temperature rise at three positions on the symmetry axis is shown in Fig. 3.7(b). The equilibrium values for the thermal resistance of the modelled layers at the symmetry axis are listed in table 3.3. Two values for the thickness of the Epo-tek 377 layer were simulated because this thickness is not exactly known experimentally. The measured value for the total thermal resistance is $9.9 \pm 0.1 \text{ K/W}$. The dynamic FEM results [Fig. 3.7(b)] show that in the first 6 ms (inset) the temperature at the silicon-gold interface is already at half its final value, and that the realistic heating exceeds that of the analytic expression for a semi-infinite silicon slab of Eq. (3.6) already within the first millisecond (as expected from the Fourier analysis). On the long timescale of 6 s we see that only the copper is still getting warmer (in agreement with the Fourier analysis) but that the total equilibrium value is approached already to within 3%. This dynamical behavior was found to be in qualitative agreement with measurements performed on a neighboring chipwire with a smaller width of $10 \mu\text{m}$ for times between 10^{-4} s and 10 s. What is the relevant process for our experimental situation? One experimental cycle takes a constant 10 s or 20 s and is repeated typically more than 20 times. This cycling together with the constant flow of cooling water through the chip mount will guarantee a constant long-term temperature stability of the microtrap. The current pulses through the chipwire take ~ 1 s or longer by which time the steady-state situation is almost reached. *We conclude that for our purposes the value of the steady-state thermal resistance is the relevant quantity that has to be minimized in our design.* The epoxy layer that bonds the silicon substrate to the boron-nitride ceramic layer forms the largest contribution to the total equilibrium thermal resistance (see table 3.3). Therefore this epoxy layer was the focus of our attempts to improve the total thermal conductance of the mount. Our favorite epoxy that we use in other parts of the mount (Epo-tek H77) is filled with ceramic grains to increase the thermal conductivity. These grains with a diameter of $\approx 20 \mu\text{m}$ make it impossible to create thin layers. We therefore employed the same type of epoxy with proven low outgassing rate but without the filler (Epo-tek 377) to bond the silicon layer to the boron-nitride ceramic. We have tested Epo-tek 377 by

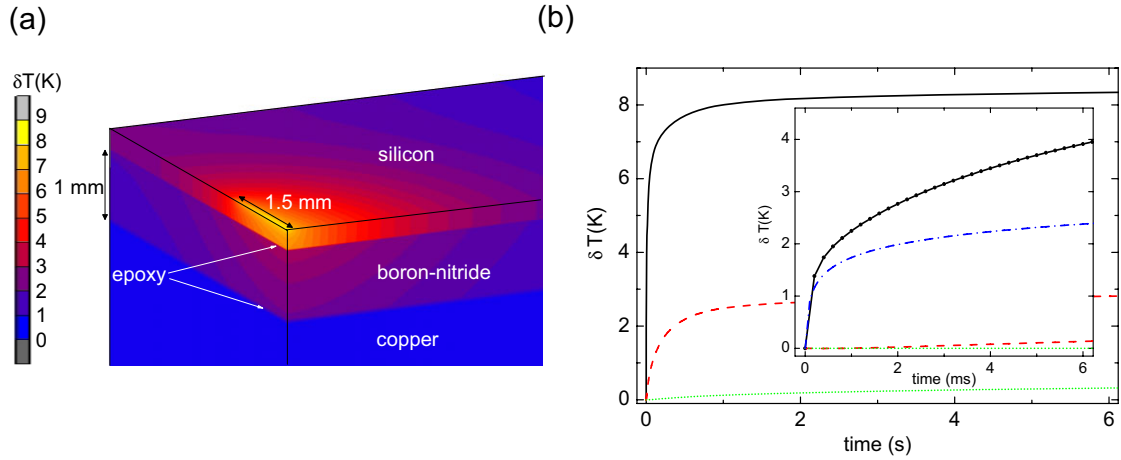


Figure 3.7: (a) Finite element method simulation of thermal properties of the chip mount. Shown here is a quarter section of the mount with the equilibrium temperature distribution for a heat load of 1 W generated at the gold wire location. The modelled layers from top to bottom are silicon, Epotek 377 ($20 \mu\text{m}$), boron-nitride, Epotek H77 and copper. The epoxy layers with their low thermal conductance clearly form a barrier for the heat flow to the next layer. (b) Dynamic thermal results of the finite-element-method simulation. Shown here is the temperature increase in the first 6 s after a heat load of 1 W at the gold wire location is turned on for three positions on the symmetry axis: silicon-gold interface (black straight line), boron-nitride-Epotek 377 interface (red dashed line) and copper-Epotek H77 interface (green dotted line). The inset shows a zoom of the first 6 ms. Here the curve for the incomplete gamma function, Eq. (3.6), that models an infinite silicon layer is shown for comparison (blue dash-dotted line). This comparison shows that already in the first millisecond the heat flow has encountered the first epoxy layer and the heating is faster than for the case of the semi-infinite silicon slab.

bonding microscope slides and studying the layer homogeneity and thickness under an optical microscope. Spreading the epoxy (prepared as described in Sec. 3.3.1) over one of the surfaces followed by curing of the bond under pressure resulted in the inclusion of air bubbles in the epoxy layer. An almost perfectly homogeneous filling was obtained when a drop of epoxy was deposited in the middle of one of the parts before putting the parts together under pressure. The “smearing” method resulted in a layer thickness of $25 \mu\text{m}$. The “drop” method resulted in thin layers of $12 \pm 3 \mu\text{m}$ and was used for the fabrication. The layer thickness achieved in the final chip mount fabrication could not be measured. We assume that the Epo-tek 377 layer is thicker than the test results because the (mechanically milled) boron-nitride surface is less smooth than that of the microscope test slides. We had to apply more epoxy per bonded area than was used for the tests. We estimate the layer thickness between $20 \mu\text{m}$ and $80 \mu\text{m}$. These thicknesses were used in the FEM simulation results. Within the simulated range the FEM thermal resistance agrees quantitatively with the measured value. The accuracy of the measurement and simulation of the thermal conductance do not allow to establish the thickness of the first epoxy layer with good accuracy. The important contribution to the total thermal resistance

layer	thickness [μm]	R thermal [K/W]	thickness [μm]	R thermal [K/W]	R thermal measured [K/W]
silicon	300	1.6	300	1.5	
Epo-tek 377	20	4.0	80	7.3	
boron-nitride	1000	0.9	1000	0.4	
Epo-tek H77	80	1.6	80	1.1	
copper	$40 \cdot 10^3$	0.4	$40 \cdot 10^3$	0.4	
total	$41 \cdot 10^3$	8.5	$41 \cdot 10^3$	10.7	9.9 ± 0.1

Table 3.3: Thermal resistance of constituting chip mount layers from FEM simulation compared to the experimentally measured value. Simulations were performed for 20 μm and 80 μm thick Epo-tek 377 layers. The experimentally measured value is shown in the last column.

however suggests that we can still improve the performance, for example by finding an epoxy that is a better thermal conductor or finding a way to make thinner layers.

3.5 Vacuum system

Our vacuum setup is shown in Fig. 3.8 [113]. It is built up around a science chamber with an octagonal cross section (1). The octagon contains both the microtrap (8) and dispenser atom sources (9). Ultra high vacuum (UHV) conditions are maintained using the combination of an ion getter pump (IGP) (6) and a titanium sublimation pump (TSP) (5). Both are located in the pump section that can be separated from the science chamber with a gate valve (3). The pressure can be monitored with a Bayard-Alpert type ionization gauge (7). The microtrap is connected with a custom-made 4+1-way cross (10) that is pumped with an additional small ion-getter pump (11). The science chamber and the pump section can be separately evacuated using a turbo molecular pump through valves (2) and (4) respectively. A 100-W halogen light bulb is positioned in the science chamber to aid the bake out. All parts are made of the commonly used stainless steel type (304) except for the science chamber, the 4+1-way cross and the chip mount where we have used the less magnetic stainless steel type (316L).

Seven glass windows give optical access to our vacuum chamber. Five CF40 windows, with a double sided AR coating, are centered at $x = 0$ in the yz -plane. A sixth CF40 window is centered at the x -axis and is placed at the backside of the vacuum vessel. The CF100 window that seals off the front side of the octagon is uncoated. The conductance from the science chamber to the 5-way cross at the center of the pump section is about 30 l/s justifying the choice of an ion getter pump with a pumping speed of 40 l/s (Physical Electronics 2082040, controller: Perkin and Elmer Digitel 500). The addition of a Titanium sublimation pump (Varian 916-0061, controller: Varian 929-0023) increases the pumping speed for reactive elements but does not pump noble gases. The pressure is monitored with a Bayard-Alpert type ionization gauge (Varian UHV-24p, controller: Varian). We can close the gate

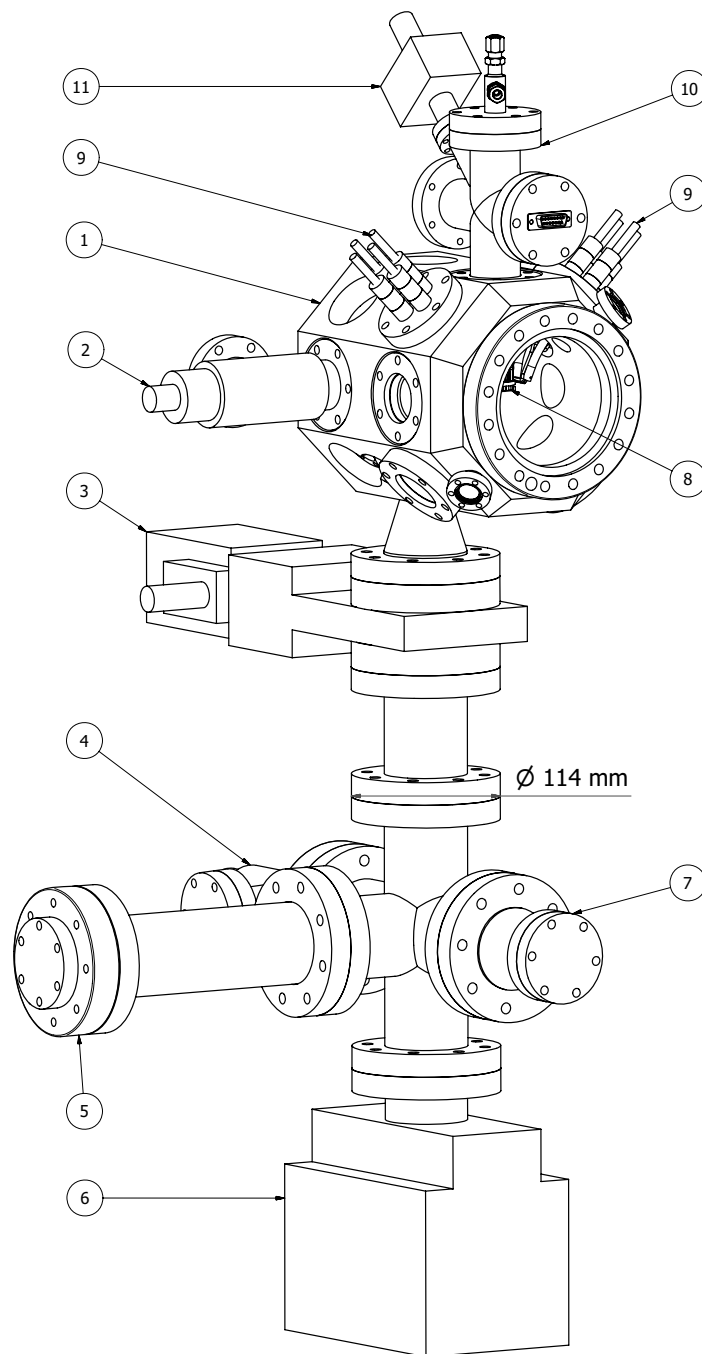


Figure 3.8: Vacuum Setup: (1) science chamber, (2) and (4) venting valves, (3) gate valve, (5) Ti sublimation pump, (6) ion getter pump 40 l/s, (7) ion gauge, (8) microtrap, (9) dispenser atom source, (10) 4+1-way cross, (11) ion getter pump 2 l/s. The scale of the figure is indicated using the size of a central flange.

valve (VAT 10836-CE01) to preserve vacuum in the pump section while opening the science chamber to replace the chip mount or the atom dispensers. Both sections can be evacuated with a turbo pump through *all-metal* valves (Varian). We pump the 4+1-way cross with the chip mount and its electrical feedthroughs with an extra 2 l/s ion getter pump (Varian 919-0520, controller: Varian minivac) to be sure that this remote piece does not act as a virtual leak.

We reach a vacuum pressure in the 10^{-11} mbar using the following procedure.⁶ We clean all vacuum parts in an ultrasonic bath first with acetone and then with ethanol. Secondly we use materials with low outgassing rates in the microtrap design (see Sec. 3.3). After assembly we perform a vacuum bake out at a temperature of 180 °C limited by the Kapton insulation of the minitrap wires and the two types of UHV compatible Epoxy (Epotek H77 and 377) used in the minitrap. The octagonal chamber was opened several times to exchange the minitrap and the dispensers while maintaining UHV in the pump part by closing the gate valve. We typically bake during seven days while pumping with a 63 l/s turbo-molecular pump (Pfeiffer). We then combine the turbo with IGP pumps. Subsequently we valve off the turbo pump and let the system cool down. We then start the TSP and let it fire during one minute at 47 A each 32 hours. This procedure leads to a pressure below the sensitivity limit of the ion gauge, this indicates a pressure of $\approx 10^{-11}$ mbar.

3.6 Dispenser pulsed atom source

We use a non-evaporable getter as a source for rubidium atoms. These so-called dispensers are commercially available (*SAES Getters*) and are widely used in cold-atom experiments [109]. The dispensers used in our experiment are centimeter-sized stainless-steel containers filled with rubidium chromate and a reducing agent. Rubidium atoms are released when the reduction reaction is initiated upon heating the container above a threshold temperature (600 °C for cesium [120]). We heat the dispenser resistively by applying a current pulse of 11-20 A during 2-4 s.⁷ Heating and cooling down can be achieved in this way within 5 s thus altering the gas pressure on the same timescale. The dispensers used in our experiment have an active length of 12 mm and contain ~ 4.5 mg of Rb. We found only one study in the literature detailing on the flux from alkali dispensers [120]. Succi and coworkers quote a cesium flux at 5 A dispenser current of 10 mg/min. If this flux can be compared to the Rb case (not specified anywhere) the dispenser would be empty after 450 minutes of continuous operation. Our dispensers were used extensively for about one year and were not empty at the time of replacement. We have mounted our dispensers close to the atom chip on a thick copper high-power vacuum feedthrough (*MPF AO756-1-CF*, 4-pin power feedthrough copper conductors 23A; 1250V). The assembly is shown in Fig. 3.9. The 6.4-mm-diameter copper rods allow the essential rapid cool

⁶N.B. all pressure readings are at the position of the ionisation gauge unless explicitly stated otherwise.

⁷The exact pulse shape and duration depend on details of the experiment like the exact cycle time.

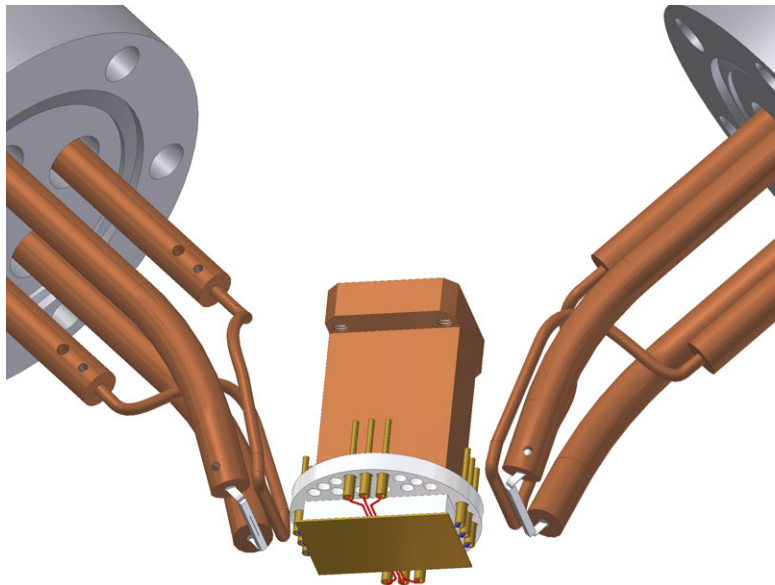


Figure 3.9: Two dispenser atom sources on CF-40 UHV feedthroughs shown with their orientation with respect to the microtrap. The size of the chip is $25 \times 16 \text{ mm}^2$. Note that the orientation of the dispensers was changed prior to the experiments of Ch. 4-6 (see text for details).

down of the dispenser after the end of the current pulse. The opening slit of the dispenser is placed close to the chip but the direct line of sight to the center of the MOT is blocked by the rim of the microtrap assembly to prevent a harmful stream of hot atoms from passing through the cold cloud. A bare copper wire runs parallel to the dispenser with counter-propagating current to minimize the generated magnetic field at the position of the MOT. In our setup that was operated in the years 2006/2007 we have pointed the opening slit of the dispensers in the opposite direction facing away from the MOT. By mounting the dispensers in this way we avoid a possible coating of the chip mount with Rb. *In initial experiments we had noticed that Rb atoms that had stuck to the microtrap assembly would desorb from the microtrap during the magnetic trapping stage at the moment the assembly heats up. These desorbed Rb atoms had a detrimental effect on the magnetic trapping lifetime.* Changing the direction of the rubidium atom beam emerging from the dispenser had no effect on the number of atoms that we could trap in the MOT. The problem of the decreased trap lifetime due to desorbed rubidium was completely solved in the most recent setup where we (i) directed the Rb beam away from the chip; (ii) reduced ohmic heating by reducing the chipwire resistance and improving the thermal conduction of the chip mount and (iii) heated the chip mount to 40°C at moments that the experiment was not running to clean the chip mount from possible Rb contamination. This heating is done by circulating warm water through the cooling water circuit (circulating bath *Tamson TC6B*).

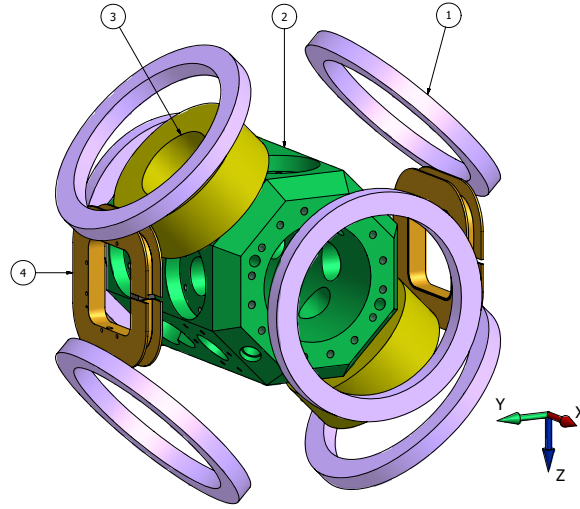


Figure 3.10: Magnetic field coils: (1) compensation coils, (2) vacuum chamber, (3) MOT coils, (4) bias coils. The outer diameter of the six outside coils is 200 mm.

Light-induced atom desorption

To change the pressure even more rapidly one can use light-induced atom desorption (LIAD) in addition to the dispensers [110, 121]. For LIAD a strong halogen light bulb or a LED that emits in the near UV is switched on during the MOT loading stage to desorb atoms from the vacuum system surface [121]. The efficiency of this method is determined by the ratio of the illuminated surface area to the total vacuum system area. This ratio can be made optimal for glass vacuum cells more easily than for stainless steel chambers. We have performed promising preliminary studies using a light emitting diode array with diodes that emit 700 mW of blue light with a central wavelength of 455 nm (Luxeon V Star royal blue), illuminating the inside of the science chamber through the big CF100 window (Fig. 3.8). Until the time of writing we had not enough reason however to change the current working setup based on pulsed dispensers.

3.7 Magnetic field coils

Figure 3.10 displays the magnetic field coil configuration around the vacuum chamber. These coils are used, together with the microtrap wires, for magneto-optical and magnetic trapping, and manipulation of cold atom samples. All coils are compactly wound with copper wire of rectangular cross-section: $0.8 \times 1.4 \text{ mm}^2$ (Romal). The wire coating is specified for temperatures up to 200 °C. In this section we briefly describe the characteristics of the miniwires and the magnetic-field coils

- *microtrap wires*: A total of six copper miniwires (the layout of these is described in Sec. 3.3.1 and Fig. 3.3) with a resistance of 0.1Ω inside the vacuum provide both magnetic fields of 1 G/A and gradients $5 \text{ G cm}^{-1}\text{A}^{-1}$ at a distance of 2 mm . The six wires are operated at a current of 10 A using three bipolar power supplies (Kepco BOP 20-10) and one unipolar version (Kepco ATE 6-10) all with a bandwidth of around 16 kHz . These very versatile miniwires serve many purposes and are used for example for the MOT field, to generate an IP type magnetic trap and for the atom-focusing experiments. The on-chip Z-wire with $R = 0.7 \Omega$ is operated at $I \leq 2.25 \text{ A}$ using a Kepco ATE 15-3 power supply.
- *compensation coils*: Six coils (1) are added to generate a homogeneous field and a gradient in arbitrary direction, and can be used to compensate the fields from the microtrap wires in any direction. The six compensation coils have 128 windings each. The coils of radius $R = 100 \text{ mm}$ are placed at a distance of $1.8R$ from the center. This is larger than the optimal distance of $R/2$ where the B-field curvature is zero, the so-called Helmholtz configuration. The B-field along the axis in the trap center has a magnitude of 1.84 G/A per coil set and a curvature of $B'' = 0.04 \text{ G/cm}^2$. Each coil has a resistance of 1.5Ω and a self-inductance of 6 mH . The compensation coils are multi purpose. They are used for example to cancel the earth magnetic field, to steer the magnetic field minimum and to add to the bias field in the highly compressed last stage of the BEC production. We run up to 11 A through each coil in a pulsed fashion. Each pair of coils for a specific direction is driven by a single power supply. We use bipolar linear regulated current amplifiers (Kepco BOP 36V, 12A) with a bandwidth of 10 kHz . The switching time for the compensation coils is limited to 2.2 ms by the coil inductance.
- *MOT coils*: A set of gradient coils (3) is used to generate the quadrupole magnetic field for magneto optical trapping. This coil set was constructed together with the vacuum chamber in the Huygens laboratory in Leiden [113]. For an optimal gradient, coils of diameter R should be placed at a distance $R/2$ from the center. In our case the distance is $2R$, a compromise between coil efficiency and available space. The coils fit exactly around a CF40 flange and have an outer diameter of 130 mm . The 624 turns per coil are wound on a hollow water-cooled w-shaped profile. Each coil has a resistance of 1Ω and a self-inductance of 24 mH . Each can carry 10 A of current when cooled with water at a flow rate of 5 ml/s . The resulting field gradient on the axis in the center of the trap is about $2.3 \text{ G cm}^{-1}\text{A}^{-1}$. We drive the current with one switched-mode power supply per coil (Delta SM 35-45). The current is shut-off in 0.5 ms using power MOSFETS (Thomson STE53NA50 500V; 53A).
- *bias coils*: An additional pair of coils (4) strengthens the homogeneous field in the y -direction that forms a waveguide together with the miniwires and chipwires. This is used in the last stage of the BEC production where we apply a magnetic field of 40 G in the y -direction. These bias coils with 100

square windings (130 mm sides) each, have a resistance of 0.7Ω , and a self-inductance of 2 mH, and switch in 1.2 ms. The magnetic field in the center is 1.23 G/A. We use a 20 V, 20 A power supply for each coil (Kepco BOP). The bias coils are water cooled and sustain 20 A if pulsed with a 50% duty cycle.

3.8 Lasers

We use only three simple diode lasers: a grating stabilized *master* laser for cooling and probing at 780 nm, a diode laser locked by injection to the master laser and a *repumper* grating stabilized diode laser at 795 nm. A modular buildup of the laser setup makes it possible to move or reconfigure separate parts. The master and amplifier lasers are placed together on a $75 \times 90 \text{ cm}^2$ breadboard. A schematic drawing is shown in Fig. 3.12. The repumper assembly, not drawn here, fits on a $60 \times 60 \text{ cm}^2$ breadboard and consists simply of a spectroscopy setup, electro-optical and mechanical switches and fiber couplers. All breadboards are placed in black cardboard boxes to prevent scattered light from reaching the main vacuum chamber. On the inside of the boxes egg-box-shaped foam damps acoustic noise. Sheets of sorbothane between the optical table and the breadboards provide for extra mechanical damping.

Master laser

The master laser is a commercial (Toptica DL100) external-grating-feedback diode laser that operates near the ^{87}Rb D2 line (780 nm) and has 90 mW output power. Half of the available light is frequency-shifted and amplified by injection-seeding a second diode laser for cooling and probing. The other half is frequency-shifted and used for optical pumping.

FM lock

The master laser is frequency stabilized on the cross-over (co) line of the $F_g = 2 \rightarrow F_e = 1$ and the $F_g = 2 \rightarrow F_e = 3$ transitions as indicated in Fig. 3.11. This cross-over line is 212 MHz red-detuned with respect to the $F_g = 2 \rightarrow F_e = 3$ cooling transition. We perform saturated absorption spectroscopy in a 10 cm-long 1"-diameter cylindrical room-temperature Rb vapor cell. The spectroscopy beams are 10-times expanded to a diameter of 20 mm and effectively probe the whole cell. To lock our laser we use a frequency-modulation (FM) scheme [123]. We create frequency sidebands on the light signal with an Electro-Optic phase modulator (EOM)[Nova Phase EO-PM-R-020-C1]. The EOM's electrical driving circuit is made resonant with the 20 MHz driving signal obtained from a "Pound Drever Driver" (Toptica PDD110). The low-voltage sine wave (2 V peak-to-peak) yields 4% modulation depth of the laser intensity. Subsequently the spectroscopy signal is recorded on a fast photo diode (PD in Fig. 3.12, Thorlabs DET110) and fed in the Pound Drever Driver where it is phase-shifted and mixed with the 20 MHz oscillator to obtain a dispersive lock signal. The lock signal finally enters a PID controller (Toptica

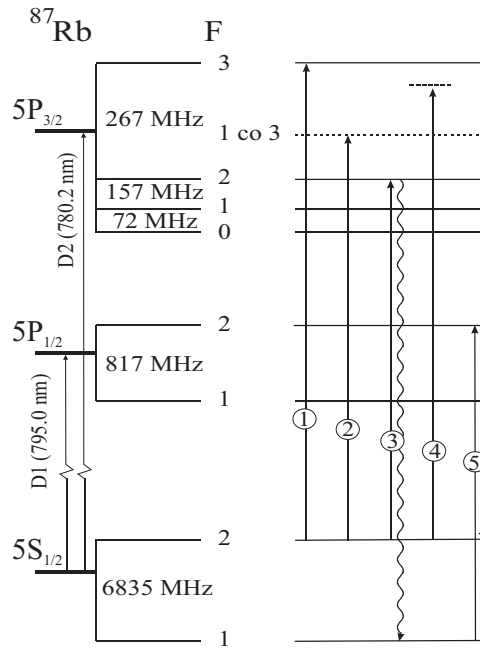


Figure 3.11: Energy level diagram for ^{87}Rb showing the relevant laser frequencies [122]: (1) probe, (2) master laser lock point, (3) optical pump, (4) MOT/molasses cooling, (5) repump.

PID110) that stabilizes the laser frequency on two channels: (*i*) fast feedback is achieved by direct modulation of the laser current; (*ii*) the external cavity grating angle is regulated with a Piezo-electric crystal to compensate for long-term drifts. We have abandoned the cheaper option of generating sidebands by direct modulation of the laser diode current because the sidebands, however small, end up in the light needed for the MOT. The presence of the sidebands appeared to be detrimental in the compressed MOT optical cooling stage probably because the red sidebands give rise to scattering and therefore heating.

Repumper

A second grating-stabilized diode laser (Toptica DL100) is locked to the $F_g = 1 \rightarrow F_e = 2$ transition of the ^{87}Rb D1 line at 795 nm. This “repumper” light serves in the optical cooling process to pump atoms that have fallen in the dark hyperfine ground-state back to the $F_g = 2$ for further cooling. We again use an FM lock. In this case we directly modulate the laser current via a bias-T. This solution is cheaper than the use of an EOM. As mentioned above the disadvantage is that the frequency sidebands end up in the light used for the main experiment. The presence of the sidebands is not critical for the repumping process however.

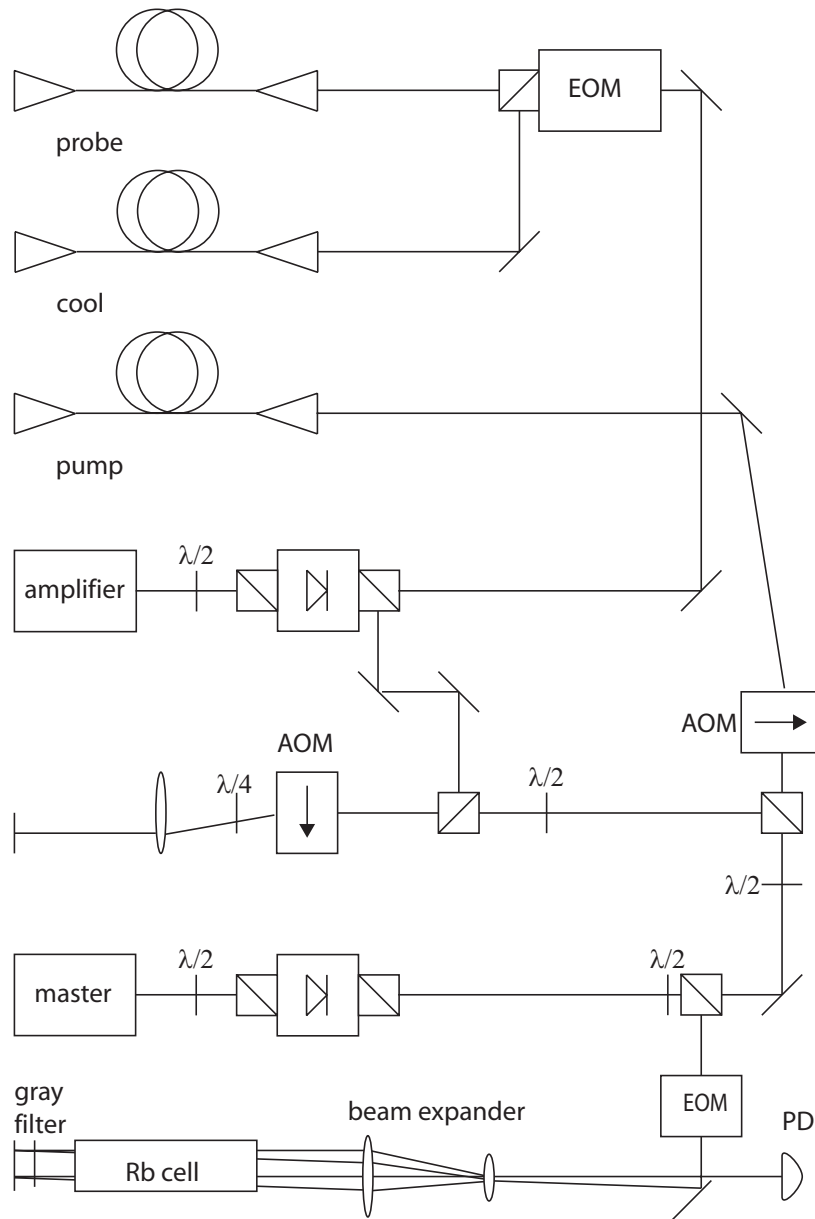


Figure 3.12: Laser setup of the *master* laser with injection lock of a diode laser that acts as an amplifier. See text for a description of the various elements.

Frequency shifter and amplifier

Half of the laser light from the *master* laser is frequency shifted in a double-pass Acousto Optic Modulator (AOM) (Isomet 1205C-02) setup. The frequency of the laser light can thus be tuned between $+1\Gamma$ and -13Γ with respect to the cooling transition where $\Gamma/(2\pi) = 6$ MHz is the natural linewidth. Two mW of frequency-shifted

light is amplified by injection-seeding a 120 mW diode (Sharp GH0781JA2C).⁸ The light is injected by sending it through the output polarizing beamsplitter cube of a 30 dB optical isolator (Linos), see Fig. 3.12. The slave laser is mounted and temperature-stabilized in a convenient commercially available mount (OFR PAL-TE-9.0-780). The free-running diode gives 120 mW of optical power at 784 nm. Operating at $T = 11^\circ\text{C}$ and $I = 139\text{ mA}$ we get about 100 mW of injection-locked light out. We direct the light on two paths, one for probing and the other for cooling. Switching between the two with a bandwidth of 1 MHz is performed with a second EOM (Linos). Both probe and cooling light pass through mechanical shutters (Vincent Associates, Uniblitz, LS2T2) before entering single-mode polarization-maintaining fibers (coupler: Schäfter & Kirchhoff 60 SMS-1-4-A8-07).

Optical pumping

In order to trap the cold atoms magnetically, we pump them to the doubly polarized $F_g = 2; m_F = 2$ state. Optical pumping is performed by simultaneously illuminating the atoms with circularly polarized pump and repump light while the quantization axis is defined by a homogeneous magnetic field along the light axis. The pump light is tuned to the $F_g = 2 \rightarrow F_e = 2$ transition of the D2 line by shifting the master light 55 MHz to the red with an AOM (Isomet 1206C-02). Both pump and repump light beams are transferred to the vacuum chamber through polarization-maintaining fibers. The beams are re-collimated to a $1/e^2$ diameter of 10 mm with beam expanders (Shäfter & Kirchhoff 60FC-4-M60-10). Both beams have about two times the saturation intensity $I_0 = 1.67\text{ mW/cm}^2$. Pump, repump and probe are made circularly polarized with separate $\lambda/4$ -plates before they are overlapped with two non-polarizing beam-splitter cubes (Thorlabs).

MOT

For the MOT operation we couple 38 mW of cooling light and 7.5 mW of repump light from polarization maintaining fibers using beam expanders (Shäfter & Kirchhoff 60FC-T-4-M90-10) resulting in a $1/e^2$ diameter of 15 mm. After the cooling-light output coupler we place a polarizer (Melles Griot 03 PBS 015) to avoid polarization effects originating from temperature-dependent residual birefringence in the fibers. The cooling light is subsequently divided equally over 4 beams with central intensity $5I_0$. Cooling light and repump light are overlapped on a polarizing beam-splitter cube. The repump light has a total intensity of $6I_0$ divided over four beams.

3.9 Imaging system

A polarization-maintaining fiber transports the probe light to the main vacuum chamber. The diverging gaussian beam is collimated to a 10 mm $1/e^2$ diameter

⁸The total cooling power was increased by 25% by replacing the 120 mW diode by a 150 mW type (Roithner RLT780-150GS) in 2007.

with a beam expander (Shäfter & Kirchhoff). The light is made circularly polarized and overlapped with the pump and repump beams on a 50/50 non-polarizing beamsplitter (Thorlabs). The beams enter the vacuum system in the horizontal plane through a CF40 window that is anti reflection coated on both sides. The trap center is imaged with a three times magnifying (Mag=3) relay telescope onto a camera (Roper Scientific Coolsnap ES) see Fig. 3.13. Lens L1 with a diameter $d = 31.5$ mm and a focal length of $f = 100$ mm (Melles Griot 01 LAO 126/076) can be moved with a translation stage to select the object plane (y -direction) and to select the object area (xz -plane). Lens L2 with a diameter $d = 50$ mm and a focal length of $f = 300$ mm has a larger diameter to avoid vignetting.⁹ (Melles Griot 01LAO256/076). All imaging optics including the camera are rigidly mounted to the optical table using 1.5" posts or solid metal blocks. Fixing the translation stage after positioning lens L1 helped in reducing interference fringes in the images. The imaging beam travels through vacuum or is enclosed by lens tubes on most of its path to reduce the disturbing effect of air turbulence.

We probe our polarized atomic samples with circularly polarized light on- or near-resonance with the $F_g = 2 \rightarrow F_e = 3$ cycling transition while defining the quantization axis with a weak (2 G) homogenous magnetic field in the propagation direction of the light (except for *in situ* measurements, where the quantization axis is defined by the IP magnetic field that points perpendicular to the propagation direction of the light). The number of scattered photons when probing with light with intensity I at a detuning δ from resonance for a duration τ can be found from

$$N_{\text{scat}} = \tau \frac{s}{s+1} \frac{\Gamma}{2}, \quad (3.7)$$

$$s = \frac{I/I_0}{1 + 4\delta^2/\Gamma^2}, \quad (3.8)$$

where the saturation parameter s is related to the saturation intensity I_0 . The probe light intensity I is 0.3 mW/cm². With an exposure time τ of 70 μ s we find from equation (3.7) $N_{\text{scat}} = 200$ for the number of scattered photons at resonance. During illumination atoms are displaced by the recoil of the scattered photons. We can estimate the root mean square displacement transverse to the line of sight with $v_{\text{rec}}\tau\sqrt{N_{\text{scat}}/3}$. Inserting the recoil velocity of $v_{\text{rec}} = 5.9$ mm/s we find that 200 recoils give a displacement of 3 μ m. This displacement is smaller than the optical resolution limit of 4 μ m (see below) and of the order of the effective pixel size in the object plane of $6.45/\text{Mag} = 2.15$ μ m (see below).

Imaging camera

We have chosen an interline transfer CCD camera (Roper Scientific Coolsnap ES). It contains a Sony ICX285 CCD chip, data is read out via dark lines between the rows of illuminated pixels. A matrix of micro lenses directs most of the light to the

⁹An aberration occurs if part of the light that enters the optical system is truncated further along its path.

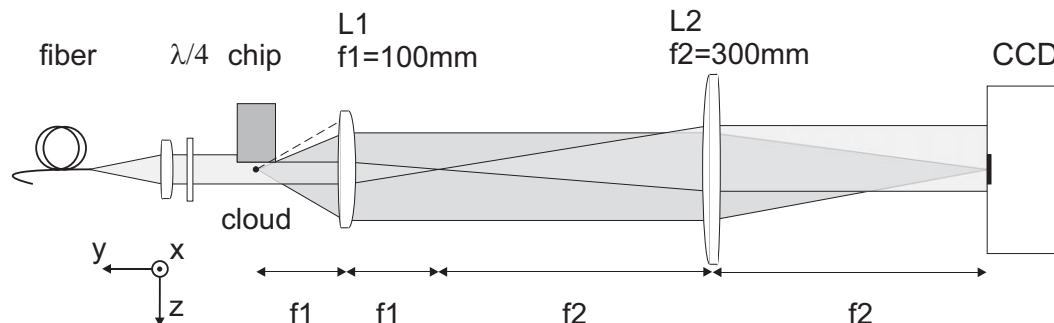


Figure 3.13: Schematic of the imaging setup. A cloud of atoms close to the chip mount is imaged on a CCD camera with a collimated beam from a fiber using a pair of achromatic doublet lenses, the light is circularly polarized after passing through a $\lambda/4$ plate. The lenses form a confocal telescope with magnification $f_2/f_1=3$. Part of the light cone that scatters from the atoms towards the first imaging lens is blocked by the chip mount effectively reducing the numerical aperture of the imaging system (dashed line).

pixels. In this way a quantum efficiency of 30% at 780 nm is obtained. The “interline transfer” technique commonly used in consumer cameras has reached a sensitivity that is not much less than with the frame transfer technique widely applied in cold atom experiments. In the frame transfer CCD’s typically all pixels in the top half of the chip are illuminated, followed by readout that is done by first transferring all charges all the way to the covered lower chip half before the collection of charges in horizontal direction. This transfer scheme slows down the readout rate. The Sony ICX285 CCD chip has $1392 \times 1040 = 1.5 \times 10^6$ pixels with $6.45 \mu\text{m}$ square size. The AD converter generates 12-bit digital data. At the probing light level we saturate about 60% of the full well of 16000 electrons in one pixel, staying nicely in the regime of linear response of the camera. The pixel readout rate is 20 MHz with a RMS readout noise of 8 electrons per pixel. With a dark current of one electron per pixel per second at room temperature cooling is not required for our purpose. The readout time per image is $1.5 \times 10^6 / 20 \times 10^6 \text{s}^{-1} = 75 \text{ms}$. It is possible to read out only pixels within a predefined region of interest (ROI). The readout time is reduced proportional to the fraction of vertical lines in the ROI. We typically use a ROI extending over all 1392 pixels horizontally and only 300 pixels vertically resulting in a readout time of less than 30 ms. Keeping the time between the absorption image and the “flat field” normalizing image short reduces the effect of interference fringes in the resulting images.

Optical resolution

A theoretical resolution limit for imaging with a lens can be given by the Rayleigh criterion: two point sources are resolved if the center of the Airy disc of one overlaps with first dark ring of the other. In formula: $d_{\text{min}} = 1.22\lambda f/d$, where λ is the

wavelength of the light, f is the focal length and d the diameter of the lens [124]. The numerical aperture NA and its inverse, the F-number, are given by $1/F = NA = f/d$. In our setup lens L1 (see Fig. 3.13) has an F-number of 3.17 resulting in a resolution limit $d_{\min} = 3 \mu\text{m}$. We measure a minimal $1/e^2$ radius feature size of $5.6 \mu\text{m}$. This corresponds to a minimal second-order moment of an intensity distribution of $2.8 \mu\text{m}$ and an $1/e$ radius of $4 \mu\text{m}$.

Magnification

To determine the magnification of our imaging system we have used the accurately known dimensions of our chip patterns. We have trapped two clouds of atoms in steep potential wells created with a single chip wire with a separation of $1034 \pm 10 \mu\text{m}$. In an absorption image the cloud separation was 485 ± 4 pixels. Inserting the pixel size of $6.45 \mu\text{m}$ we find a magnification of 3.03 ± 0.04 .

Absorption imaging

The probe beam travelling in the y -direction with initial intensity distribution $I_0(x, z)$ passes an atomic cloud and casts a shadow on the camera. The light is absorbed by the atoms following Lambert-Beer's law

$$I(x, z) = I_0(x, z)e^{-D(x, z)}. \quad (3.9)$$

The optical density profile is the integrated atomic density along the line of sight multiplied by the absorption cross section $D(x, z) = \sigma \int dy n(x, y, z)$ where $\sigma = 3\lambda^2/(2\pi)$ for circularly polarized light and polarized atoms. We find D in Eq. (3.9) from the ratio $I(x, z)/I_0(x, z)$ by taking a sequence of three images. First the absorption image $I_{\text{abs}}(x, z)$ secondly a ‘‘flat field’’ image $I_{\text{ff}}(x, z)$ without atoms and finally a dark background image $I_{\text{bg}}(x, z)$. The background corrected ratio is $I/I_0 = (I_{\text{abs}} - I_{\text{bg}})/(I_{\text{ff}} - I_{\text{bg}})$.

3.10 Experimental control

The experiment is controlled with the help of a single PC in combination with analog and digital cards. Images from the CCD camera are read out and processed directly using the same computer. We give a brief description of the used components and the functionality of the control device here. A more detailed description of the experimental control including the software written in LabView (National Instruments) will appear in [115]. During each experimental cycle of 10 to 20 seconds atoms are trapped and cooled and subsequently a series of digital images is collected. The control involves two tasks: first the programming of digital and analog outputs and second the image processing.

device	type	manufacturer	connections
Industrial PC	IPC-535	Spectra	12 PCI slots
digital card	DIO-64	Viewpoint Systems	64 DO
Analog output 1	PCI-6713	National Instruments	8 AO
Analog output 2	PCI-6713	National Instruments	8 AO
Analog output 3	PCI-6713	National Instruments	8 AO
Analog input	PCI-6014	National Instruments	8 AI
Camera card	PCI	Roper Scientific	Camera control

Table 3.4: Overview of used hardware for experimental control (AI= Analog Input, AO= Analog Output, DI=Digital Input, DO= Digital Output).

3.10.1 Output control

The hardware used in the experimental control is listed in table 3.4. We use an industrial computer (Spectra IPC-535) with 12 available PCI slots in a 19" housing. It runs on Microsoft Windows XP and has a 2.8 GHz pentium 4 processor. The PCI cards involved are: Viewpoint DIO-64 for digital control and timing, three National Instruments PCI-6713 analog output cards and one analog input card (National Instruments PCI-6014). We program 18 bipolar analog outputs (± 10 V) and 31 TTL outputs with sub- μ s time precision in steps of 10μ s. An overview of the control lines involved is listed in table 3.5. Before the start of each cycle a timing sequence of typically 10^4 steps is loaded into the memory of the Viewpoint DIO-64 card. During an experimental cycle the clock on the DIO card governs the timing and triggers the analog output cards guaranteeing reliable timing precision undisturbed by other processes that run on the PC. The TTL signals from the DIO card are shaped with line drivers and connected to a BNC break-out box with twisted pair flat cables to avoid reflections and cross-talk.

3.10.2 Radio frequency source

We generate a radio frequency (RF) signal for forced evaporative cooling with a direct digital synthesis (DDS) evaluation board (Analog Devices). The DDS board is programmed using 8 parallel data lines, 6 address lines and 6 other lines. In this way the RF amplitude and frequency can be controlled with the same 10μ s timing precision as the rest of the control signals. The frequency resolution was set to 24 bits corresponding to 12 Hz. A more detailed description of the DDS system will appear elsewhere [115].

Image processing

Three images of maximally $1.5 \cdot 10^6$ pixels are collected in ≈ 75 ms per image. Subsequently the two dimensional optical density is calculated and displayed in real time. Two simple gaussian fits are performed separately to estimate atom number and cloud size "on the fly". The set of three images is stored in the lossless 16 bits pgm format for further analysis.

analog	digital
cool/probe EOM	camera trigger
cool/probe AOM	probe shutter
pump AOM	cool shutter
repump EOM	repump 1 shutter
dispenser	repump 2 shutter
miniwire 1	pump shutter
miniwire 2	MOT coils on/off
miniwire 3	RF on/off
miniwires 4, 5 and 6	DDS 1-8 data
compensation coils 1	DDS 1-6 address
compensation coils 2	DDS 1-6 other
compensation coils 3	AO trigger 1
MOT coil 1	AO trigger 2
MOT coil 2	AO trigger 3
Y bias coils	
chipwire Z	
chipwire box	
RF amplitude	

Table 3.5: Overview of used analog and digital control lines.

3.11 Concluding remarks

The described setup forms a state of the art machine for cold atom experiments that is especially suited for studying the 1D regime. In the design emphasis was put on simplicity and compactness, resulting in a reliable and stable setup for BEC production. The design and thermal analysis of the novel microtrap are discussed in some detail forming a basis for improvements and more general applications. The next chapter describes how this setup is used. One elementary cycle that leads to the production of a BEC every 10 seconds is detailed.

4 Realizing Bose-Einstein condensation

4.1 Introduction

This chapter describes one trapping and cooling cycle that is used to reach Bose-Einstein condensation (BEC) in the microtrap that was described in Ch. 3. The first part (Sec. 4.2) describes the magneto-optical cooling steps and a rapid evaporative cooling stage that we apply to reach an elongated three-dimensional BEC. Section 4.2.7 describes the specific scheme that was used to reach the cross-over to the 1D quasi-condensate regime. In Sec. 4.3, we characterize the roughness of the trapping potential for our quasi-condensates. This roughness stems from non-straight current flow in the trapping wire. We discuss how we have reduced the influence of this roughness and we give an estimate for the smoothness of the resulting potential.

4.2 Trapping and cooling sequence

Our goal in the trapping and cooling sequence is to reach quantum degeneracy with the highest atom number possible. A spherical gaussian cloud of radius r containing N atoms has a central density $n_0 = N\pi^{-3/2}r^{-3}$. The phase space density in the trap center is $\Phi = n_0\Lambda_T^3$, with Λ_T the thermal de Broglie wavelength, Eq. (2.14). Bose-Einstein condensation in a three-dimensional ideal Bose gas is reached for $\Phi > 2.612$ (see Ch.2). The successive steps, discussed here, that increase the phase space density of a cloud of atoms and finally lead to Bose condensation are generally applied in BEC labs worldwide. Specific for our experimental setup is the use of miniwires to generate the magnetic potentials for the cooling and trapping stages. In short, the procedure is as follows. In the first step we load our mirror-MOT [111] secondly we apply a short compressed MOT [125] stage. Subsequently the atoms are optically pumped to a single magnetic Zeeman state followed by magnetic trapping in the miniwire trap. A transfer to the magnetic potential of the on-chip Z-wire enables us to compress the trapping volume thereby increasing the inter-atomic collision rate. Finally, we perform forced evaporative cooling using radio frequency induced spin flips. A single 1.2 s RF ramp leads to the fast and relatively efficient production of a Bose-Einstein condensate of $\sim 10^4$ atoms. These steps are described below in more detail.

4.2.1 MOT

We start the trapping and cooling sequence by resistively heating the dispenser described in Sec. 3.6. The hot ($T > 600$ °C) rubidium atoms that escape from the dispenser thermalize by collisions with the walls of the vacuum chamber. At room temperature and a ^{87}Rb pressure of 10^{-9} mbar we have $\Phi = 10^{-25}$. The largest gain in phase space density is reached in the first cooling step with the magneto-optical trap (MOT): We trap $5 \cdot 10^7$ atoms and reach $\Phi = 10^{-9}$. Specifically, we use the mirror MOT [111] configuration (see Sec. 3.3), where four cooling laser beams with 15 mm $1/e^2$ diameter and 9 mW of power per beam impinge on the central trapping area (see Fig. 3.2). The two beams in the yz -plane reflect at a 45° angle on the surface of our micro-electronic chip. This scheme creates the three orthogonal beam pairs needed for a 3D MOT while the center of the MOT is only millimeters away from the chip surface. The cooling light is detuned 2.7Γ to the red with respect to the $F = 2 \rightarrow F = 3$ cycling transition of the D2-line and the central intensity is $6I_0$, where the saturation intensity is $I_0 = 1.67$ mW/cm 2 and $\Gamma/2\pi = 6$ MHz is the natural linewidth of the atomic transition. We overlap a repumper light beam with the same diameter with all four cooling beams. The repumper is resonant with the $F = 1 \rightarrow F = 2$ transition of the D1-line, and the central intensity is at saturation (1.49 mW/cm 2). The quadrupole magnetic field in this initial stage is generated with the MOT coils (Sec. 3.7) that produce a gradient of 15 G/cm. The dispenser, see Sec. 3.6, is pulsed on by resistive heating during a 4 s 12 A current pulse. After switching off the current, the dispenser cools down within 4 s. The vacuum pressure recovers for 6 s after the end of the dispenser pulse before we prepare for the second cooling step by transferring the atoms to a miniwire-based MOT. A schematic overview of the cooling and trapping sequence described here is shown in Table 4.1. We ramp down the current in the MOT coils while ramping on current in the miniwires in combination with a homogeneous bias field of 5 G in the $+y$ direction. A -4 G bias field component in the z direction is added to match the ideal quadrupole field optimally [126]. The miniwires and their dimensions are shown in Fig. 3.3. In the positive x direction miniwires 4, 5, and 6 carry a current of 2 A each, while miniwires 1 and 3 are operated at $+3.5$ A and -3.5 A along y respectively. The transfer takes 80 ms and the resulting miniwire quadrupole field compresses the MOT magnetic field to a gradient of 30 G/cm at a distance of 1.2 mm from the chip.

4.2.2 Compressed MOT

The next important increase in phase space density is achieved with the compressed MOT technique [125]. In this 6 ms cooling stage we reduce the light pressure, that arises from the scattered cooling photons, by decreasing the repumper intensity by two orders of magnitude while we increase at the same time the detuning of the cool light from 2.7Γ to 13Γ . Consequently a larger fraction of the the MOT atoms will end up in the dark $F = 1$ ground state, hence the alternative nomenclature for this trick: “transient dark MOT”. The compressed MOT stage results in a

	MOT loading	Vacuum recover	compress+move up	wire MOT	compressed MOT	optical pumping	mini wire IP trap	Z-wire trap	compress Z	evaporative cooling
Dispenser										
MOT coil 1										
MOT coil 2										
bias coil B _y										
mini-wires 4,5,6										
mini-wires 1,3										
miniwire 2										
chip Z-wire										
RF										
cool light										
Repumper										
Pump										
detuning/(2 π 6MHz)	2.7	2.7	5.5	2.7	13	0				
duration [ms]	4000	6000	80	105	6	0.4	10	38	400	1200
atom number [10 ⁶]	50	50	50	40	40	40	20	20	20	0.04
temperature [μ K]	100	100	100	100	100	30	40	40	500	1.3

Table 4.1: Timeline for the trapping and cooling sequence. In the first step we load our mirror-MOT, secondly we apply a short compressed MOT stage. Subsequently the atoms are optically pumped to a single magnetic Zeeman state followed by magnetic trapping in the miniwire trap. A transfer to the magnetic potential of the on-chip Z-wire enables us to compress the trapping volume thereby increasing the inter-atomic collision rate. Finally, we perform forced evaporative cooling using radio frequency induced spin flips. A single 1.2 s RF ramp leads to the fast and relatively efficient production of a Bose-Einstein condensate.

dense cold cloud with a lower atom number but a much higher phase space density ($N = 4 \cdot 10^7$; $T = 30 \mu\text{K}$; $n_0 = 5 \cdot 10^{16} \text{ m}^{-3}$; $\Phi = 2 \cdot 10^{-6}$) compared to the standard MOT.

4.2.3 Optical pumping

An optical pumping stage transfers the atoms to the magnetically trappable $F = 2, m_F = 2$ Zeeman state. First the MOT light and quadrupole field are switched off. A small bias field, $B_y = 2 \text{ G}$ defines a quantization axis for the atoms. Two co-linear circularly polarized beams also point in the y direction: a resonant repump beam (D1; $F = 1 \rightarrow F = 2$) and the pump beam, tuned to the $F = 2 \rightarrow F = 2$ transition of the D2-line. An optical pumping pulse of $400 \mu\text{s}$ at an intensity $\sim 3 \text{ mW/cm}^2$ per beam transfers nearly all atoms to the doubly polarized state.

4.2.4 Minitrap

The spin-polarized atoms can now be captured in the Ioffe-Pritchard magnetic trap. To exactly mode match the optically cooled cloud ($T = 30 \mu\text{K}$) with a radius ($r \approx 0.5 \text{ mm}$) to the trapping potential we need trap frequencies $\omega = \sqrt{2k_B T / mr^2} =$

$2\pi \times 23$ Hz. These low frequencies can only be reached in a chip trap that is very shallow due to gravitational sag. Our best results ($N = 2 \cdot 10^7$; $\Phi = 1 \cdot 10^{-6}$) were achieved by lifting the trap bottom B_0 to 8 G resulting in a trap with an axial frequency of 16 Hz and a radial frequency of 46 Hz. Miniwire current settings are: 6.65 A, for wires 4,5 and 6; 9.8 A, for wires 1 and 3, and -2.5 A through miniwire 2. The cartesian field vector from the external bias coils is $(B_x, B_y, B_z) = (8, 17, 0)$ G.

4.2.5 Z-trap – compression

After having loaded the miniwire trap we start a magnetic field ramp that adiabatically transfers the atoms to a potential made with the on chip Z-wire. The Z-wire current is ramped to 2.25 A in 28 ms while the miniwires are turned off. In order to increase the axial harmonic confinement frequency we leave on miniwire 2 (see Fig. 3.3) with -2 A of current. We adiabatically compress the cloud in two steps. We ramp down B_0 (in the x direction) from 8 G to 2.2 G in 400 ms while in the last 200 ms we also increase B_y from 17 G to 40 G. After this transformation the trap frequencies are $\omega_{\parallel} = 2\pi \times 35$ Hz in the axial and $\omega_{\perp} = 2\pi \times 3.3$ kHz in the radial direction.

4.2.6 Reaching BEC by evaporative cooling

The final increase in phase space density of six orders of magnitude that ultimately leads to degeneracy is achieved by evaporative cooling [98,99]. In Sec. 2.8 a treatment of the evaporative cooling process along the lines of [99] is given for the specific case of our IP trap, in the regime where the confining potential is radially linear and axially harmonic. We selectively remove the high-energy tail of the Maxwell-Boltzmann velocity distribution of the trapped atoms using radio-frequency (RF) induced spin flips. Hot atoms are resonantly excited with a RF signal from a DDS (Sec. 3.10.2) that is connected to a chip wire neighboring the Z-trap wire. For our starting condition ($N = 2 \cdot 10^7$; $\Phi = 1 \cdot 10^{-6}$; $T \approx 45$ μ K) the elastic collision rate, Eq. (2.56), $1/\tau_{\text{el}} = 4$ s $^{-1}$. By adiabatic compression of the IP-trap at constant atom number we reduce the trap volume with a factor $\beta \approx 140$, thereby boosting the scatter rate by that same factor ($1/\tau_{\text{el}} \propto \beta$). In this case the temperature scales as $T \propto \sqrt{\beta}$, and goes up to ≈ 0.6 mK. As our trap, with depth $\epsilon = 38$ G (2.5 mK), is not quite deep enough to maintain $\eta > 7$ needed for a $\gamma_e > 2$ (see Fig. 2.5), we apply an evaporation knife at a constant height of 38.5 G ($\omega_{\text{RF}}/2\pi = 27$ MHz, $\epsilon = 36.3$ G) during the adiabatic compression ramp, to guarantee homogeneous evaporation at all times.

After compression we start a logarithmic frequency sweep from 27 MHz to a final value of ~ 1.55 MHz with a duration of 1.2 s. Condensation is reached at an atom number of $7 \cdot 10^4$ and a temperature of 1.3(1) μ K. The central density at condensation is $3 \cdot 10^{20}$ m $^{-3}$ leading to a scatter rate of $3 \cdot 10^3$ s $^{-1}$. The overall efficiency is $\gamma_{e,\text{tot}} = 2.6$. In Fig. 4.1 (left) we show absorption images taken on the day that the first condensates were produced in our setup in the spring of 2006. Pictures are taken after 11 ms of free expansion and correspond to lowering the RF

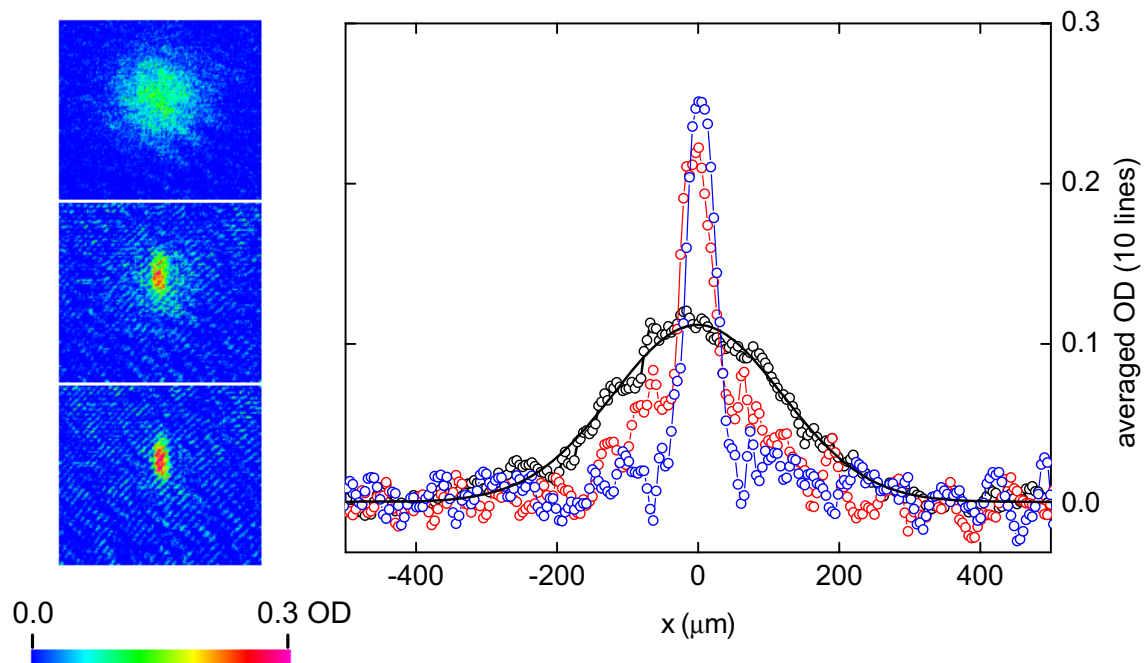


Figure 4.1: (left) Absorption images of ultracold atom clouds, taken after 11 ms of free expansion, correspond to lowering the RF evaporation knife from 1.63 MHz (top) to 1.59 MHz (middle) and finally 1.57 MHz (bottom). (right) horizontal cut through the displayed absorption images. A clear transformation from the gaussian thermal distribution above T_c (\circ) to a bimodal distribution (\circ), and finally the Thomas-Fermi shape of an almost pure condensate (\circ). The black line corresponds to a gaussian fit to the data at 1.63 MHz, the temperature resulting from this fit is $1.4(1) \mu\text{K}$.

evaporation knife from 1.63 MHz (top) to 1.59 MHz (middle) and finally 1.57 MHz (bottom). The panel at the right in Fig. 4.1 shows a horizontal cut through the displayed absorption images. A clear transformation is visible from the gaussian thermal distribution above T_c (\circ) to a bimodal distribution (\circ), and finally the Thomas-Fermi shape of an almost pure condensate (\circ).

4.2.7 Axial relaxation – reaching BEC in the 3D-1D cross-over

For the experiments on the Bose gas in the dimensional cross-over regime from 3D to 1D that are described in Ch. 5 and Ch. 6 we have used the following adapted procedure. After the first 400 ms of compression of the Z-wire trap we start a linear evaporation ramp of 600 ms from 27 MHz to 1.7 MHz. Before reaching degeneracy we relax the axial confinement to a final trap with $\omega_{\parallel}/2\pi = 8.5$ Hz along x , and $\omega_{\perp}/2\pi = 3280$ Hz, and a bottom corresponding to $\omega_{RF}/2\pi = 1.518(2)$ MHz; for comparison $\hbar\omega_{\perp}/k_B = 158$ nK. The current in the Z-wire is set at 2.25 A, and the distance of the cloud to the chip surface is $90 \mu\text{m}$. In this final trap a slower forced

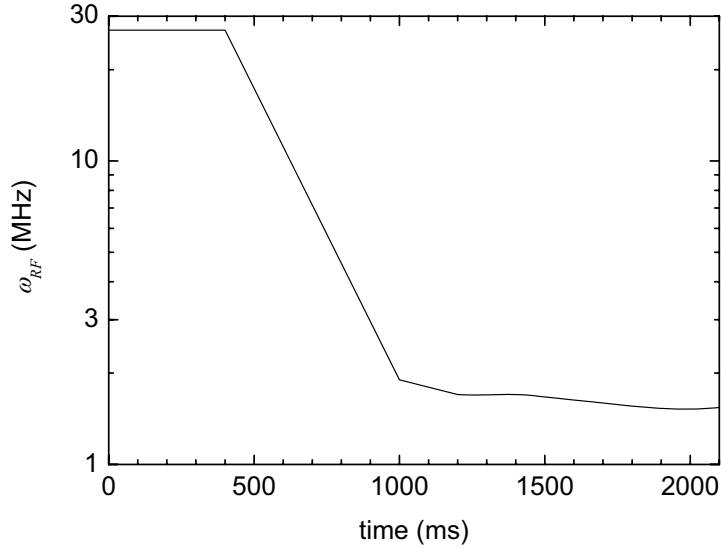


Figure 4.2: RF frequency ramp that was employed for the achievement of an elongated condensate. We start by applying 400 ms of plain evaporation during the compression of the magnetic trap. Followed by a rapid cooling ramp (600 ms) before we carefully relax the trap axially and cool to degeneracy slowly in order to create an elongated condensate that is in equilibrium at the end of the last 300 ms of plain evaporation.

evaporation stage is performed, where we ramp the RF frequency from 1.7 MHz to ~ 1.55 MHz in 450 ms. An additional 300 ms of plain evaporation at the final RF frequency allows the damping of residual quadrupole collective oscillations in the cloud to the point where these oscillations are no longer visible within our experimental resolution. We slow down the evaporation process before reaching BEC to avoid shock cooling: if the cooling goes faster than the axial thermalization, local patches of BEC are formed along the axis. These patches subsequently collapse into the central potential resulting in large quadrupole oscillations [127]. We reach degeneracy at an atom number of $4 \cdot 10^4$, thus the overall efficiency is $\gamma_{e,tot} = 2.2$. The RF ramp is shown in Fig.4.2. To penetrate further into the 1D regime we can purposely reduce the atom number by performing the first RF ramp from 27 MHz to 1.7 MHz much faster, for example not in 600 ms but in 160 ms. In the latter case the linear density of a quasi-condensate is $50 \mu\text{m}^{-1}$, well below the cross-over value of $150 \mu\text{m}^{-1}$ (see 2.4.3).

4.3 Potential roughness

Our typical trapping distance $d = 90 \mu\text{m}$ is of the same order as the typical axial size of a cold cloud. At this relatively large distance the effect of potential corrugations due to wire roughness at large spatial frequencies ($\gg 1/d$) is strongly suppressed [128, 129]. Only residual, long-wavelength ($\lambda \sim d$) deviations from straight

current flow in the trapping wire are visible as small (< 1 mG) potential perturbations. The relative potential roughness is $\Delta B/B \sim 10^{-5}$. This roughness corresponds to a few tens of nanokelvins in energy and thus disturbs our condensates that have a chemical potential of ~ 160 nK. In order to minimize the effect of the residual wire corrugations we look for a “sweet spot” along the trap axis. We displace the trap center in the x direction by sending additional currents through miniwires 1 ($-y$) and 3 ($+y$). The resulting magnetic field gradient gives an approximately linear displacement of $400 \mu\text{m}/\text{A}$. In Fig. 4.3 a scan along the x -axis is shown, subsequent traces are shown displaced in the vertical direction to increase the visibility. Linear density traces are taken for increasing miniwire current in steps of 50 mA, corresponding to approximately $20 \mu\text{m}$ axial displacement per step. The red curve is taken in a region where the potential is smoothest: our sweet spot.

After the identification of the sweet spot we have characterized the axial trapping potential with standard methods using both the measurement of *in situ* density profiles at high T [129] and the dipole mode oscillation frequency in the trap center. The relative potential roughness at $d = 90 \mu\text{m}$ is $\Delta B/B \sim 10^{-5}$ and can be compared to the value of $\Delta B/B \sim 10^{-5}$ quoted by Krüger *et al.*, be it much closer to the chip ($d = 10 \mu\text{m}$) [130]. Our potential is much smoother than the original trap wire used by the Orsay group that was nicely characterized in Ref. [129].

Note that we have followed here a pragmatic approach to circumvent the effect of wire corrugations. For the present work, a full analysis of the cause of the irregular cloud shapes in Fig. 4.3 was not performed. Another way to suppress potential roughness was presented in Ref. [131]. There, a new method for strong suppression of the corrugation (employing ac modulation) was demonstrated. Evidence for strong suppression of the corrugation was obtained from the increase of the damping time of the center-of-mass motion, while the optical images still showed some residual apparent roughness in the 10-nK range. This apparent roughness was attributed to residual noise in the imaging system.

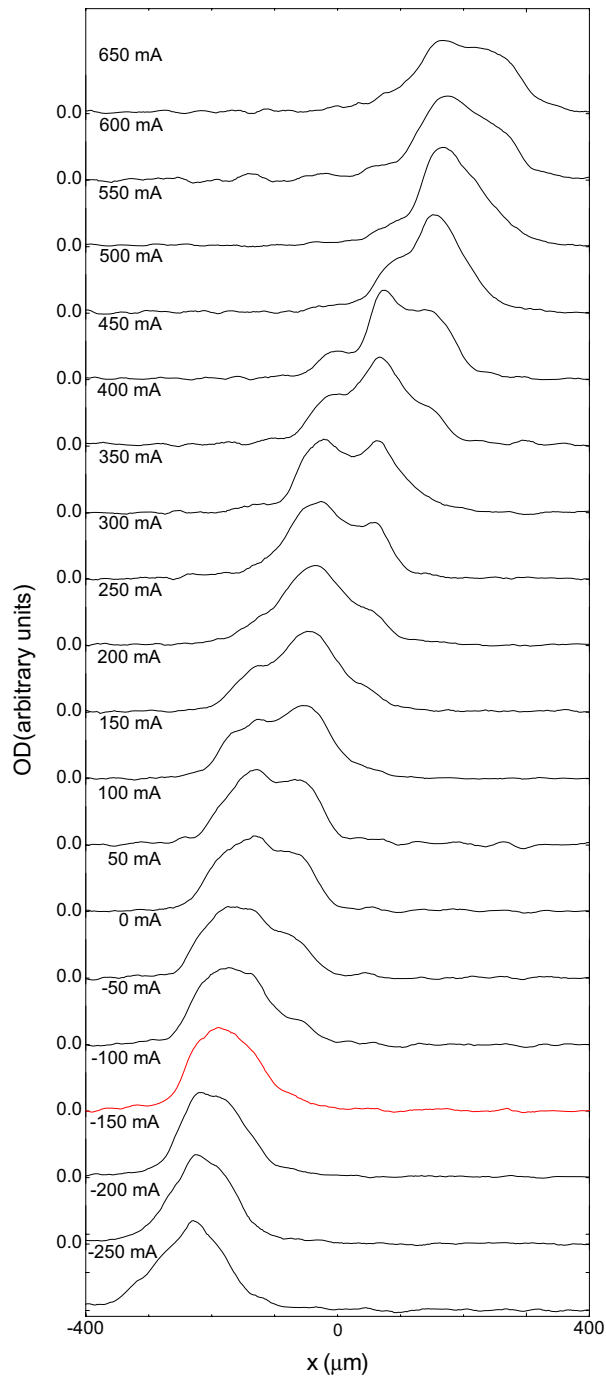


Figure 4.3: Linear density traces of condensates imaged *in situ* for varying axial trap center position. Traces are taken for increasing miniwire 1 and 3 current with steps of 50 mA, corresponding to approximately $20 \mu\text{m}$ axial displacement. In the graph subsequent traces are displaced vertically to increase the visibility. The red curve indicates our “sweet spot”, the region where the potential is smoothest.

5 Focusing phase-fluctuating condensates

5.1 Introduction

The term ‘atom optics’ stems from the possibility to translate techniques and theory from optics to the field of atomic physics. Work with atomic and molecular beams dates back to the first half of the twentieth century [132]. Paul and Friedberg [133, 134] first implemented optical imaging with neutral atoms in 1950. Early examples of the exchange of roles of light and matter are the idea by Balykin and Letokhov to focus an atomic beam using an optical potential [135] and their experimental demonstration of the reflection of atoms on an evanescent light wave mirror [136]. Such a light mirror was later used in Amsterdam with the aim of creating a BEC with all optical means [137, 138]. With the achievement of BECs as a source of coherent atomic waves, the step to the experimental demonstration of an atom laser was small [139–142]. Immanuel Bloch and coworkers demonstrated a variety of atom-optical manipulations: reflection, focusing, and the storage of an atom laser beam in a resonator [143]. In the last decade, the group of Alain Aspect made detailed progress in the study of atom lasers [144–148]. A theoretical treatment of the propagation of atom-laser beams was given by Bordé [149, 150]. Coherent atomic waves are a promising tool, analogous to lasers, but with the possibility of a much smaller wavelength and therefore higher spatial resolution. A further application is the use of atomic waves in a Sagnac interferometer that can lead to huge sensitivity improvements over ring laser gyroscopes. The Sagnac phase shift of a particle traversing an interferometer is proportional to the mass energy of the interfering particle, this is 10^{10} times larger for an atom than for a photon [151]. Dave Pritchard and his group performed pioneering experiments using an atomic beam for interferometry [152] in the early 1990s.

Another optical technique applied to atoms was demonstrated in Amsterdam, where a non-equilibrium BEC was focused in free flight [127]. We have extended this atom-focusing technique, also building on the work in Ref. [153], to equilibrium clouds, that are in the cross-over from the three-dimensional to the one-dimensional regime. We have used the technique to study the axial momentum distribution of these gases. In this chapter we present data showing the focusing of clouds in the quasi-condensate regime. We are able to extract the temperature from the focal width of quasi-condensates. In this way we have implemented a novel tool

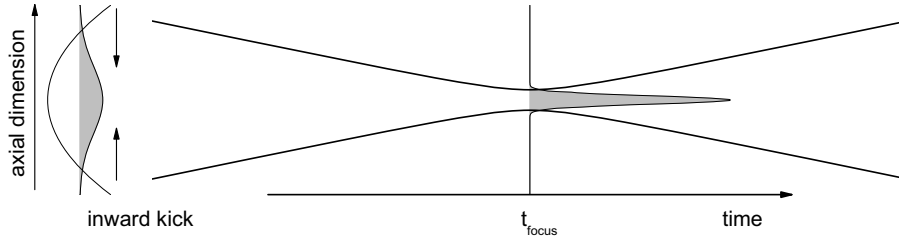


Figure 5.1: Principle of focusing an atomic cloud. We apply a short, strong axial harmonic potential yielding a kick to the atoms proportional to their distance from the trap center, followed by free propagation. As a result the atoms come to a focus, at which time (t_{focus}) the axial density distribution reflects the axial momentum distribution before focusing.

for cold atom thermometry. We derive the relation between the focal width and the temperature by explicitly exploiting the wave nature of atoms: An elongated (quasi-)condensate as it propagates freely after its release from the trap is described as a macroscopic wavefunction. It obeys the Schrödinger equation that has the same form as the paraxial wave equation for light.

We have also obtained focusing results for cold clouds in a regime where atomic interactions and non-zero temperature lead to reduced coherence, and a quasi-condensate description is not always applicable. Those results are described in Ch. 6.

The concept of focusing an elongated cloud is as follows: We apply a short, strong axial harmonic potential yielding a kick to the atoms proportional to their distance from the trap center (analogous to the action of a lens in optics), followed by free propagation. As a result the atoms come to a focus, at which time (t_{focus}) the axial density distribution reflects the axial momentum distribution before focusing. The focusing concept is illustrated in Fig. 5.1. Since the focusing brings all atoms together axially, the signal level is high, even for a single realization. As we will show, averaging over a few shots is sufficient to obtain high signal-to-noise ratio.

The outline of this chapter is as follows. We start in Sec. 5.2 by giving a brief summary of concepts known from optics like the ABCD matrix, the Huygens-Fresnel integral and gaussian beam propagation. We proceed in Sec. 5.3 by exploiting the equivalence of the paraxial wave equation and the Schrödinger equation in 1D to outline the theory for matter wave propagation through linear ABCD systems. We extend the existing work on nonideal light beams [154, 155] and matter wave propagation [146, 148–150] by making a connection between the quality factor M^2 of a nonideal atomic beam and the temperature of a quasi-condensate. This treatment enables us to derive the relation between the focal width of quasi-condensates and the temperature, given in Sec. 5.4. In Sec. 5.5 we summarize the behavior of a weakly interacting quasi-condensate in a time-dependent trap with scaling equations [156–158]. The experimental methods and results of the novel quasi-condensate thermometry method are presented in Sec. 5.6. In Sec. 5.7 we discuss the experimental limits of the presented method. We conclude this chapter and give an outlook in Sec. 5.8.

5.2 Gaussian and nonideal optical beams and ABCD matrices

As an introduction to *atom optics* some basics of gaussian beam optics and ABCD matrices are briefly summarized following Ref. [124]. Additionally, we discuss the treatment of nonideal light beams, using the quality factor M^2 that was developed by Siegman [159] and Bélanger [160] in the early 1990s.

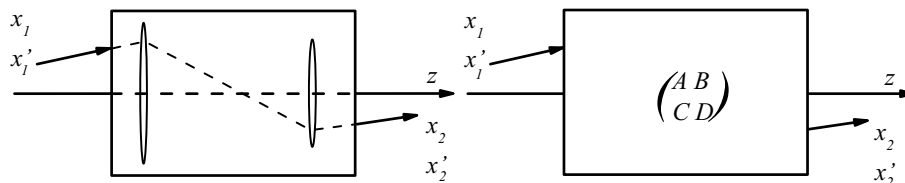


Figure 5.2: Overall ABCD matrix for the propagation of an optical ray through a cascade of optical elements.

In textbook optics [161, 162] an ABCD matrix describes the transformation of the vector of position x and slope x' of a light ray as it propagates from a plane z_1 to a plane z_2 through a cascade of optical elements as is shown in Fig. 5.2. In matrix form

$$\begin{pmatrix} x_2 \\ x_2' \end{pmatrix} = \begin{pmatrix} A & B \\ C & D \end{pmatrix} \begin{pmatrix} x_1 \\ x_1' \end{pmatrix}. \quad (5.1)$$

The ABCD matrix has unit determinant

$$AD - BC = 1. \quad (5.2)$$

For a complete system, with many elements, the overall ABCD ray matrix is simply computed by multiplication of matrices of the individual optical elements and regions of free space that a light ray passes.

5.2.1 Paraxial wave equation and Huygens-Fresnel integral

We consider a monochromatic light wave that propagates mainly along the optical axis and has a slowly varying envelope. We write the general complex wave like

$$\tilde{E}(x, y, z) \equiv \tilde{u}(x, y, z)e^{ikz}, \quad (5.3)$$

where $k = 2\pi/\lambda$ is the wavevector of the light.¹ The propagation of this beam is governed by the electromagnetic wave equation that follows from Maxwell's equations and the appropriate boundary conditions. In the wave equation the second partial derivative in z may be dropped if

$$\left| \frac{\partial^2 \tilde{u}}{\partial z^2} \right| \ll \min \left\{ \left| 2k \frac{\partial \tilde{u}}{\partial z} \right|, \left| \frac{\partial^2 \tilde{u}}{\partial x^2} \right|, \left| \frac{\partial^2 \tilde{u}}{\partial y^2} \right| \right\}. \quad (5.4)$$

¹We use the imaginary number i instead of $-j$ used by Siegman.

The propagation of $\tilde{u}(x, y, z)$ in free space can then be described with the *paraxial wave equation* in the form

$$\left[\nabla_{\mathbf{r}}^2 + 2ik \frac{\partial}{\partial z} \right] \tilde{u}(\mathbf{r}, z) = 0, \quad (5.5)$$

where $\mathbf{r} \equiv (x, y)$ are the transverse coordinates and $\nabla_{\mathbf{r}}$ is the laplacian operator working on these transverse directions. The paraxial wave approximation is valid if the inequality (5.4) is satisfied. This is typically applicable for waves that propagate at an angle of less than 30° with the optical axis [124].

The propagation of paraxial beams can be calculated alternatively using Huygens' integral. A wave (writing only one transverse dimension for brevity) $\tilde{u}(x)$ is transported from the plane z_1 to the plane z_2 by

$$\tilde{u}(x_2) = \int_{-\infty}^{\infty} \mathcal{K}(x_2, x_1) \tilde{u}(x_1) dx_1, \quad (5.6)$$

where $\mathcal{K}(x_2, x_1)$ is the Huygens kernel. If the criterium (5.4) is met, it can be written in the Fresnel approximation

$$\mathcal{K}(x_2, x_1) = \frac{1}{\sqrt{2i\pi B}} \exp \left[\frac{i}{2B} (Ax_1^2 - 2x_2x_1 + Dx_2^2) \right], \quad (5.7)$$

where, for a given optical system A, B and D are the same constants that appear in the ABCD matrix of that system derived using geometric optics, Eq. (5.1) and Eq. (5.2). By inserting Eq. (5.7) in Eq. (5.6) we get the Huygens-Fresnel integral

$$\tilde{u}(x_2) = \int_{-\infty}^{\infty} \frac{1}{\sqrt{2i\pi B}} \exp \left[\frac{i}{2B} (Ax_1^2 - 2x_2x_1 + Dx_2^2) \right] \tilde{u}(x_1) dx_1. \quad (5.8)$$

A set of solutions to both the paraxial wave equation and the Huygens-Fresnel integral is formed by the gaussian beams of the form

$$\tilde{u}(x, z) = \tilde{q} \exp \left[ik \frac{x^2}{2R(z)} - \frac{x^2}{w^2(z)} \right], \quad (5.9)$$

we have used the complex radius of curvature, defined as

$$\frac{1}{\tilde{q}} \equiv \frac{1}{R(z)} + i \frac{\lambda}{\pi w^2(z)}, \quad (5.10)$$

where $R(z)$ is the radius of curvature and $w(z)$ is the $1/e^2$ intensity half width. The variation of the complex radius of curvature along z is

$$\tilde{q}(z) = \tilde{q}_0 + z - z_0, \quad (5.11)$$

with the complex source point $\tilde{q}_0 = \tilde{q}(z_0)$. This leads to

$$w^2(z) = w_0^2 \left[1 + \frac{(z - z_0)^2}{z_R^2} \right], \quad (5.12)$$

with w_0 the minimum transverse size, and

$$R(z) = z + \frac{z_R^2}{z}. \quad (5.13)$$

Where the Rayleigh range

$$z_R \equiv \frac{\pi w_0^2}{\lambda}, \quad (5.14)$$

is the distance the beam travels from the waist w_0 until the diameter increases by a factor $\sqrt{2}$. It is shown for example in [124] using the Huygens-Fresnel integral [Eq. (5.8)] that for a general system characterized by an ABCD matrix the complex beam parameter \tilde{q} transforms according to the relation

$$\tilde{q}_2 = \frac{A\tilde{q}_1 + B}{C\tilde{q}_1 + D}. \quad (5.15)$$

Thus a gaussian beam can be propagated through cascaded optical elements using the cascaded ABCD matrix for those elements.

5.2.2 Nonideal beam

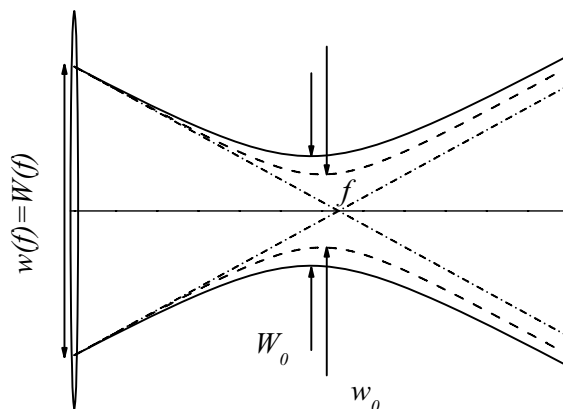


Figure 5.3: Focusing of a Gaussian light beam (dashed line) and a nonideal light beam (solid line) with the same size at the lens position but $M^2 = 1.5$; the dash dotted line intersects the axis at the geometrical focus f of the lens.

To treat monochromatic beams in the paraxial approximation that are *not* diffraction limited and have ripples in phase and amplitude at any transverse plane, Siegman [159] and Bélanger [160] have introduced a treatment analogous to that for gaussian beams. Consider a beam size $W(z)^2 \equiv [2\Delta x(z)]^2$, where Δx^2 is the second-order moment [Eq. (5.30)] of the transverse intensity profile of the general beam. The complex radius of curvature can be generalized for arbitrary beams [159]

$$\frac{1}{Q} = \frac{1}{R} + i\frac{\lambda M^2}{\pi W^2}, \quad (5.16)$$

where R approximates the mean radius of curvature and M^2 is the so-called beam quality factor that is an invariant coefficient of the beam. Just like for gaussian beams, it follows from the Huygens-Fresnel integral [Eq. (5.8)] that the generalized radius of curvature for an arbitrary beam obeys the relation [160]

$$Q_2 = \frac{AQ_1 + B}{CQ_1 + D}. \quad (5.17)$$

This formalism now allows the propagation of arbitrary paraxial beams through ABCD systems. As a simple example we write the propagation rule for the beam size of an arbitrary beam as it propagates through free space starting from its waist at z_0 where the beam attains its minimum size W_0

$$W^2(z) = W_0^2 \left[1 + M^4 \left(\frac{\lambda}{\pi W_0^2} \right)^2 (z - z_0)^2 \right]. \quad (5.18)$$

A comparison of an ideal gaussian beam and a distorted beam with $M^2 = 1.5$ is plotted in Fig. 5.3.

5.3 Atom optics and ABCD matrices

In this section the step from *light optics* to *atom optics* is made. In Sec. 5.3.1 the equivalence of the paraxial wave equation and Schrödinger's equation for matter waves is discussed. Further, via the Huygens-Fresnel integral applied to matter waves we arrive in Sec. 5.3.2 at a formulation of the ABCD matrices for atoms. In Sec. 5.3.3 we relate the temperature of a non-interacting gas to its focal width.

5.3.1 Schrödinger equation and Wigner function

The application of techniques from optics to matter waves can be established by exploiting the analogy between the paraxial wave equation for light Eq. (5.5) and the Schrödinger equation for matter waves:

$$\left[\frac{\hbar^2}{2m} \nabla_x^2 + i\hbar \frac{\partial}{\partial t} + V_{\text{ext}}(x) \right] \psi(x, t) = 0. \quad (5.19)$$

As in Sec. 5.2 we restrict ourselves here to one single transverse dimension. Note that the Schrödinger equation Eq. (5.19) is equivalent to the paraxial wave equation [Eq. (5.5)] with the correspondences [149]:

$$t \longleftrightarrow z, \quad \frac{m}{\hbar} \longleftrightarrow k, \quad V_{\text{ext}} \longleftrightarrow 0, \quad \psi \longleftrightarrow \tilde{u}. \quad (5.20)$$

In the Schrödinger equation the wavefunction $\Psi(x, t)$ propagates in time equivalently to the wavefront $\tilde{u}(x, z)$ along the axis z . Additionally, for a wave propagating in a medium with refractive index $n(x) = n_0 - n_2 x^2/2$, as in a “duct” (see [124] p. 652 and

the Errata) the correspondence for a harmonic oscillator potential $V_{\text{ext}} = m\omega^2 x^2/2$ is

$$\omega^2 \longleftrightarrow \frac{n_2}{n_0}. \quad (5.21)$$

Because of this equivalence, the ABCD matrix formalism and the Huygens-Fresnel integral can also be applied to the wavefunction Ψ to calculate its propagation through a cascade of harmonic potentials and sections of free space.

Let us look at a matter wave $\Psi(x, t)$ obeying Eq. (5.19) with, in general, a distorted density and phase distribution. The distribution in momentum² space $\bar{\Psi}(k)$ can be found by taking the Fourier transform of $\Psi(x)$, defined as

$$\bar{\Psi}(k) = \frac{1}{\sqrt{2\pi}} \int_{-\infty}^{\infty} \Psi(x) e^{-ikx} dx. \quad (5.22)$$

Before continuing with the ABCD formalism for matter waves, it is useful to briefly digress and introduce the Wigner distribution function (WDF). The Wigner distribution function $W(x, k)$ characterizes the state of a quantum system in phase space [154, 163–165]

$$W(x, k, t) \equiv \frac{1}{2\pi} \int_{-\infty}^{\infty} \Psi(x + x'/2, t) \Psi^*(x - x'/2, t) e^{-ikx'} dx', \quad (5.23)$$

where $*$ denotes the complex conjugate. The projections of the WDF have a physical meaning. The density distribution is

$$\int_{-\infty}^{\infty} W(x, k, t) dk = |\Psi(x, t)|^2, \quad (5.24)$$

and the momentum distribution is

$$\int_{-\infty}^{\infty} W(x, k, t) dx = |\bar{\Psi}(k, t)|^2. \quad (5.25)$$

The integral over the whole Wigner chart yields the total probability, equal to 1 for a normalized wavefunction

$$\int_{-\infty}^{\infty} \int_{-\infty}^{\infty} W(x, k, t) dx dk = 1. \quad (5.26)$$

Unless stated otherwise we will indeed take W (and Ψ) to be normalized in this way.

The Huygens-Fresnel integral [Eq. (5.8)] acts on the Wigner distribution function as a coordinate transformation. Specifically, let two functions $f(x)$ and $g(x)$ be related by the Huygens-Fresnel integral. Then the Wigner functions of $f(x)$ and $g(x)$ are related by [155]

$$W_g(x_2, k_2) = W_f(x_1, k_1), \quad (5.27)$$

²For notational convenience we actually use the wavevector k instead of the momentum $p = \hbar k$. Note for instance that the phase space area $\Delta x \Delta k$ is dimensionless.

where the coordinate transformation can be written in the ABCD form

$$\begin{pmatrix} x_2 \\ k_2 \end{pmatrix} = \begin{pmatrix} A & B \\ C & D \end{pmatrix} \begin{pmatrix} x_1 \\ k_1 \end{pmatrix}. \quad (5.28)$$

In this way we can conveniently express the transformation of a matter wave in phase space when it traverses a system of cascaded potentials represented by the total ABCD matrix.

5.3.2 ABCD matrices for matter waves

The aim of this section is to find the propagation of the second-order moments of a wavepacket through an ABCD system that represents our atom focusing experiment. Part of this section follows the work by Bastiaans [155].

Wigner chart

We start by drawing the simple Wigner chart for a one-dimensional, minimum-uncertainty (“Heisenberg-limited”), atomic wavepacket (with the same mathematical form as an ideal gaussian beam). The wavefunction is

$$\Psi_H(x) = \left(\frac{1}{2\pi\Delta x^2} \right)^{1/4} e^{-x^2/(2\Delta x)^2}. \quad (5.29)$$

The density distribution is symmetric around $x = 0$ (and $k = 0$). In the case $\langle x \rangle = \langle k \rangle = 0$, the second-order moments of the density distribution $\Delta x^2(t)$ and the momentum distribution $\Delta k^2(t)$ are defined as

$$\Delta x^2(t) = \int_{-\infty}^{\infty} x^2 |\Psi(x, t)|^2 dx, \quad (5.30)$$

$$\Delta k^2(t) = \int_{-\infty}^{\infty} k^2 |\bar{\Psi}(k, t)|^2 dk. \quad (5.31)$$

For $\Psi_H(x)$ [Eq. (5.29)] the product $\Delta x \Delta k = 1/2$, indeed the wavepacket is Heisenberg limited. Using this relation and Eq. (5.23) we arrive at the Wigner distribution function of the minimum-uncertainty wavepacket

$$W_H(x, k) = \frac{1}{\pi} e^{-\frac{k^2}{2\Delta k^2} - \frac{x^2}{2\Delta x^2}}. \quad (5.32)$$

A graphical representation of $W_H(x, k)$ is shown in Fig. 5.4.

propagation of second-order moments

In addition to the second-order moments of position and momentum [Eq. (5.30)] it is useful to define a ‘mixed moment’ Δ_{xk} employing the WDF

$$\Delta_{xk}(t) = \Delta_{kx}(t) = \int_{-\infty}^{\infty} \int_{-\infty}^{\infty} xkW(x, k, t) dx dk, \quad (5.33)$$

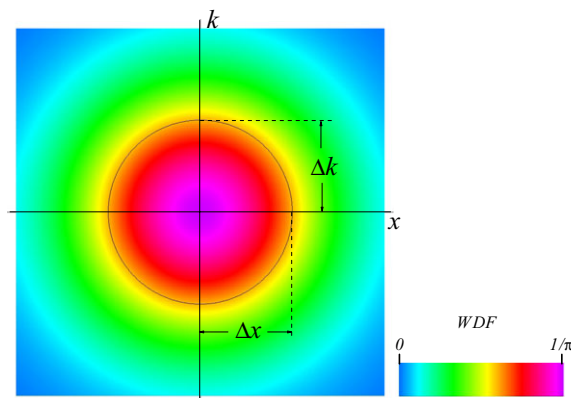


Figure 5.4: The Wigner distribution function (WDF) characterizes the state of a quantum system in phase space. Shown here is the Wigner distribution function of a minimum uncertainty wavepacket.

The propagation of the second-order moments Δx^2 , Δk^2 , Δ_{xk} and Δ_{kx} of a wavepacket that propagates through an ABCD system, between times t_1 and t_2 , is also conveniently written in matrix form [155]

$$\begin{pmatrix} \Delta x^2(t_2) & \Delta_{kx}(t_2) \\ \Delta_{xk}(t_2) & \Delta k^2(t_2) \end{pmatrix} = \begin{pmatrix} A & B \\ C & D \end{pmatrix} \begin{pmatrix} \Delta x^2(t_1) & \Delta_{kx}(t_1) \\ \Delta_{xk}(t_1) & \Delta k^2(t_1) \end{pmatrix} \begin{pmatrix} A & B \\ C & D \end{pmatrix}^T. \quad (5.34)$$

The ABCD matrices have unit determinant, therefore Eq. (5.34) shows that the determinant of the matrix of moments at t_2 equals that at t_1 : The determinant is an invariant of the propagation in this system

$$\Delta x^2(t)\Delta k^2(t) - \Delta_{xk}(t)\Delta_{kx}(t) \equiv \left(\frac{M^2}{2}\right)^2. \quad (5.35)$$

This determinant defines what was called the M^2 factor for matter waves by Riou and coworkers [146,148].

As an example, we write down M^2 for a classical ideal gas in a harmonic trap. Such a classical Boltzmann gas assumes a gaussian shape in a harmonic potential. Atoms do not interact and the density distribution can be treated separately for each direction. Consider a gas in thermal equilibrium so that the average position and momentum are not related and $\Delta_{xk} = 0$. In the axial direction the position spread is given by

$$\Delta x_T = \sqrt{\frac{k_B T}{m\omega_{\parallel}^2}}, \quad (5.36)$$

while the Boltzmann gas has a momentum spread

$$\Delta k_T = \frac{1}{\hbar} \sqrt{mk_B T}. \quad (5.37)$$

Equation (5.35) then yields the quality factor for a trapped Boltzmann gas

$$\frac{M^2}{2} = \frac{k_B T}{\hbar \omega_{\parallel}}. \quad (5.38)$$

Intuitively, it counts the number of thermally occupied modes of the axial harmonic oscillator potential.

Equation (5.34) describes how the second-order moments of a wavepacket propagate through a general ABCD system. The next step is then to write down the ABCD matrices corresponding to the specific transformations in phase space that we encounter in our focusing experiment. The focusing procedure consists of two stages: In the first stage we pulse on the harmonic potential $V(x) = m\omega^2 x^2/2$. In the second stage the magnetic potential is completely switched off, and the wavepacket propagates freely.

harmonic potential ABCD matrix

Consider a classical particle with position x and velocity $p(t)/m = \hbar k(t)/m$ in the harmonic potential $V(x) = m\omega^2 x^2/2$. The particle motion is described by the equations

$$\begin{aligned} \frac{dx}{dt} &= \frac{\hbar k(t)}{m}, \\ \hbar \frac{dk}{dt} &= m\omega^2 x(t). \end{aligned} \quad (5.39)$$

The general solution for the propagation of the particle from a time t_1 to a later time t_2 is

$$x_2 = x_1 \cos \omega t + \frac{\hbar}{m\omega} k_1 \sin \omega t. \quad (5.40)$$

From Eq. (5.40) and its derivative we can see that the ABCD matrix acting on the pair (x, k) is

$$\begin{pmatrix} x_2 \\ k_2 \end{pmatrix} = \begin{pmatrix} \cos \omega t & \frac{\hbar}{m\omega} \sin \omega t \\ -\frac{m\omega}{\hbar} \sin \omega t & \cos \omega t \end{pmatrix} \begin{pmatrix} x_1 \\ k_1 \end{pmatrix} \equiv \mathbf{M}_C \begin{pmatrix} x_1 \\ k_1 \end{pmatrix}. \quad (5.41)$$

To solve the Schrödinger equation for a quantum mechanical particle in a harmonic oscillator potential, Namias [166] has introduced the so-called fractional order Fourier transform (FrFT).³ To model our focusing potential we write the fractional Fourier transform for matter waves in the matrix representation. The ABCD matrix corresponding to the standard Fourier transform for matter waves acting on the pair (x, k) is

$$\mathbf{M}_{\text{FT}} = \begin{pmatrix} 0 & \hbar/m\omega \\ -m\omega/\hbar & 0 \end{pmatrix}, \quad (5.42)$$

³This mathematical method was applied later on in the field of optics by Mendlovic, Ozaktas and Lohmann [167, 168]. These authors made the connection between the fractional Fourier transform and the propagation of waves in a “duct”.

with ω the frequency of the harmonic oscillator. The ABCD matrix of a FrFT can be defined as

$$\mathbf{M}_{\text{FrFT}}^q = \mathbf{M}_{\text{FrFT}}, \quad (5.43)$$

so that if \mathbf{M}_{FrFT} is applied q times, the full Fourier transform is regained. \mathbf{M}_{FrFT} can be written in the general form that corresponds exactly to the classical matrix in (5.41)

$$\mathbf{M}_{\text{FrFT}} = \mathbf{M}_{\text{C}}, \quad (5.44)$$

where

$$\omega t = p \frac{\pi}{2} = \frac{\pi}{2q},$$

with p the fractional order of the FrFT. We have the full Fourier transform for $p = 1$. The fractional Fourier transform generates a rotation of the Wigner distribution function over an angle ωt in phase space (x, k) with a scaling factor $\hbar/m\omega$ [as is illustrated in Fig. 5.5(b)]. The value $\omega t = \pi/2$ corresponds to the standard Fourier transform that exactly interchanges the role of position and momentum.

free evolution ABCD matrix

Free temporal evolution of a matter wave simply means $k_2 = k_1$ and $x_2 = x_1 + \hbar k t / m$. In ABCD matrix form we write

$$\mathbf{M}_{\text{free}} = \begin{pmatrix} 1 & \hbar t / m \\ 0 & 1 \end{pmatrix}. \quad (5.45)$$

The above matrix is equivalent to the action of the Fresnel transform on the Wigner function. Using Eq. (5.27) we find that free propagation results in a shearing deformation of the Wigner distribution along the x -direction

$$W(x, k, t) = W\left(x + \frac{\hbar t}{m}k, k, t\right), \quad (5.46)$$

as is illustrated in Fig. 5.5(c).

From relation (5.34) and using M^2 [Eq. (5.35)] we get for the propagation of $\Delta x^2(t)$ of a wavepacket

$$\Delta x^2(t_2) = A^2 \Delta x^2(t_1) + 2AB \Delta_{xk}(t_1) + B^2 \frac{(M^2/2)^2}{\Delta x^2(t_1)}. \quad (5.47)$$

Filling in the elements of \mathbf{M}_{free} and starting from $t = t_{\text{focus}}$, the time of the narrowest width, where $\Delta_{xk} = 0$ we arrive at the equation that describes the free propagation of a matter wave

$$\Delta x^2(t) = \Delta x_0^2 \left[1 + M^4 \left(\frac{\hbar}{2m\Delta x_0^2} \right)^2 (t - t_{\text{focus}})^2 \right], \quad (5.48)$$

where we have written $\Delta x(t_{\text{focus}}) \equiv \Delta x_0$ for brevity. This is equivalent to the relation (5.18) when the correspondence (5.20) is used.

atomic wave focusing ABCD matrix

Finally, by multiplying \mathbf{M}_{FrFT} and \mathbf{M}_{Free} we obtain the complete ABCD matrix for the focusing of an atomic wave. We apply the magnetic lens in a pulsed fashion with a pulse time t_p followed by a free propagation time $t_{\text{free}} \equiv t - t_p$

$$\mathbf{M} = \begin{pmatrix} \cos \omega t_p - t_{\text{free}} \omega \sin \omega t_p & \frac{\hbar}{m\omega} \sin \omega t_p + \frac{\hbar t_{\text{free}}}{m} \cos \omega t_p \\ -\frac{m\omega}{\hbar} \sin \omega t_p & \cos \omega t_p \end{pmatrix}. \quad (5.49)$$

To find the focus time we require $A = 0$

$$t_{\text{focus}} = t_p + \frac{\cos \omega t_p}{\omega \sin \omega t_p}. \quad (5.50)$$

The scaling time t_{scale} gives the relation between initial velocity and final position

$$B(t_{\text{focus}}) = \frac{\hbar}{m\omega \sin \omega t_p} = \frac{\hbar}{m} t_{\text{scale}}. \quad (5.51)$$

With the above insights, the procedure can be simply extended to also include ramps in the potential of the form $\omega^2(t) = \omega_0^2 + \alpha t$, as is used in the experiments described in Sec. 5.6. This leads to an ABCD matrix similar to (5.49) that can be obtained by integration of Eq. (5.39).

5.3.3 Temperature of a focused non-interacting gas

In the case of a gas of non-interacting particles we can treat each particle separately. We can subsequently calculate the propagation for an ensemble of non-interacting particles through any ABCD system. Specifically, we calculate the width of a thermal ensemble that is focused using our procedure represented by an ABCD matrix such as (5.49). The width of the focused cloud yields the temperature of a gas.

The propagation of point particles in the classical limit is equivalent to the light-ray limit in optics. The gaussian density distribution of the Boltzmann gas along the trap axis is

$$n_l(x) = n_0 \exp[-\beta E(x)] = n_0 \exp\left[-\frac{1}{2}\beta m\omega_{\parallel}^2 x^2\right], \quad (5.52)$$

where n_0 is the density in the trap center and $\beta = (k_B T)^{-1}$. Using the temporal scaling of the gaussian cloud we find the evolution of the axial density distribution in time

$$n_l(x, t) = \frac{n_0 \Delta x_T}{\Delta \tilde{x}(t)} \exp\left[-\frac{1}{2}\left(\frac{x}{\Delta \tilde{x}}\right)^2\right], \quad \Delta \tilde{x}(t) = \sqrt{\Delta x_T^2 A^2(t) + \Delta k_T^2 B^2(t)}, \quad (5.53)$$

where we have used the matrix elements $A(t)$ and $B(t)$ and the thermal position and momentum spread Δx_T and Δk_T respectively [Eq. (5.36) and Eq. (5.37)].

For the case of a 3D harmonically trapped ideal Bose gas, at a temperature above

degeneracy, the density distribution is given in a semiclassical approximation by Eq. (2.25). It is useful to introduce the axial and radial harmonic oscillator lengths $l_{\parallel} = \sqrt{\hbar/m\omega_{\parallel}}$ and $l_{\perp} = \sqrt{\hbar/m\omega_{\perp}}$ respectively. We arrive at the linear density n_l along x by integrating Eq. (2.25) over both radial directions

$$n_l(x) = \frac{l_{\perp}^4}{\Lambda_T^5} g_{5/2}(ze^{-\beta m \omega_{\parallel}^2 x^2/2}). \quad (5.54)$$

If the cloud is focused in the axial direction we have access to the density n_p in momentum space [obtained after integration of Eq. (2.26)]

$$n_p(p_{\parallel}) = \frac{l_{\perp}^4}{m\omega_{\parallel}\Lambda_T^5} g_{5/2}(ze^{-\beta p_{\parallel}^2/2m}). \quad (5.55)$$

This momentum distribution translates into a spatial distribution in the focus as a function of the scaling time [as in Eq. (5.51)]

$$n_T(x, t_{\text{scale}}) = \frac{l_{\perp}^4}{\omega_{\parallel} t_{\text{scale}} \Lambda_T^5} g_{5/2}(ze^{-\beta m x^2/2t_{\text{scale}}^2}). \quad (5.56)$$

Note that for interacting clouds the treatment is not so straightforward (see Sec. 5.5). Note also that for 1D clouds the semiclassical treatment of the radial momentum distribution will fail.

5.4 Quasi-condensate as nonideal atomic beam

A quasi-condensate, at a temperature below $\sqrt{\gamma}T_d$, can be described as a macroscopic wavefunction obeying the Gross-Pitaevski equation [Eq. (2.30)] with a stable Thomas-Fermi like density profile but a phase that fluctuates along the symmetry axis [77] as was discussed in Sec. 2.4.4. The macroscopic wavefunction can be written as

$$\Psi_Q(x) = \sqrt{n_l(x)} e^{i\phi(x)}, \quad (5.57)$$

where n_l is the linear atomic density obeying Eq. (2.36). This quasi-condensate wavefunction is governed by inter-atomic interactions until its release from the trap when the interaction energy vanishes almost instantaneously (see Sec. 5.5 and references there). From that time onwards the atomic wave is well described by the linear Schrödinger equation in 1D, Eq. (5.19) and we can apply the ABCD formalism for matter waves to study its behavior. Note that the normalization of Ψ_Q is such that $\int |\Psi(x)|^2 dx = N$, the total particle number.

While the density of the 1D quasi-condensate is stable, the phase can fluctuate. Low energy excitations of elementary modes in the energy range $\hbar\omega_{\parallel} < \varepsilon \lesssim \mu$ result in an increased axial momentum spread. The excitations, that obey the Bogoliubov-de Gennes equations, with an energy spectrum given by Eq. (2.39) have a Bose distribution [Eq. (2.11) and $\mu = 0$]. The $k = 0$ mode of this spectrum is simply the ground state that has an arbitrary constant phase. All higher modes are

orthogonal to the ground state mode and have zero spatial average. The wavevector k counts the number of nodes in the corresponding mode.

In order to find the relation between the quasi condensate temperature and its width at the time of focus we exploit the analogy between the quasi-condensate matter wave Ψ_Q and the nonideal optical beam of Sec. 5.2.2. Following Riou *et al.* [146, 148] we have given the quality factor M^2 for matter waves in Eq. (5.35). Equation (5.34) showed that M^2 is invariant under linear ABCD transformations. We extend the work by Riou here by giving a physical interpretation of the quality factor by relating M^2 to the quasi-condensate temperature. We have seen in Sec. 5.3.2 that our focusing procedure is composed of a rotation followed by a shearing deformation of the Wigner chart. Figure 5.5 shows a schematic representation of the focusing process. An initial BEC in a cigar shaped trap has a large spatial extent and a small momentum spread [Fig. 5.5(a)]. The application of a harmonic potential pulse with frequency ω and duration t_p , performs a rotation with an angle $\theta = \omega t_p$ [Fig. 5.5(b)]. Free evolution, finally, performs a shearing deformation. The focus is reached when Δx reaches its minimum: $\hbar\Delta k/m\omega \sin\theta$ [Fig. 5.5(c)]. At t_{in} the

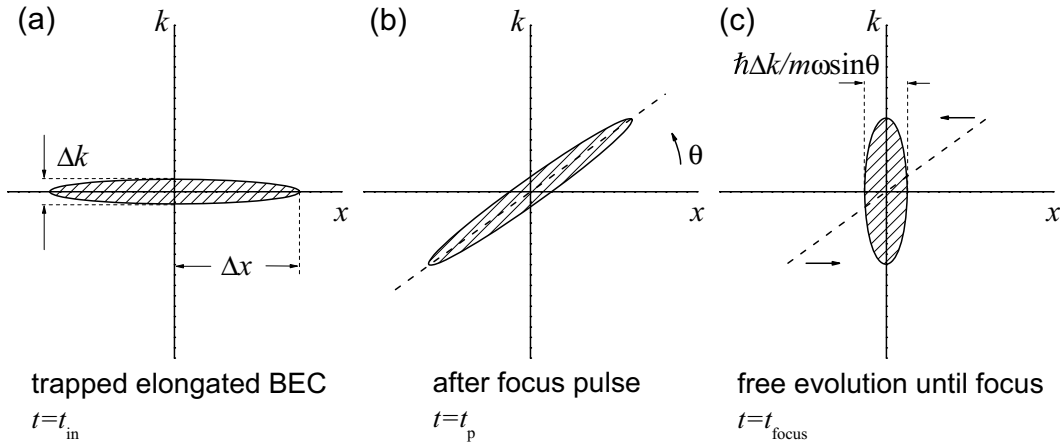


Figure 5.5: Schematic representation of the focusing process as a deformation of the WDF. (a) An initial BEC in a cigar shaped trap has a large spatial extent and a small momentum spread. (b) The application of a focussing pulse performs a rotation with an angle θ . (c) Free evolution performs a shearing deformation. The focus is reached when Δx reaches its minimum $\hbar\Delta k/m\omega \sin\theta$.

WDF of the equilibrium quasi-condensate at rest is aligned with both the position and momentum axes; i.e., there is no correlation between position and momentum, hence the mixed moment $\Delta_{xk} = 0$. Therefore, we can simplify Eq. (5.35) as

$$\frac{M^2}{2} = \Delta x(t_{in})\Delta k(t_{in}). \quad (5.58)$$

The axial momentum width $\Delta p(T)$, that is broadened by the thermal fluctuations of the phase, is expressed by the second-order moment of the projection of the WDF of Ψ_Q . A calculation of Δp for a harmonically trapped cloud, from the phase

fluctuation spectrum employing the local density approximation, was performed by Gerbier *et al.* [74, 169], who find the approximate relation

$$\Delta p^2(T) \approx \left(\frac{\alpha\hbar}{L}\right)^2 + \left(\frac{\beta\hbar}{l_\phi(T)}\right)^2, \quad (5.59)$$

with $\alpha = 2.0$, $\beta = 0.65$ and where the phase coherence length l_ϕ is inversely proportional to the temperature. The phase coherence length is given for the 1D homogeneous case by Eq. (2.40). For a harmonically trapped condensate in the 3D to 1D cross-over l_ϕ can be conveniently expressed as a function of the peak linear density $n_l(0)$ [74] if the local density approximation is employed

$$l_\phi = \frac{\hbar^2 n_l(0)}{mk_B T}. \quad (5.60)$$

The quasi-condensates in the experiments discussed in this chapter have $T \approx 10^2$ nK and $n_l(0) \approx 10^2 \mu\text{m}^{-1}$. For these numbers Eq. (2.40) yields $l_\phi \approx 6 \mu\text{m}$; much smaller than the cloud length $L \approx 10^2 \mu\text{m}$. Equation (5.59) then simplifies to

$$\Delta p = \hbar\Delta k = \frac{\beta\hbar}{l_\phi}. \quad (5.61)$$

Equation (5.58) relates the momentum width, Eq. (5.61), to the M^2 factor. We write $\Delta x(t_{\text{in}}) = \kappa L$ and arrive at

$$M^2 = 2\beta\kappa \frac{L}{l_\phi}, \quad (5.62)$$

where $\kappa \approx 1/\sqrt{5}$ for our typical parabola-like clouds.

Equation (5.62) allows us to express relation (5.48) explicitly as a function of the phase coherence length. We arrive at the expression for the free-space propagation of a phase-fluctuating quasi-condensate

$$\Delta x^2(t) = \Delta x_0^2 \left[1 + \left(2\beta\kappa \frac{L}{l_\phi} \right)^2 \left(\frac{\hbar}{2m\Delta x_0^2} \right)^2 (t - t_{\text{focus}})^2 \right]. \quad (5.63)$$

In Sec. 5.6 we use Eq. (5.63) in a model to fit our experimental results. This will allow us to determine l_ϕ , and subsequently to extract the temperature of the quasi-condensate from Eq. (5.60).

5.5 Weakly interacting condensate in a time dependent trap

The treatment of quasi-condensate propagation that was given in the previous section holds in the limit of vanishing interatomic interactions. In this section we treat the first part of the focusing process including interactions. We study the

time evolution of a trapped (quasi-)condensate in a changing harmonic potential. Three-dimensional trapped condensates respond differently to a change in potential as compared to the 1D trapped case. Our condensates are in the cross-over from 3D to 1D. It will be shown however that for small evolution times (our condensate is released shortly after the change in harmonic potential) the 3D and 1D solutions give quantitatively very similar results.

The trapped three-dimensional condensate has a parabolic shape in all spatial dimensions, see Sec. 2.4.1. The evolution of the cloud size can be described with scaling solutions [156–158]. We follow the notation of Castin and Dum [156]. The key point of this approach is that a parabolic cloud shape is maintained if the strength of the harmonic potential is changed in time. In particular, if the cloud is suddenly released from the trap it will expand maintaining its parabolic shape. The scaled cloud size b_i in direction $i = x, y, z$ evolves like

$$\ddot{b}_i = \frac{\omega_i^2(0)}{b_i(t)b_x(t)b_y(t)b_z(t)} - \omega_i^2(t)b_i(t). \quad (5.64)$$

In Sec. 5.6 we will show a numerical solution of (5.64) for our experimental focus pulse $\omega_{\parallel}(t)$, for the case of the 3D cigar with $\omega_{\parallel} \equiv \omega_x \gg \omega_y = \omega_z \equiv \omega_{\perp}$. Here we consider a sudden opening of a cylindrically symmetric trap at $t = 0$, Eq. (5.64) then simplifies to

$$\begin{aligned} \frac{d^2}{d\tau^2} b_{\perp} &= \frac{1}{b_{\perp}^3(t)b_{\parallel}(t)}, \\ \frac{d^2}{d\tau^2} b_{\parallel} &= \frac{\epsilon^2}{b_{\perp}^2(t)b_{\parallel}^2(t)}, \end{aligned} \quad (5.65)$$

where we have introduced the dimensionless time parameter $\tau = \omega_{\perp}(0)t$ and the small inverse aspect ratio $\epsilon = \omega_{\parallel}(0)/\omega_{\perp}(0) \ll 1$. To zeroth order in ϵ , sufficient for our experiments with $\epsilon \approx 1/400$, we find the solution for Eq. (5.65): $b_{\parallel} = 1$, i.e. the axial expansion of the cloud is negligible. The radial expansion scales as

$$b_{\perp}(\tau) = \sqrt{1 + \tau^2}, \quad (5.66)$$

and grows linearly for $t \gg \omega_{\perp}^{-1}$, i.e. shortly after release. We solve Eq. (5.64) numerically for more complicated, realistic temporal potential changes. An example is given in Fig. 5.6 where the red curves correspond to the shape oscillation in a 3D cloud that would appear if the focus pulse (an increase of the axial trapping frequency by a factor of three at $t = 0$) would be left on indefinitely. This results in large anharmonic amplitude oscillations showing the nonlinear character of the system. There is a visible difference between the periods of these large oscillations and that of small harmonic amplitude oscillations that have a quadrupole frequency $\omega_Q = \sqrt{5/2}\omega_{\parallel}$ (dashed red lines in Fig. 5.6) [170]. The condensates in our experiments are in the cross-over from the 3D to the 1D regime. This alters the scaling equation. In the 1D limit the axially compressed condensate will remain in the radial ground state as long as the axial dynamics is slow compared to the radial trap

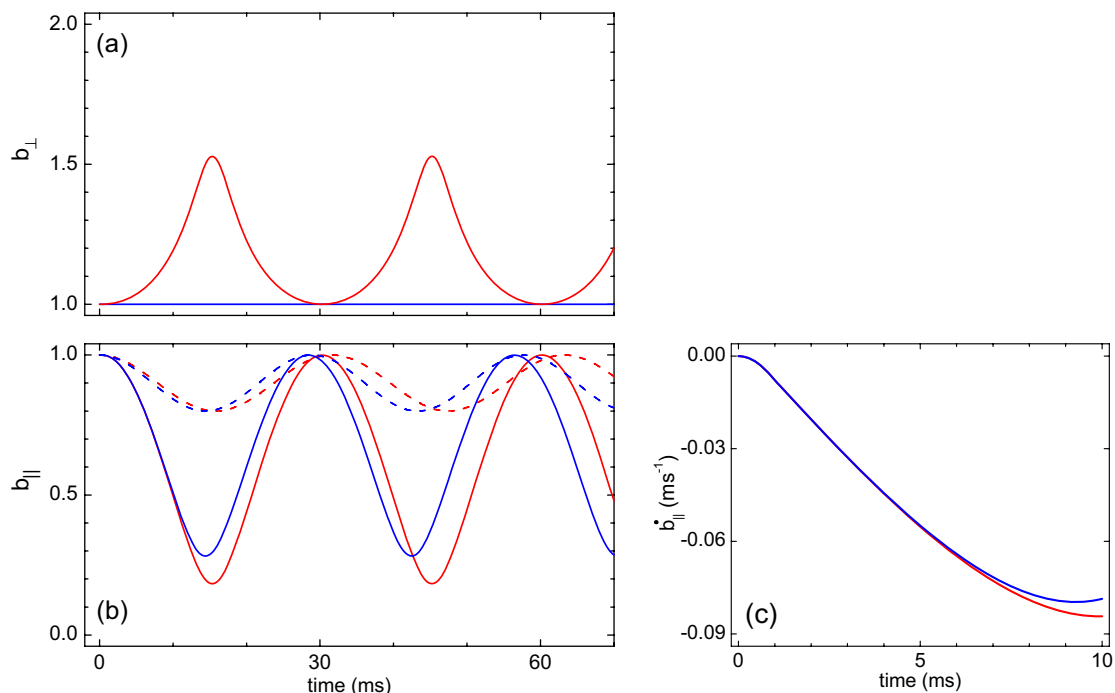


Figure 5.6: Large amplitude oscillations of an elongated BEC in a harmonic trap shows nonlinear behavior; red lines are solutions for the 3D case, the 1D solutions are drawn in blue. (a) Scaled radial size. (b) Scaled axial sizes dotted lines indicate the solutions in the limit of small oscillation amplitudes yielding $\omega_Q = \sqrt{5/2}\omega_{\parallel}$ in 3D and $\omega_Q = \sqrt{3}\omega_{\parallel}$ in 1D. (c) A comparison of the axial inward velocity for 3D and 1D directly after the start of an oscillation shows that the difference is negligible in the first 5 ms.

frequency and the interaction energy is negligible compared to the radial vibration energy $\mu \ll \hbar\omega_{\perp}$. In that limit the scaling equation reads

$$\ddot{b}_{\parallel} = \frac{\omega_{\parallel}^2(0)}{b_{\parallel}^2(t)} \left(\frac{\omega_{\perp}(t)}{\omega_{\perp}(0)} \right)^4 - \omega_{\parallel}^2(t)b_{\parallel}(t). \quad (5.67)$$

Figure 5.6 shows a comparison of the 1D and 3D results. The blue dashed line indicates the quadrupole frequency $\omega_Q = \sqrt{3}\omega_{\parallel}$ expected for small-amplitude oscillations. In Fig. 5.6(c) we plot \dot{b}_{\parallel} for the 1D and 3D case. For our focusing pulse of 5.4 ms (see Sec. 5.6), that is much shorter than the axial harmonic oscillator time, the difference between the inward velocity for the 1D and the 3D solution is negligible. We calculate a focus time for the 1D case that is only 0.3% longer than that for the 3D case. We model a sudden release from the trap by $\omega_{\perp} \rightarrow 0$ at the time of release thus cancelling the first term on the right hand side of Eq. (5.67) from the time of release onwards.

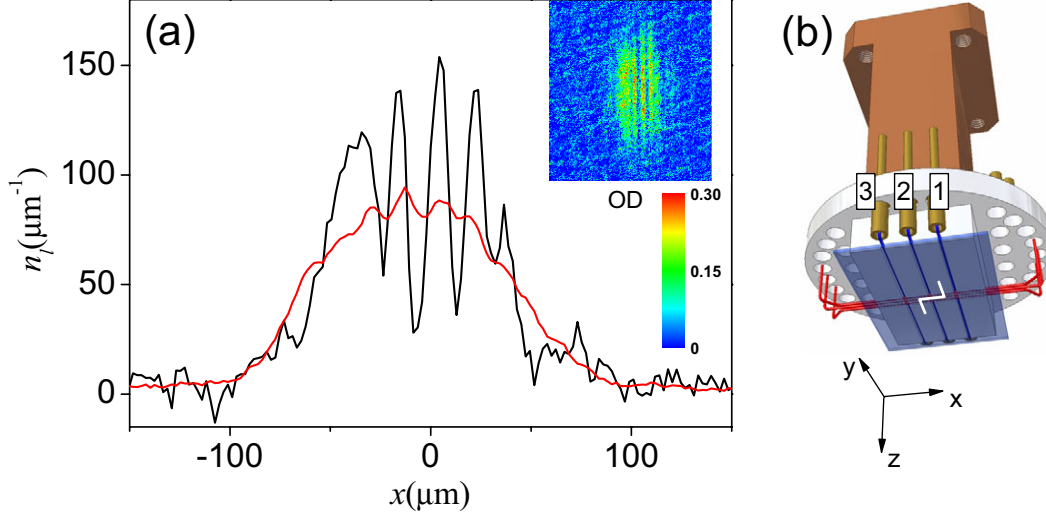


Figure 5.7: (a) Linear density of an elongated Bose gas after 20.5 ms of free expansion. Each single realization shows strong random density modulations, while the average density distribution is smooth and reproducible. An example single realization is shown in black, and the inset shows the corresponding optical density image before integration along z . The density distribution found after averaging 50 images is shown in red. The final frequency of the evaporation RF is 1.53 MHz for these images. (b) Our magnetic microtrap configuration, indicating the Z-wire on the atom chip, the two orthogonal sets of three miniwires, and the orientation of the frame of reference.

5.6 Experiments

The experimental procedure for the quasi-condensate focusing experiments starts with the generation of an elongated degenerate cloud as described in Sec. 4.2.7. For a final RF frequency of 1.53 MHz we have an almost pure quasi-condensate with an atom number of $8 \cdot 10^3$ and a linear density in the trap center of $80 \mu\text{m}^{-1}$, corresponding to $\mu \approx 0.6\hbar\omega_{\perp}$, i.e. on the 1D side of the dimensional cross-over ($\omega_{\perp}/2\pi = 3.28$ kHz, $\hbar\omega_{\perp}/k_B = 158$ nK, as stated in Sec. 4.2.7). We perform three types of measurements on the gas using absorption imaging in *time-of-flight* (after free fall from the trap), *in situ* (in the trap), and *focus* (after the application of a focusing pulse). We vary atom number and temperature of the gas by changing the final RF frequency. The gas is probed using absorption imaging with circularly polarized light resonant with the $|F = 2\rangle \rightarrow |F' = 3\rangle$ transition of the ^{87}Rb D2 line at one third of the saturation intensity. For the time-of-flight and *in focus* data described below, the quantization axis is defined by a small magnetic field of $B_y = 2$ G along the imaging axis, and the illumination time is $80 \mu\text{s}$. For the *in situ* measurements a shorter pulse of $20 \mu\text{s}$ is used to reduce blur due to heating of the atoms from photon recoil.

We start the description of our results with the time-of-flight data. A typical absorption image, and the resulting linear density along the axis is shown in Fig. 5.7(a). Each individual realization shows strong density fluctuations (black line), while averaging over 50 images result in a smooth distribution (red line). These fluctuations

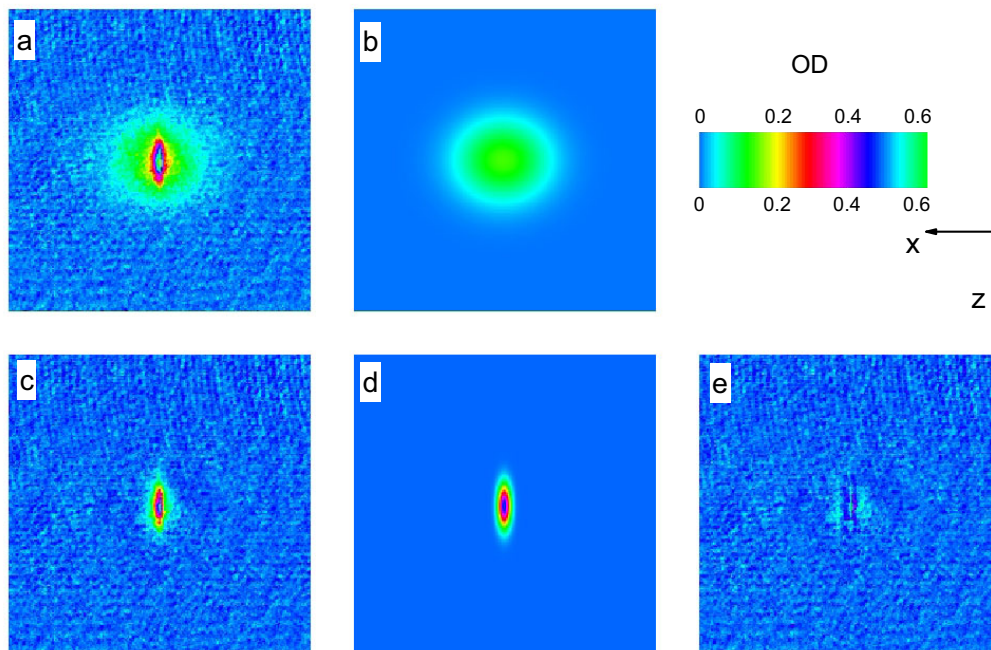


Figure 5.8: Fits to an average over 8 absorption images of a bimodal cloud during focusing. (a) Absorption image corresponds to final RF frequency of 1.57 MHz and a time of 17.3 ms after the start of the focus pulse. (b) Gaussian fit to thermal part, central area is excluded from the fit. (c) Data with fitted pedestal subtracted. (d) Gaussian fit to the central peak after subtraction of the pedestal. (e) Residue of the fit. The color coding of the optical density is indicated with a scale bar, each image size is $430 \times 430 \mu\text{m}^2$.

develop from the initial phase fluctuations of the degenerate gas and have been studied in detail for elongated 3D condensates with $\mu > \hbar\omega_{\perp}$ [171–173]. Images like these clearly establish the phase-fluctuating character of our one-dimensional atom clouds corresponding to $M^2 \gg 1$. A quantitative analysis of the axial density fluctuations is cumbersome, a point we will come back to in Sec. 5.8. Furthermore, the radial expansion, visible in the z direction, is also of limited use for characterizing temperature and chemical potential in our regime of $\mu < k_B T$ and $k_B T \approx \hbar\omega_{\perp}$, because the radial expansion is then dominated by the radial ground-state energy [39]. As we will now discuss, much more information can be readily obtained from the *focus* data.

The magnetic focusing pulse is created by ramping up the axial trapping frequency from 8.5 Hz to 20 Hz in 0.8 ms, maintaining this for 3.8 ms, and ramping back down to 8.5 Hz in 0.8 ms, as is illustrated in Fig. 5.9. The axial trapping potential is changed by sending a current of (5, -0.23, 5)A through miniwires 1, 2 and 3 respectively [see Fig. 5.7(b)]. This is followed by a sudden switch-off of the magnetic trap. During the focusing pulse the cloud length reduces by only 15%, see Fig. 5.6. After switching off the magnetic trap, the cloud expands in the radial direction on a timescale of $1/\omega_{\perp}$ (cf. Sec. 5.5), so that the interactions vanish rapidly

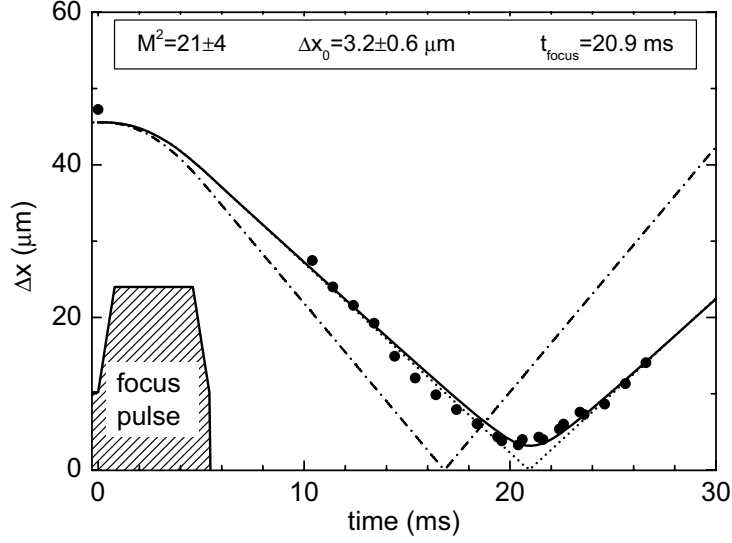


Figure 5.9: Experimental focus data (\bullet) and calculated axial cloud size for a BEC using the scaling solution (dotted line). A more realistic model based on the scaling solution during the focus pulse and the nonideal gaussian matter wave during free flight was fitted to the experimental data (straight line). For comparison we show the the classical trajectory of a point particle starting at rest calculated with the ABCD formalism (dash-dotted line). The timing of the axial potential pulse is indicated as the shaded area.

compared to the relevant axial timescale and the subsequent axial contraction can be treated as free propagation. After a free propagation time of ≈ 15 ms the cloud comes to an axial focus.

As an example, Fig. 5.8 shows an absorption image of a partly condensed cloud taken 17.3 ms after the start of the focus pulse corresponding to a final RF frequency of 1.57 MHz; we have averaged over 8 images. We perform a bimodal gaussian fit to the 2D atomic density distribution and extract atom number and axial and radial dimensions of the thermal and condensed parts of the bimodal cloud. The axial shape of the quasi-condensate upon focusing changes from approximately parabolic in the trap (see Sec. 2.4.3) to an approximately Lorentzian shape in the focus as was shown in Ref. [169]. In addition to that, the focal shape is blurred by the finite resolution limit of our detection optics. To treat density distributions with arbitrary shapes we measure the second-order moment [Eq. (5.30)] of the axial density. In practice, we do this by fitting the axial density distribution with the gaussian function $a \exp[-x^2/2\Delta x^2]$, where Δx is the second-order moment of the fitted Gaussian distribution. This procedure is expected to give good estimates for the position spread in the focal region where the atomic density distribution is well approximated by a gaussian, while it would overestimate the second-order moment for a trapped pure quasi-condensate profile [Eq. (2.36)].

We use the following hybrid model to describe the complete time evolution of a quasi-condensate during the focusing process. For the first part, the quasi-

condensate in the trap during a focusing pulse, we use the scaling equations (Sec. 5.5). We numerically integrate the scaling equations for our exact values of $\omega(t)$. Subsequently, to model the free evolution after release from the trap, we use the nonideal atomic beam description [Eq. (5.63)]. We match the two parts by calculating the cloud size $\Delta x(t_p)$ and inward velocity $\Delta \dot{x}(t_p)$ at the end of the focus pulse ($t = t_p$) from the scaling equations and impose these as boundary conditions for Eq. (5.63). These boundary conditions fix the “far-field divergence” of the matter wave and thereby the relation between M^2 and Δx_0 , leaving only a single free fitting parameter.

In Fig. 5.9 we show experimental focus data for an almost pure quasi-condensate of $8 \cdot 10^3$ atoms, corresponding to a final RF frequency of 1.53 MHz; each data point is obtained from a gaussian fit to an average over three absorption images. We fit the experimental data with the hybrid model (straight line) based on the scaling solution during the focus pulse and the nonideal matter wave, after that [Eq. (5.63)]. Indicated with the dotted line is the result of the scaling equation alone for a quasi-condensate. For comparison we show the classical trajectory of a point particle starting at rest calculated with the ABCD formalism (dash-dotted line). The timing of the axial potential pulse is indicated as the shaded area. The focus time resulting from the scaling equations is $t_{\text{focus}} = 20.9$ ms. The fit results in $\Delta x_0 = 3.2 \pm 0.6 \mu\text{m}$ and $M^2 = 21 \pm 4$. Assuming that M^2 is constant during the focus pulse, and with the peak linear density obtained from the *in situ* data, $n_l(0) = 80 \mu\text{m}^{-1}$, we find from Eq. (5.62) and Eq. (5.60) $T = 0.16 \pm 0.04 \mu\text{K}$.

In Fig. 5.10 we show the fit results for the partly condensed cloud, for a final RF frequency of 1.57 MHz (as in Fig. 5.8) corresponding to a thermal cloud containing $N_{\text{ex}} = 5.5 \pm 0.3 \cdot 10^3$ and a condensed part of $N_0 = 1.3 \pm 0.1 \cdot 10^3$. The thermal cloud radial expansion (\diamond) is approximately linear for $t \gg \omega_{\perp}^{-1}$ [Eq. (5.66)], while the axial size shows the effect of focusing (\bullet). The much smaller axial size of the condensed part is indicated with (\triangle). From a fit to the radial expansion of the thermal part we extract $T = 0.46 \pm 0.01 \mu\text{K}$. We calculate the axial size for this temperature with Eq. (5.53) and find the drawn black curve. The measured axial size at $t = 0$ clearly exceeds Δx_T [Eq. (5.36)] of an ideal Boltzmann gas. We attribute the broadening to the repulsive force of the non-negligible atomic interactions in the trap. We have modelled the effect of interactions using a reduced effective initial potential $V_{\text{eff}} = m\omega_{\text{eff}}^2 x^2/2$ with $\omega_{\text{eff}} = 6.7 \text{ s}^{-1} < \omega_x$ to match the calculated and measured initial sizes. If we calculate the propagation of the cloud width upon applying the same focus potential as before we obtain the dashed line in Fig. 5.10. The dash-dotted line indicates a fit to the central peak using the hybrid model where we have not only used Δx_0 as fitting parameter but have additionally let t_{focus} free in the fitting process. The resulting focus time is 18.1 ms, shorter than the 20.9 ms that we find for condensates of $8 \cdot 10^3$ atoms. We discuss this effect of a reduced focus time in Sec. 5.7.

In practice we have measured the *in focus* distribution at a fixed time $t = 20.9$ ms. Figure 5.11 shows results of *in focus* measurements when we lower the final RF frequency. In Fig. 5.11(a) we show the cloud temperatures determined from the quasi-condensate focal width (\triangle). The error bars are estimated based on the finite

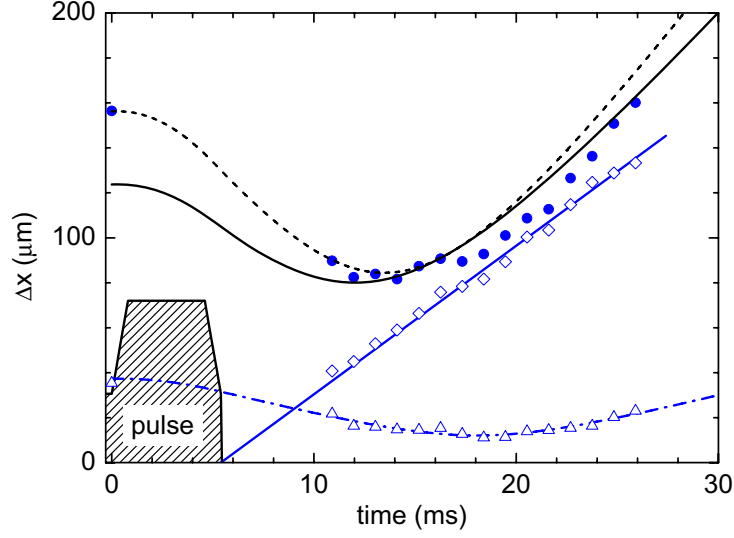


Figure 5.10: Experimental focus data for the thermal and condensed parts of a partially condensed cloud. The thermal cloud radial expansion (\diamond) is approximately linear for $t \gg \omega_{\perp}^{-1}$, while the axial size is clearly focussed (\bullet). The much smaller axial size of the condensed part is indicated with (\triangle), the dash-dotted line is the result of a fit using a hybrid model (see text). From a fit to the radial expansion of the thermal part we extract $T = 0.46 \pm 0.01 \mu\text{K}$. We calculate the axial size for this temperature and find the drawn (dotted) curves when we neglect (include) the repulsion of the thermal atoms by the condensate in the trap.

optical resolution of $\Delta x = 2.8 \pm 0.6 \mu\text{m}$ and on a 20% error in Δx_0 as found in the fit of Fig. 5.9. We compare the results with a temperature determined from the radial expansion energy of the thermal pedestal of the bimodal clouds (\diamond). In the latter temperature determination, the contribution to the expansion energy from the ground state has been neglected. The dash-dotted line is to guide the eye and indicates a ratio of 11 of the trap depth (set by ω_{RF}) and the cloud temperature. The dashed line corresponds to $\hbar\omega_{\perp}/k_B$. In Fig. 5.11(b) we show the atom number in the condensate (\triangle) and in the thermal component (\bullet). We discuss here the discrepancies between the two presented temperature measurements. We expect that the radial expansion data overestimate the temperature for $T \lesssim \hbar\omega_{\perp}$ where the radial size is dominated by the size of the harmonic oscillator ground state. On the other hand, for the central peak width, we have seen in Fig. 5.10 that the focus time shifts towards lower values for degenerate clouds at higher temperatures and lower linear densities indicating deviations from the quasi-condensate model that can be the reason for the deviating results for $\omega_{\text{RF}} \gtrsim 1.55 \text{ MHz}$. The presence of density fluctuations can explain the effect of a shift of the focus towards earlier times for higher final RF values as will be discussed below (see also Ch. 6).

It was shown in Fig. 5.9 that the quasi-condensate focusing description works fine for condensates with atom numbers $\sim 8 \cdot 10^3$. For lower atom numbers, however, we see deviations as is illustrated by the observed reduced focus time for condensates

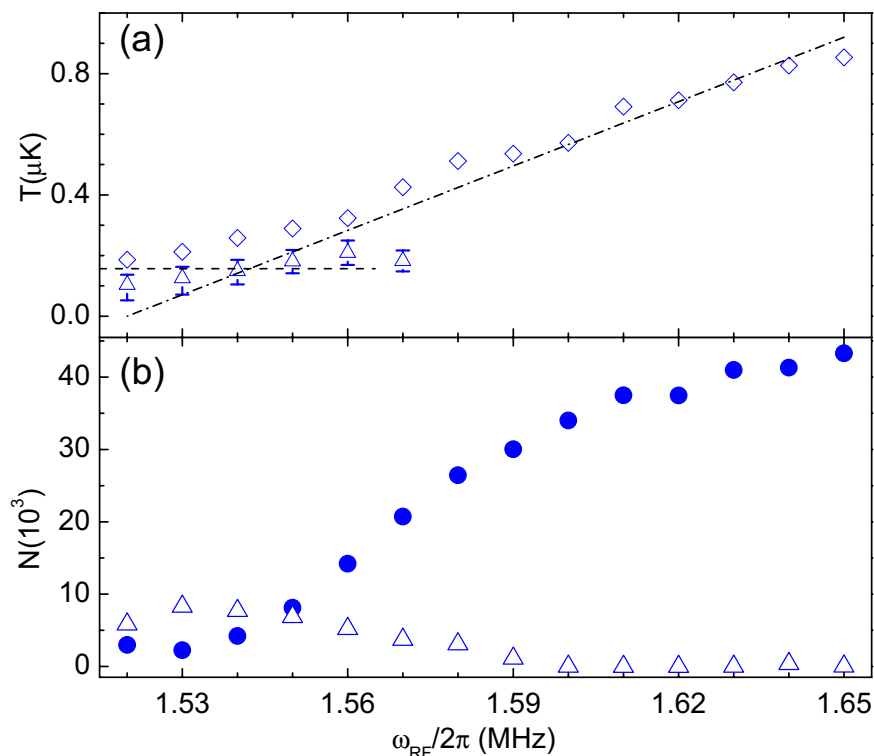


Figure 5.11: Characterization of the measured atomic clouds as a function of the final RF frequency ω_{RF} , as determined from Gaussian fits to the *in focus* data. (a) Temperature from the radial (\diamond) size of the broad Gaussian fit to the *in focus* data. The dash-dotted line is to guide the eye and indicates a ratio of 11 of the trap depth (set by ω_{RF}) and the cloud temperature. The dashed line corresponds to $\hbar\omega_{\perp}/k_B$. (b) Atom number from the *in focus* data: wide distribution (\bullet) and central peak (\triangle).

with lower atom number (triangles in Fig. 5.10). Figure 5.12 shows focus traces for varying atom number for the same final $\omega_{\text{RF}} = 1.52 \text{ MHz}$ of the evaporation trajectory, each datapoint comes from a gaussian fit to an absorption image averaged over typically 4 images. For comparison the focus data for $N = 8 \cdot 10^3$ presented in Fig. 5.9 are also plotted (black). We reduce the atom number by reducing the duration of the first part of the RF evaporative cooling ramp, while leaving the last part of the ramp unchanged. When the atom number is lowered we observe that the time of narrowest waist comes earlier. Additionally the waist size increases with decreasing atom number.

5.7 Discussion

The observed reduced focus time and increased focal width when the atom number is lowered, as presented in Fig. 5.12, likely stem from deviations in the degenerate cloud during the focus pulse from the mean-field description. This can be qualitatively understood in the following way: Although our experimentally observed clouds are

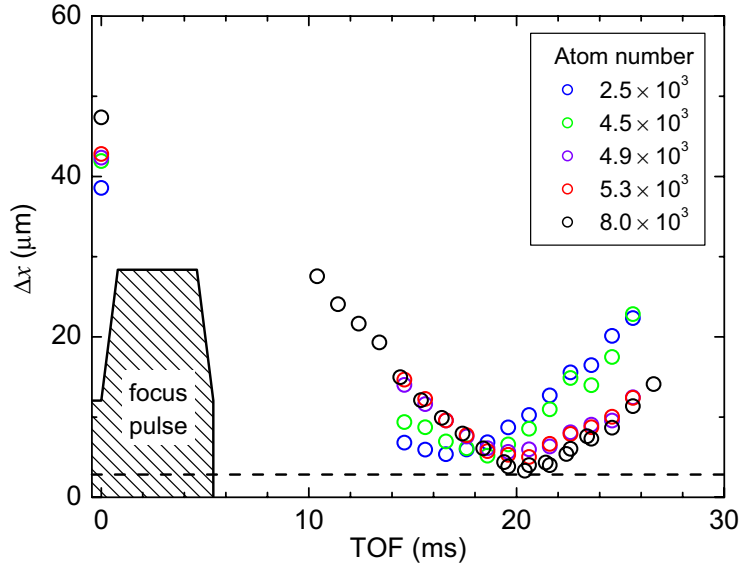


Figure 5.12: Experimental focus data for varying atom number. When the atom number is intentionally decreased we observe that the time of narrowest waist comes earlier. Atom numbers are indicated in the legend. The dashed line indicates the resolution limit.

in the cross-over from 3D to 1D we can best understand the effects of reduced coherence by considering the pure 1D case, corrections for the cross-over case do not qualitatively change the argument. When the atom number is lowered, even at constant temperature, the chemical potential decreases, cf. Fig. 2.2. As a result, the relative importance of the density fluctuations increases as is also visible in Fig. 2.2: Decreasing μ for constant finite temperature leads to an increasing two-particle local correlation $g^{(2)}$. We conclude that, by reducing the atom number at constant temperature, we enter the regime where $T \gtrsim \sqrt{\gamma}T_d$ (see Sec. 2.6.2) and the local value of $g^{(2)}$ becomes larger than 1. This means that the atomic density fluctuates and that the quasi-condensate starts to behave more and more like a decoherent thermal cloud. This results in a broadened focus that moves to earlier focus times as the coherence is reduced. The reduced focus time for decoherent clouds can also be seen in Fig. 5.9 by comparing the dotted line for a quasi-condensate with the dash-dotted line for non-interacting particles. In Ch. 6 we present a more detailed quantitative description of this reduced coherence based on the Yang-Yang thermodynamics.

We observe very narrow density distributions with Δx waists down to $3 \mu\text{m}$. These small features are close to the resolution limit of our optical system, see Sec. 3.9. The optical resolution could be improved, for example, by placing an objective lens *in vacuo* or outside a new and smaller vacuum system.

5.8 Conclusion and outlook

We have presented a model that describes the propagation of a quasi-condensate when it is focused in free flight. This model enables us to quantitatively extract the temperature of a phase-fluctuating quasi-condensate from the atom-beam quality factor M^2 . We have thus implemented a quasi-condensate thermometer. The temperature of the quasi-condensate is a direct measure of the phase coherence. By measuring the momentum spread of a focused quasi-condensate we probe the first-order correlation function. These correlations are the fundamental ingredient for the collective behavior of degenerate gases and of importance in possible applications of coherent matter waves like the guided-wave atom-interferometer [96].

We have also seen deviations from the quasi-condensate description in the regime where the mean-field approach is not valid, i.e. for low linear atomic density and relatively high temperature so that $T \gtrsim \sqrt{\gamma}T_d$. We will show in Ch. 6 that especially in this regime of reduced coherence the focus method is very useful to provide information on the correlations in the gas.

As was mentioned in Sec. 5.6 the analysis of the phase fluctuations after time-of-flight is cumbersome. The difficulties stem from the large modulation depth of the density fluctuations as shown in Fig. 5.7(a). We therefore can not use the analysis method developed by Petrov *et al.* [77, 171]. As an outlook we suggest a possible alternative approach, that we have tested preliminarily: A phase reconstruction method. This method is based on the description of the quasi-condensate as a matter wave, like light in the paraxial approximation. Employing the continuity equation it is possible to reconstruct the phase of a general wave in 1D from two measurements of the density distribution of this wave taken shortly after one another [174, 175]. In practice, we can not take two subsequent images of the same cloud because of the destructive absorption imaging method. However we know from theory and repeated measurements that the *in situ* density distribution is smooth and reproducible from shot to shot. The constant *in situ* density distribution can therefore serve as the first density measurement. Single *time-of-flight* density measurements could then be sufficient to reconstruct the phase of the matter wave. The implementation of this method and the analysis of its range of validity are beyond the scope of this thesis but form a nice outlook for further study.

Another topic for further study could be to use extensions of the ABCD formalism to describe a (trapped) weakly interacting gas. One could make use of an extended ABCD formalism that was given by Paré and Bélanger [176] to model light propagation in non-linear (Kerr) media. Additionally, a recent preprint by Impens and Bordé attacks the same problem [177].

6 Yang-Yang thermodynamics on an atom chip

In this chapter we describe measurements on the behavior of a weakly interacting nearly one-dimensional (1D) trapped Bose gas at finite temperature. We perform *in situ* measurements of spatial density profiles and show that they are very well described by a model based on exact solutions obtained using the Yang-Yang thermodynamic formalism, in a regime where other, approximate theoretical approaches fail. We demonstrate Bose gas focusing as a means to gain experimental access to the axial momentum distribution of the gas, and find good agreement with the *in situ* results.

6.1 Introduction

Reducing the dimensionality in a quantum system can have dramatic consequences. For example, the 1D Bose gas with repulsive delta-function interaction exhibits a surprisingly rich variety of physical regimes that is not present in 2D or 3D (see Sec. 2.6). This 1D Bose gas model is of particular interest because exact solutions for the many-body eigenstates can be obtained using a Bethe ansatz (Sec. 2.5.2). Furthermore, the finite-temperature equilibrium can be studied using the Yang-Yang thermodynamic formalism [36–38], a method also known as the thermodynamic Bethe ansatz (Sec. 2.5.3). The experimental achievement of ultracold atomic Bose gases in the 1D regime [39–41, 178] has attracted renewed attention to the 1D Bose gas problem [73, 84, 179–181] and is now providing previously unattainable opportunities to test the Yang-Yang thermodynamics.

In this chapter, we present the first direct comparison between experiments and theory based on the Yang-Yang exact solutions. The comparison is done in the weakly interacting regime and covers a wide parameter range where conventional models fail to quantitatively describe *in situ* measured spatial density profiles. Furthermore, we show that Bose gas focusing allows experimental access to the equilibrium momentum distribution of the 1D gas, which is difficult to obtain through other means.

Theory for the 1D Bose gas is summarized in Ch. 2. In brief, for a uniform 1D Bose gas, the key parameter is the dimensionless interaction strength $\gamma = mg_1/\hbar^2 n_1$, where m is the mass of the particles, n_1 is the 1D density, and g_1 is the 1D coupling

constant. An overview of the regimes in 1D is shown in Fig. 2.4. At low densities or large coupling strength such that $\gamma \gg 1$, the gas is in the strongly interacting or Tonks-Girardeau regime [42, 43, 53]. The opposite limit $\gamma \ll 1$ corresponds to the weakly interacting gas. Here, for temperatures below the temperature of quantum degeneracy $T_d = \hbar^2 n_1^2 / 2mk_B$, one distinguishes two regimes [59]. (i) For sufficiently low temperatures, $T \ll \sqrt{\gamma} T_d$, the equilibrium state is a quasi-condensate with suppressed density fluctuations and fluctuating phase. The system can be treated by the mean-field approach and by the Bogoliubov theory of excitations. The 1D character manifests itself through long-wavelength phase fluctuations resulting in a finite phase coherence length $l_\phi = \hbar^2 n_1 / mk_B T$ which greatly exceeds the mean-field correlation length $l_c = \hbar / \sqrt{m n_1 g_1}$. (ii) The temperature interval $\sqrt{\gamma} T_d \ll T \ll T_d$ corresponds to the quantum decoherent regime [59], where both the density and the phase fluctuate. Here, the condition $l_c \ll l_\phi$ required for the existence of a quasi-condensate is no longer satisfied and the system can be treated as a degenerate ideal gas combined with perturbation theory in g_1 . At temperatures near the crossover to the quasi-condensate, $T \sim \sqrt{\gamma} T_d$, neither of the above mentioned approximate theoretical approaches work and one has to rely on the numerical solution to the exact Yang-Yang equations, as we show in this chapter.

Experiments on 1D Bose gases are usually carried out in harmonic traps with strong transverse confinement and weak confinement along the symmetry axis, $\omega_\perp \gg \omega_\parallel$. A trapped gas is in the 1D regime if both temperature and chemical potential are small with respect to the radial excitation energy, $k_B T, \mu \ll \hbar \omega_\perp$. The effective 1D coupling can be expressed through the 3D scattering length a as $g_1 \simeq 2\hbar \omega_\perp a$ if $a \ll (\hbar / m \omega_\perp)^{1/2}$ [33][Eq. (2.34)]. Various physical regimes of a harmonically trapped 1D gas have been discussed in Refs. [34, 70, 76, 85]. The above classification of the regimes for the uniform gas can be applied locally to the trapped gas if the conditions for the local density approximation (LDA) are met [70, 76, 85]. It was recognized early on that the physics of the degenerate part of the trapped cloud is already effectively 1D if the weaker condition $\mu < \hbar \omega_\perp$ is satisfied [39–41, 178].

We experimentally investigate the behavior of a weakly interacting trapped Bose gas ($\gamma \approx 10^{-2}$) in the regime where $\mu < \hbar \omega_\perp$ and $k_B T \simeq \hbar \omega_\perp$. Similar measurements to our *in situ* data were previously performed at higher chemical potentials and higher temperatures [60], in which case the observed density profiles were found to be in disagreement not only with a pure quasi-condensate description and with an ideal-gas description, but also with a model based on a Hartree-Fock approximation. Our approach here is different in that we fit the data using a model based on the solutions to the exact Yang-Yang equations [36, 59] and use these fits to extract the chemical potential and the temperature of the gas. The model describes our *in situ* data very well, in contrast to the more conventional descriptions.

The outline of this chapter is as follows. In Sec. 6.2 a short summary of the used methods is given. In Sec. 6.3 and Sec. 6.4 we describe the data obtained with the *in situ* and *in focus* methods respectively. In Sec. 6.5 the presented data are discussed and compared with theory. Finally, in Sec. 6.6, we conclude this chapter and give an outlook to further experimental and theoretical investigations.

6.2 Methods

For (nearly) 1D clouds, it is difficult to obtain experimental access to the axial momentum distribution. The conventional time-of-flight method does not work for this purpose, mainly because the cloud hardly expands axially beyond its long initial length. In addition, we observe strong density fluctuations, similar to the example given in Fig. 5.7(a), that develop in time-of-flight from the initial phase fluctuations of our 1D degenerate clouds further complicating the analysis. Previous work for elongated 3D condensates with $\mu > \hbar\omega_{\perp}$ can be found in Refs. [171, 172]. Bragg spectroscopy has been demonstrated as a means to obtain the axial momentum distribution of phase-fluctuating condensates [172], but this requires averaging over many realizations of the experiment.

We gain experimental access to the axial momentum distribution using Bose gas focusing a technique that is described in detail in Ch.5. In brief, we apply a short, strong axial harmonic potential yielding a kick to the atoms proportional to their distance from the trap center (analogous to the action of a lens in optics), followed by free propagation. As a result the atoms come to a focus, at which time the axial density distribution reflects the axial momentum distribution before focusing. Initial phase fluctuations do not lead to density fluctuations in the focus, but instead result in a finite width of the cloud [127]. Since the focusing brings all atoms together axially, the signal level is high, even for a single realization. As we will show, averaging over a few shots is sufficient to obtain high signal-to-noise ratio.

The core of our experimental setup is a magnetic microtrap that is described in Sec. 3.3. The experimental procedure to prepare our cold atom samples is described in Ch. 4. In short, we trap 2×10^7 ^{87}Rb atoms in the $F = 2, m_F = 2$ state in a tight magnetic trap near the chip surface, and perform forced evaporative cooling by applying a radio frequency (RF) field. The frequency ω_{RF} is ramped down from 27 MHz to 1.7 MHz relatively quickly (in 180 ms) to purposely reduce the atom number. Apart from that the experimental procedure is identical to that of Ch. 5. Before reaching degeneracy we relax the axial confinement to a final trap with $\omega_{\perp}/2\pi = 3280$ Hz, $\omega_{\parallel}/2\pi = 8.5$ Hz, and a bottom corresponding to $\omega_{RF}/2\pi = 1.518(2)$ MHz. The current in the Z-wire is set at 2.25 A, and the distance of the cloud to the chip surface is 90 μm . In this trap we perform a slower ramp (450 ms) to the final RF frequency. An additional 300 ms of plain evaporation allows the damping of residual quadrupole collective oscillations in the cloud to the point where these oscillations are no longer visible.

6.3 *In situ* density profiles

In Fig. 6.1(a)-(e) we show the linear density of atomic clouds in the magnetic trap for different final RF frequencies. These data were obtained by *in situ* absorption imaging and integrating the atom number along z . The absolute atom number was calibrated using time-of-flight data. Each curve is an average of ~ 18 images taken under identical circumstances. Since all of our data was taken for $\mu < \hbar\omega_{\perp}$, we

expect¹ that the interactions will significantly affect only the distribution in the radial *ground* state, while the population in the radially *excited* states can to a good approximation be described by the ideal-gas distribution. This leads to the following model that was used to analyze the *in situ* data.

We start from the solution to the Yang-Yang integral equations for a finite-temperature uniform 1D Bose gas at thermal equilibrium [36]. As was shown in Sec. 2.5.3, this yields numerical results for both the equation of state $n_{YY}(\mu, T)$ and the local pair correlation function $g^{(2)}$ [59]. The local density approximation is then used to account for the axial potential via a varying chemical potential $\mu(x) = \mu - V(x)$. This approach is expected to be valid as long as the axial potential is smooth on the scale of the relevant correlation lengths [70, 85].

Our axial trapping potential was characterized with standard methods using both the measurement of *in situ* density profiles at high T [129] and the dipole mode oscillation frequency in the trap center. The curvature in the trap center corresponds to a frequency of 8.5 Hz, while for larger $|x|$ (in the wings of the warmer clouds) the curvature corresponds to a frequency of 6.4 Hz [128].

Since our temperature is on the order of the radial level splitting, $\hbar\omega_{\perp}/k_B = 158$ nK, the fraction of the gas which occupies radially excited states can not be neglected. We account for this fraction by summing over radially excited states [radial quantum number j , degeneracy $(j + 1)$] and treating each radial state as an independent ideal 1D Bose gas in thermal equilibrium with the gas in the radial ground state, $\mu_j(x) = \mu(x) - j\hbar\omega_{\perp}$. Within this model the density is given by

$$n_i(x, \mu, T) = n_{YY}(\mu(x), T) + \sum_{j=1}^{\infty} (j + 1)n_e(\mu_j(x), T). \quad (6.1)$$

For the radially excited states, we use the result of the LDA for the 1D ideal gas, $n_e(\mu, T) = g_{1/2}(\exp(\mu/k_B T))/\Lambda_T$ where $g_{1/2}$ is a Bose function and $\Lambda_T = (2\pi\hbar^2/mk_B T)^{1/2}$ is the thermal de Broglie wavelength (see Sec. 2.3.2). In this model, the radially excited states act as a bath for particle and energy exchange with the radial ground state. The resulting fits are shown as solid lines in Fig. 6.1(a)-(e) and describe our data very well. The fitted values of T and μ are displayed in Fig. 6.2.

6.4 *In focus* density profiles

We now turn to the *in focus* measurements which give access to the axial momentum distribution of the gas (see Ch. 5). The focusing pulse is created in the same way as described in Sec. 5.6, by ramping up the axial trapping frequency from 8.5 Hz to 20 Hz in 0.8 ms, maintaining this for 3.8 ms, and ramping back down to 8.5 Hz in 0.8 ms. This is followed by a sudden switch-off of the magnetic trap. During the focusing pulse the cloud length reduces by less than 20%. After switching off the magnetic trap, the cloud expands in the radial direction on a timescale of $1/\omega_{\perp}$, so that the interactions vanish rapidly compared to the relevant axial timescale and the

¹For our trap parameters the condition $\mu < \hbar\omega_{\perp}$ corresponds to $n < 3/4a \approx 150 \mu\text{m}^{-1}$, see Sec. 2.4.3

subsequent axial contraction can be treated as free propagation. We experimentally observe that the cloud comes to an axial focus after a free propagation time of 13 ms. The focus time is reduced as compared to the measurements performed at higher linear densities that were presented in Sec. 5.6; these data could be modelled using a mean-field description. The observed earlier time of focus for the data presented here indicates the failure of the mean-field description – as was already hinted at in Sec. 5.7, Fig. 5.12 – that will be discussed in the next section.

In Fig. 6.1(f)-(i) we show the axial density distribution obtained in the focus, averaged over typically 10 shots, for final RF frequencies similar to the *in situ* data in Fig. 6.1 (a)-(e). Here, in contrast to the *in situ* results, one can clearly distinguish a narrow peak from a broad pedestal for RF values below 1.56 MHz [Figs. 6.1(h)-(j)]. The Yang-Yang solution does not yield the momentum distribution and thus it can not be used to fit to the *in focus* data. Instead, to quantify the observation of the bimodal structure we first fit a 2D Gaussian to the wings of the atomic density distribution. In a second step we fit a narrow Gaussian to the residual peak in the center. The fitted curves are shown after integration in the z direction in Fig. 6.1(f)-(j), and describe the observed *in focus* distributions well.

6.5 Analysis and discussion

Fig. 6.2(c) shows the resulting atom numbers in the wide and narrow part of the momentum distribution; we also plot the atom numbers from the Yang-Yang model in the radial ground state, in the radially excited states, and atoms in the radial ground state experiencing $\mu(x) > 0$. Comparing the *in situ* and the *in focus* data, we conclude that: (i) the momentum distribution becomes bimodal around the point where the global chemical potential μ crosses zero and becomes positive; and (ii) the narrow part of the momentum distribution is dominated by the atoms in the radial ground state (described by n_{YY}), while the wide part is dominated by atoms in the radially excited states.

A further comparison between the *in focus* and *in situ* results can be made as follows. Estimates for the temperature can be obtained from the Gaussian fit to the wide part of the *in focus* data, by assuming that the tails (where degeneracy is negligible) are well described by Boltzmann statistics. The resulting temperatures are shown in Fig. 6.2(a). The agreement with the temperature extracted from the *in situ* data is reasonable. We attribute the remaining discrepancy to the approximations implicit in the above interpretation of the Gaussian fit results, which neglects the discrete radial level structure and the contribution of the radial ground state to the wide part of the axial momentum distribution.

The failure of both the ideal-gas and quasi-condensate descriptions is illustrated in Fig. 6.1(c)-(e). The key point here is the following. The Yang-Yang thermodynamic equations yield a smooth equation of state $n_{YY}(\mu, T)$, including the region around $\mu(x) = 0$, as is plotted in Fig. 2.2. This deviates dramatically from both the ideal-gas description (diverging density as μ approaches zero from below) and the quasi-condensate description (vanishing density as μ approaches zero from above).

The region in $\mu(x)$ (and consequently in $n_{YY}(x)$) where this discrepancy is significant is particularly large for our parameters, and the Yang-Yang thermodynamic solutions are essential for a proper description of the *in situ* data. For example, for our trap parameters and $T = 140$ nK [as in Fig. 6.1(e)] the point $T = \sqrt{\gamma}T_d$ (or equivalently $l_\phi = 2l_c$) corresponds to $n_{YY} = 20 \mu\text{m}^{-1}$. At this temperature the Yang-Yang equation of state deviates significantly from the ideal-gas and quasi-condensate description over the range $2 \lesssim n_{YY}(x) \lesssim 30 \mu\text{m}^{-1}$ and the calculated value of the local pair correlation function $g^{(2)}$ varies smoothly between 1.1 and 1.8 in this range (see Fig. 2.2). This differs from the ideal-gas value of 2 and the quasi-condensate value of ≈ 1 , and confirms the breakdown of the Hartree-Fock model of Ref. [60] which sets $g^{(2)} = 2$.

6.6 Conclusion and outlook

In conclusion, we have found excellent agreement between *in situ* measurements of the spatial linear density of a nearly 1D trapped Bose gas and a model based on the exact Yang-Yang solutions. We have measured the corresponding momentum distribution for which currently no theoretical comparison is available. We expect that these results will stimulate further theoretical and experimental studies of Yang-Yang thermodynamics. In addition, our findings should be relevant to experiments performed at similar linear densities and temperatures, such as guided-wave atom lasers [147] and atom-chip based interferometers [96].

Figure 6.1 on next page: Linear atomic density from absorption images obtained *in situ* (a)-(e) and *in focus* (f)-(j). The data from top to bottom correspond to lowering the value of the final RF evaporation frequency as indicated. *In situ*: solid black lines are fits using Yang-Yang thermodynamic equations (see text). The values of μ and T resulting from the fits are shown in the figure. Red line: ideal Bose gas profile showing divergence for $\mu = 0$. Green line in (e): quasi-condensate profile with the same peak density as the experimental data. *In focus*: blue lines are the sum of two independent Gaussian fits – one to the wings (light blue) and one to the central part of the atomic density distribution.

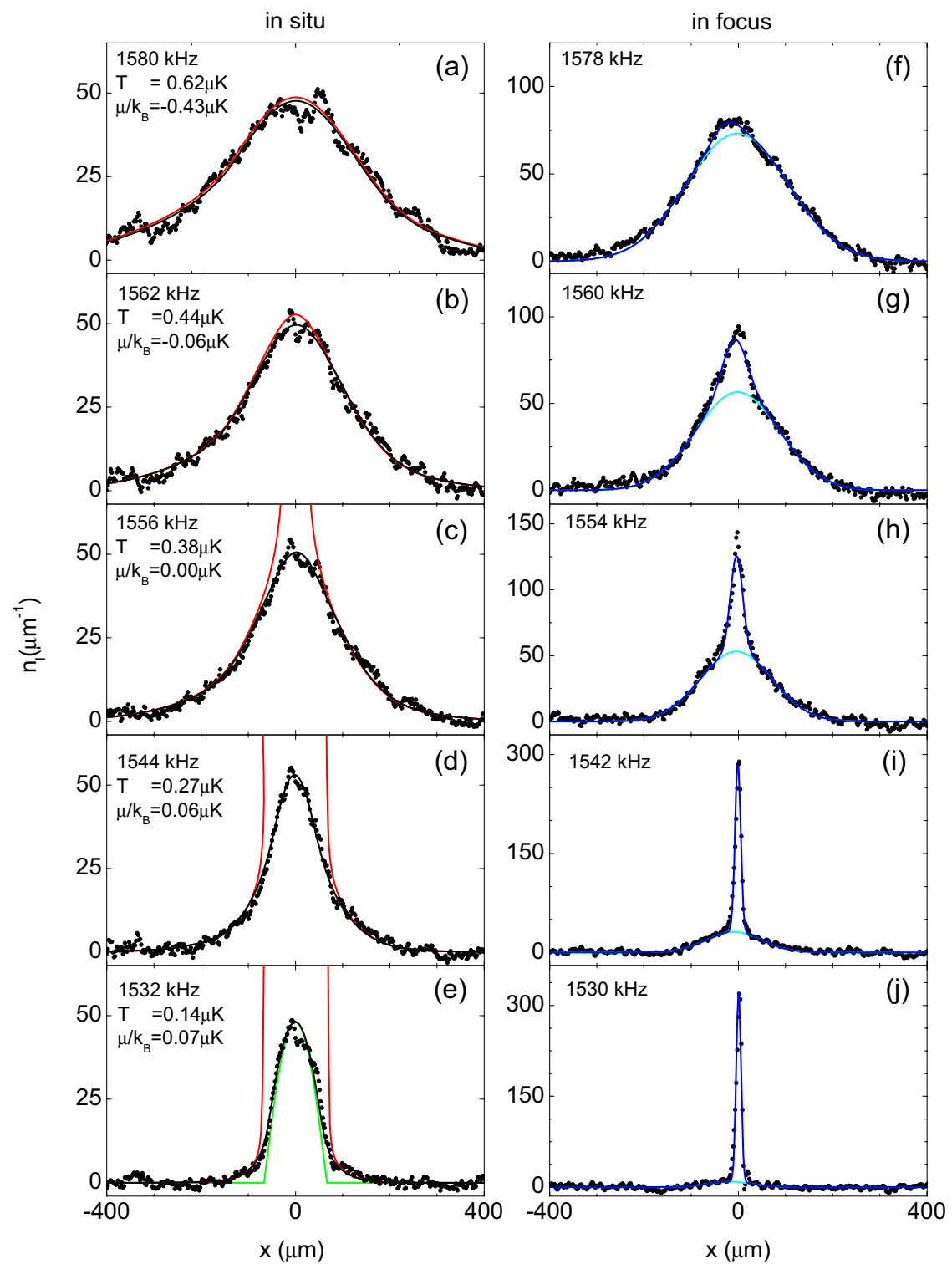


Figure 6.1: Linear atomic density from absorption images obtained *in situ* (a)-(e) and *in focus* (f)-(j).

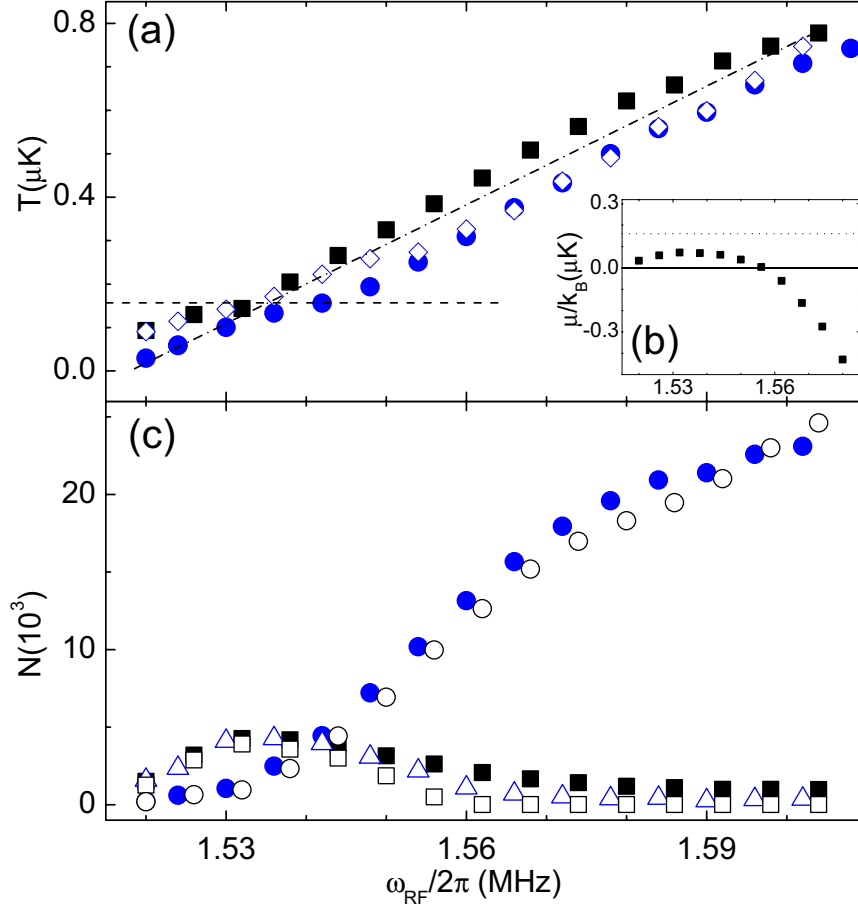


Figure 6.2: Characterization of the measured atomic clouds as a function of the final RF frequency ω_{RF} , as determined from fits of the Yang-Yang model to the *in situ* data and Gaussian fits to the *in focus* data. (a) Temperature from the *in situ* data (■) and from the radial (◇) and axial (●) size of the broad Gaussian fit to the *in focus* data. The dash-dotted line is to guide the eye and indicates a ratio of 11 of the trap depth (set by ω_{RF}) and the cloud temperature. The dashed line corresponds to $\hbar\omega_{\perp}/k_B$. (b) Chemical potential from the Yang-Yang fit. The dashed line indicates $\hbar\omega_{\perp}/k_B$. (c) Atom number from the *in focus* data: wide distribution (●) and central peak (△); from the Yang-Yang model fit to the *in situ* data: atoms in the radial ground state (■), in radially excited states (○), and atoms in the radial ground state experiencing $\mu(x) > 0$ (□).

References

- [1] S. Bose. *Plancks gesetz und lichtquantenhypothese*. Z. Phys. **26**, 178 (1924).
- [2] A. Einstein. *Quantentheorie des einatomigen idealen gases*. Sitz.ber., K. Preuss. Akad. Wiss. p. 261 (1924).
- [3] H. Kamerlingh-Onnes. *On the sudden change in the rate at which the resistance of mercury disappears*. Communications from the Physical Laboratory of the University of Leiden **124c** (1911).
- [4] H. Kamerlingh-Onnes. *The liquefaction of helium*. Communications from the Physical Laboratory at the University of Leiden **108** (1908).
- [5] P. Kapitza. *Viscosity of liquid helium below the λ point*. Nature **141**, 74 (1938).
- [6] J. Allen and A. Misener. *Flow of liquid helium II*. Nature **141**, 75 (1938).
- [7] F. London. *The λ -phenomenon of liquid helium and the Bose-Einstein degeneracy*. Nature **141**, 643 (1938).
- [8] L. Tisza. *Transport phenomena in helium II*. Nature **141**, 913 (1938).
- [9] S. Balibar. *The discovery of superfluidity*. J. Low Temp. Phys. **146**, 441 (2007).
- [10] H. F. Hess. *Evaporative cooling of magnetically trapped and compressed spin-polarized hydrogen*. Phys. Rev. B **34**, 3476–3479 (1986).
- [11] N. Masuhara *et al.* *Evaporative cooling of spin-polarized atomic hydrogen*. Phys. Rev. Lett. **61**, 935–938 (1988).
- [12] I. Silvera and J. Walraven. *Spin-polarized atomic hydrogen*. in: Progr. Low Temp Phys. **X**, 139–370 (1986).
- [13] T. Hänsch and A. Shawlow. *Cooling of gases by laser radiation*. Opt. Commun. **13**, 68 (1975).
- [14] W. D. Phillips and H. Metcalf. *Laser deceleration of an atomic beam*. Phys. Rev. Lett. **48**, 596–599 (1982).
- [15] S. Chu *et al.* *Three-dimensional viscous confinement and cooling of atoms by resonance radiation pressure*. Phys. Rev. Lett. **55**, 48–51 (1985).

- [16] C. Cohen-Tannoudji and W. Phillips. *Physics Today* **43**, 33 (1990).
- [17] M. H. Anderson *et al.* *Observation of Bose-Einstein condensation in a dilute atomic vapor.* *Science* **269**, 198–201 (1995).
- [18] K. B. Davis *et al.* *Bose-Einstein condensation in a gas of sodium atoms.* *Phys. Rev. Lett.* **75**, 3969–3973 (1995).
- [19] C. C. Bradley, C. A. Sackett, J. J. Tollett, and R. G. Hulet. *Evidence for Bose-Einstein condensation in an atomic gas with attractive interactions.* *Phys. Rev. Lett.* **75**, 1687–1690 (1995).
- [20] C. C. Bradley, C. A. Sackett, J. J. Tollett, and R. G. Hulet. *Evidence of bose-einstein condensation in an atomic gas with attractive interactions [phys. rev. lett. 75, 1687 (1995)].* *Phys. Rev. Lett.* **79**, 1170 (1997).
- [21] C. C. Bradley, C. A. Sackett, and R. G. Hulet. *Analysis of in situ images of bose-einstein condensates of lithium.* *Phys. Rev. A* **55**, 3951–3953 (1997).
- [22] C. C. Bradley, C. A. Sackett, and R. G. Hulet. *Bose-einstein condensation of lithium: Observation of limited condensate number.* *Phys. Rev. Lett.* **78**, 985–989 (1997).
- [23] F. London. *Superfluids.* John Wiley and Sons New York (1950).
- [24] V. L. Ginzburg and L. D. Landau. *Zh. Eksperim. i Teor. Fiz.* **20**, 1064 (1950).
- [25] O. Penrose and L. Onsager. *Bose-Einstein condensation and liquid helium.* *Phys. Rev.* **104**, 576–584 (1956).
- [26] C. N. Yang. *Concept of off-diagonal long-range order and the quantum phases of liquid He and of superconductors.* *Rev. Mod. Phys.* **34**, 694–704 (1962).
- [27] K. Huang. *Bose-Einstein Condensation* chapter 3. Cambridge University Press, Cambridge (1995).
- [28] N. D. Mermin and H. Wagner. *Absence of ferromagnetism or antiferromagnetism in one- or two-dimensional isotropic Heisenberg models.* *Phys. Rev. Lett.* **17**, 1133–1136 (1966).
- [29] P. C. Hohenberg. *Existence of long-range order in one and two dimensions.* *Phys. Rev.* **158**, 383–386 (1967).
- [30] J. M. Kosterlitz and D. J. Thouless. *Ordering, metastability and phase transitions in two-dimensional systems.* *Journal of Physics C: Solid State Physics* **6**, 1181–1203 (1973).
- [31] V. Bagnato, D. E. Pritchard, and D. Kleppner. *Bose-Einstein condensation in an external potential.* *Phys. Rev. A* **35**, 4354–4358 (1987).

- [32] W. Ketterle and N. J. van Druten. *Bose-Einstein condensation of a finite number of particles trapped in one or three dimensions*. Phys. Rev. A **54**, 656–660 (1996).
- [33] M. Olshanii. *Atomic scattering in the presence of an external confinement and a gas of impenetrable bosons*. Phys. Rev. Lett. **81**, 938 (1998).
- [34] D. S. Petrov, G. V. Shlyapnikov, and J. T. M. Walraven. *Regimes of quantum degeneracy in trapped 1D gases*. Phys. Rev. Lett. **85**, 3745–3749 (2000).
- [35] E. H. Lieb and W. Liniger. *Exact analysis of an interacting Bose gas. I. the general solution and the ground state*. Phys. Rev. **130**, 1605 (1963).
- [36] C. N. Yang and C. P. Yang. *Thermodynamics of a one-dimensional system of bosons with repulsive delta-function interaction*. J. Math. Phys. **10**, 1115 (1969).
- [37] V. E. Korepin, N. M. Bogoliubov, and A. G. Izergin. *Quantum Inverse Scattering Method and Correlation Functions*. Cambridge University Press, Cambridge, England (1993).
- [38] M. Takahashi. *Thermodynamics of One-Dimensional Solvable Models*. Cambridge University Press, Cambridge, England (1999).
- [39] A. Görlitz *et al.* *Realization of Bose-Einstein condensates in lower dimensions*. Phys. Rev. Lett. **87**, 130402 (2001).
- [40] F. Schreck *et al.* *Quasipure Bose-Einstein condensate immersed in a Fermi sea*. Phys. Rev. Lett. **87**, 080403 (2001).
- [41] M. Greiner *et al.* *Exploring phase coherence in a 2D lattice of Bose-Einstein condensates*. Phys. Rev. Lett. **87**, 160405 (2001).
- [42] B. Paredes *et al.* *Tonks-Girardeau gas of ultracold atoms in an optical lattice*. Nature **429**, 277–281 (2004).
- [43] T. Kinoshita, T. Wenger, and D. S. Weiss. *Observation of a one-dimensional Tonks-Girardeau gas*. Science **305**, 1125–1128 (2004).
- [44] W. Hänsel, P. Hommelhoff, T. W. Hänsch, and J. Reichel. *Bose-Einstein condensation on a microelectronic chip*. Nature **413**, 498–501 (2001).
- [45] H. Ott *et al.* *Bose-Einstein condensation in a surface microtrap*. Phys. Rev. Lett. **87**, 230401 (2001).
- [46] A. van Amerongen *et al.* *Yang-Yang thermodynamics on an atom chip*. Phys. Rev. Lett. **100**, 90402 (2008).
- [47] J. D. Weinstein and K. G. Libbrecht. *Microscopic magnetic traps for neutral atoms*. Phys. Rev. A **52**, 4004–4009 (1995).

- [48] J. Fortágh and C. Zimmermann. *Magnetic microtraps for ultracold atoms*. Rev. Mod. Phys. **79**, 235 (2007).
- [49] R. Gerritsma *et al.* *Atoomchips*. Ned. tijdschr. v. Natuurk. **74**, 82 (2008).
- [50] T. Schumm *et al.* *Matter-wave interferometry in a double well on an atom chip*. Nature Phys. **1**, 57–62 (2005).
- [51] J. J. P. van Es *et al.* *Three-dimensional character of atom-chip-based rf-dressed potentials*. arXiv **cond-mat**, 0802.0362v1 (2008).
- [52] R. Gerritsma *et al.* *Lattice of microtraps for ultracold atoms based on patterned magnetic films*. Phys. Rev. A **76**, 033408 (2007).
- [53] M. D. Girardeau. *Relationship between systems of impenetrable bosons and fermions in one dimension*. J. Math. Phys. **1**, 516 (1960).
- [54] E. H. Lieb. *Exact analysis of an interacting Bose gas. II. the excitation spectrum*. Phys. Rev. **130**, 1616–1624 (1963).
- [55] H. Bethe. *Zur theory der metalle*. Zeitschrift für Physik **71**, 205 (1931).
- [56] B. Laburthe Tolra *et al.* *Observation of reduced three-body recombination in a correlated 1D degenerate Bose gas*. Phys. Rev. Lett. **92**, 190401 (2004).
- [57] T. Kinoshita, T. Wenger, and D. S. Weiss. *Local pair correlations in one-dimensional Bose gases*. Phys. Rev. Lett. **95**, 190406 (2005).
- [58] T. Kinoshita, T. Wenger, and D. S. Weiss. *A quantum newton’s cradle*. Nature **440**, 900–903 (2006).
- [59] K. V. Kheruntsyan, D. M. Gangardt, P. D. Drummond, and G. V. Shlyapnikov. *Pair correlations in a finite-temperature 1D Bose gas*. Phys. Rev. Lett. **91**, 040403 (2003).
- [60] J.-B. Trebbia, J. Estève, C. I. Westbrook, and I. Bouchoule. *Experimental evidence for the breakdown of a Hartree-Fock approach in a weakly interacting Bose gas*. Phys. Rev. Lett. **97**, 250403 (2006).
- [61] E. Arimondo, M. Inguscio, and P. Violino. *Experimental determinations of the hyperfine structure in the alkali atoms*. Rev. Mod. Phys. **49**, 31–75 (1977).
- [62] C. Pethick and H. Smith. *Bose-Einstein Condensation in Dilute Gases*. Cambridge University Press, Cambridge (2002).
- [63] D. Steck. *Rubidium 87 D line data*. Los Alamos National Laboratories Report No. LA-UR-03-8638 2003.
- [64] V. V. Vladimírski. Zh. Eksp. Teor. Fiz. **39**, 1062 [Sov. Phys. JETP **12**, 740 (1961)] (1960).

- [65] D. E. Pritchard. *Cooling neutral atoms in a magnetic trap for precision spectroscopy*. Phys. Rev. Lett. **51**, 1336–1339 (1983).
- [66] J. Luiten. *Lyman- α spectroscopy of magnetically trapped atomic hydrogen*. PhD thesis Universiteit van Amsterdam (1993).
- [67] K. Huang. *Statistical mechanics*. John Wiley & sons New York 2nd edition (1987).
- [68] S. R. de Groot, G. J. Hooyman, and C. A. ten Seldam. *On the Bose-Einstein condensation*. Proc. R. Soc. London Ser. A **203**, 266 (1950).
- [69] V. Bagnato and D. Kleppner. *Bose-Einstein condensation in low-dimensional traps*. Phys. Rev. A **44**, 7439–7441 (1991).
- [70] K. V. Kheruntsyan, D. M. Gangardt, P. D. Drummond, and G. V. Shlyapnikov. *Finite-temperature correlations and density profiles of an inhomogeneous interacting one-dimensional Bose gas*. Phys. Rev. A **71**, 053615 (2005).
- [71] N. Bogoliubov. J. Phys. **11**, 23 (1947). (Moscow).
- [72] E. G. M. van Kempen, S. J. J. M. F. Kokkelmans, D. J. Heinzen, and B. J. Verhaar. *Interisotope determination of ultracold rubidium interactions from three high-precision experiments*. Phys. Rev. Lett. **88**, 093201 (2002).
- [73] C. Menotti and S. Stringari. *Collective oscillations of a one-dimensional trapped Bose-Einstein gas*. Phys. Rev. A **66**, 043610 (2002).
- [74] F. Gerbier. *Quasi-1D Bose-Einstein condensates in the dimensional crossover regime*. Europhys. Lett. **66**, 771–777 (2004).
- [75] C. Menotti. numerical data available online from the following url: http://bec.science.unitn.it/data/data_3D_1D.txt.
- [76] D. S. Petrov, D. M. Gangardt, and G. V. Shlyapnikov. *Low-dimensional trapped gases*. J. Phys. IV (France) **116**, 5 (2004).
- [77] D. S. Petrov, G. V. Shlyapnikov, and J. T. M. Walraven. *Phase-fluctuating 3D Bose-Einstein condensates in elongated traps*. Phys. Rev. Lett. **87**, 050404 (2001).
- [78] P. de Gennes. *Superconductivity of Metals and Alloys*. Benjamin New York (1966).
- [79] V. N. Popov. Sov. Phys. JETP **20**, 1185 (1965).
- [80] V. N. Popov. *Functional Integrals in Quantum Field Theory and Statistical Physics*. Reidel Dordrecht, The Netherlands (1983).
- [81] A. Lenard. *Momentum distribution in the ground state of the one-dimensional system of impenetrable bosons*. J. Math. Phys. **5**, 930 (1964).

- [82] H. G. Vaidya and C. A. Tracy. *One-particle reduced density matrix of impenetrable bosons in one dimension at zero temperature*. Phys. Rev. Lett. **42**, 3–6 (1979).
- [83] H. G. Vaidya and C. A. Tracy. *One-particle reduced density matrix of impenetrable bosons in one dimension at zero temperature*. Phys. Rev. Lett. **43**, 1540 (1979).
- [84] J.-S. Caux and P. Calabrese. *Dynamical density-density correlations in the one-dimensional Bose gas*. Phys. Rev. A **74**, 031605 (2006).
- [85] I. Bouchoule, K. V. Kheruntsyan, and G. V. Shlyapnikov. *Interaction-induced crossover versus finite-size condensation in a weakly interacting trapped one-dimensional Bose gas*. Phys. Rev. A **75**, 031606 (2007).
- [86] M. Naraschewski and D. M. Stamper-Kurn. *Analytical description of a trapped semi-ideal Bose gas at finite temperature*. Phys. Rev. A **58**, 2423–2426 (1998).
- [87] V. V. Goldman, I. F. Silvera, and A. J. Leggett. *Atomic hydrogen in an inhomogeneous magnetic field: Density profile and Bose-Einstein condensation*. Phys. Rev. A **24**, 2870–2873 (1981).
- [88] P. Öhberg and S. Stenholm. *A Hartree Fock study of a Bose condensed gas*. J. Phys. B **30**, 2749 (1997).
- [89] F. Gerbier *et al.* *Experimental study of the thermodynamics of an interacting trapped Bose-Einstein condensed gas*. Phys. Rev. A **70**, 013607 (2004).
- [90] F. D. M. Haldane. *Effective harmonic-fluid approach to low-energy properties of one-dimensional quantum fluids*. Phys. Rev. Lett. **47**, 1840–1843 (1981).
- [91] F. Haldane. *Demonstration of the Luttinger liquid character of Bethe-ansatz-soluble models of 1-D quantum fluids*. Phys. Lett. A **81**, 153 (1981).
- [92] F. Haldane. *Luttinger liquid theory of one-dimensional quantum fluids: I. properties of the Luttinger model and their extension to the general 1D interacting spinless Fermi gas*. J. Phys. C: Solid State Phys. **14**, 2585 (1981).
- [93] F. D. M. Haldane. *Effective harmonic-fluid approach to low-energy properties of one-dimensional quantum fluids*. Phys. Rev. Lett. **47**, 1840–1843 (1981).
- [94] M. A. Cazalilla. *Bosonizing one-dimensional cold atomic gases*. Journal of Physics B: AMOP **37**, S1–S47 (2004).
- [95] A. A. Burkov, M. D. Lukin, and E. Demler. *Decoherence dynamics in low-dimensional cold atom interferometers*. Phys. Rev. Lett. **98**, 200404 (2007).
- [96] S. Hofferberth *et al.* *Non-equilibrium coherence dynamics in one-dimensional Bose gases*. Nature **449**, 324 (2007).

- [97] O. J. Luiten, M. W. Reynolds, and J. T. M. Walraven. *Kinetic theory of the evaporative cooling of a trapped gas*. Phys. Rev. A **53**, 381–389 (1996).
- [98] J. Walraven. *Atomic hydrogen in magnetostatic traps*. In G.-L. Oppo, S. Barnett, E. Riis, and M. Wilkinson, editors, *Quantum dynamics of symple systems* volume 44 of *SUSSP Proceedings* Bristol (1996). IOP.
- [99] W. Ketterle and N. J. van Druten. *Evaporative cooling of trapped atoms*. Advances in Atomic, Molecular and Optical Physics **37**, 181–236 (1996).
- [100] P. W. H. Pinkse *et al.* *One-dimensional evaporative cooling of magnetically trapped atomic hydrogen*. Phys. Rev. A **57**, 4747–4760 (1998).
- [101] J. Reichel. *Microchip traps and Bose-Einstein condensation*. Appl. Phys. B **75**, 469–487 (2002).
- [102] A. Kasper *et al.* *A Bose-Einstein condensate in a microtrap*. J. Opt. B **5**, S143–S149 (2003).
- [103] K. Dieckmann. *Bose-Einstein Condensation with High Atom Number in a Deep Magnetic Trap*. PhD thesis Universiteit van Amsterdam (2001).
- [104] M. A. Joffe, W. Ketterle, A. Martin, and D. E. Pritchard. *Transverse cooling and deflection of an atomic beam inside a Zeeman slower*. J. Opt. Soc. Am. B **10**, 2257 (1993).
- [105] Z. T. Lu *et al.* *Low-velocity intense source of atoms from a magneto-optical trap*. Phys. Rev. Lett. **77**, 3331–3334 (1996).
- [106] K. Dieckmann, R. J. C. Spreeuw, M. Weidemüller, and J. T. M. Walraven. *Two-dimensional magneto-optical trap as a source of slow atoms*. Phys. Rev. A **58**, 3891–3895 (1998).
- [107] M. Greiner, I. Bloch, T. W. Hänsch, and T. Esslinger. *Magnetic transport of trapped cold atoms over a large distance*. Phys. Rev. A **63**, 031401 (2001).
- [108] H. J. Lewandowski, D. M. Harber, D. L. Whitaker, and E. A. Cornell. *Simplified system for creating a Bose-Einstein condensate*. J. Low Temp. Phys. **132**, 309–367 (2003).
- [109] J. Fortágh, A. Grossmann, T. W. Hänsch, and C. Zimmermann. *Fast loading of a magneto-optical trap from a pulsed thermal source*. J. Appl. Phys **84**, 6499–6501 (1998).
- [110] B. P. Anderson and M. A. Kasevich. *Loading a vapor-cell magneto-optic trap using light-induced atom desorption*. Phys. Rev. A **63**, 023404 (2001).
- [111] J. Reichel, W. Hänsel, and T. W. Hänsch. *Atomic micromanipulation with magnetic surface traps*. Phys. Rev. Lett. **83**, 3398–3401 (1999).

- [112] H. J. Metcalf and P. van der Straten. *Laser Cooling and Trapping of Neutral Atoms*. Springer New York (1999).
- [113] E. Eliel. Huygens Laboratory, Leiden, The Netherlands.
- [114] S. Du *et al.* *Atom-chip Bose-Einstein condensation in a portable vacuum cell*. Phys. Rev. A **70**, 053606 (2004).
- [115] J. J. P. van Es. PhD thesis Universiteit van Amsterdam (2008).
- [116] J. Reichel, W. Hänsel, P. Hommelhoff, and T. W. Hänsch. *Applications of integrated magnetic microtraps*. Appl. Phys. B **72**, 81–89 (2001).
- [117] E. Hennes. *Thermal properties of the atom chip assembly*. Technical report University of Amsterdam (2006).
- [118] E. Kreyszig. *Advanced Engineering Mathematics*. John Wiley & Sons, Inc. New York (1993).
- [119] S. Groth *et al.* *Atom chips: Fabrication and thermal properties*. Appl. Phys. Lett. **85**, 2980–2982 (2004).
- [120] M. Succi, R. Canino, and B. Ferrario. *Atomic absorption evaporation flow rate measurements of alkali metal dispensers*. Vacuum **35**, 579 (1985).
- [121] C. Klempt *et al.* *Ultraviolet light-induced atom desorption for large rubidium and potassium magneto-optical traps*. Phys. Rev. A **73**, 013410 (2006).
- [122] Ralchenko *et al.* *NIST atomic spectra database (version 3.1.2)*. Online: <http://physics.nist.gov/asd3> 2007.
- [123] G. C. Bjorklund, M. D. Levenson, W. Lenth, and C. Ortiz. *Frequency modulation (FM) spectroscopy; theory of lineshapes and signal-to-noise analysis*. Appl. Phys. B **32**, 145 (1983).
- [124] A. E. Siegman. *Lasers*. University Science Books Mill Valley, California (1986).
- [125] W. Petrich, M. H. Anderson, J. R. Ensher, and E. A. Cornell. *Behavior of atoms in a compressed magneto-optical trap*. J. Opt. Soc. Am. B **11**, 1332–1335 (1994).
- [126] S. Wildermuth *et al.* *Optimized magneto-optical trap for experiments with ultracold atoms near surfaces*. Phys. Rev. A **69**, 030901 (2004).
- [127] I. Shvarchuck *et al.* *Bose-Einstein condensation into nonequilibrium states studied by condensate focusing*. Phys. Rev. Lett. **89**, 270404 (2002).
- [128] D.-W. Wang, M. D. Lukin, and E. Demler. *Disordered Bose-Einstein condensates in quasi one-dimensional magnetic microtraps*. Phys. Rev. Lett. **92**, 076802 (2004).

- [129] J. Estève *et al.* *The role of wire imperfections in micro magnetic traps for atoms.* Phys. Rev. A **70**, 043629 (2004).
- [130] P. Krueger *et al.* *Disorder potentials near lithographically fabricated atom chips.* arXiv:cond-mat/0504686 v1 (2005).
- [131] J.-B. Trebbia *et al.* *Roughness suppression via rapid current modulation on an atom chip.* Phys. Rev. Lett. **98**, 263201 (2007).
- [132] N. Ramsey. *Molecular beams.* Oxford university Press (1956).
- [133] H. Friedburg and W. Paul. Naturwissenschaften **38**, 159 (1951).
- [134] H. Friedburg. *Optische abbildung mit neutralen atomen.* Z. Phys. **130**, 493 (1951).
- [135] V. I. Balykin and V. S. Letokhov. *The possibility of deep laser focusing of an atomic beam into the A-region.* Opt. Commun. **64**, 151–156 (1987).
- [136] V. I. Balykin, V. S. Letokhov, Y. B. Ovchinnikov, and A. I. Sidorov. *Quantum-state-selective mirror reflection of atoms by laser light.* Phys. Rev. Lett. **60**, 2137–2140 (1988).
- [137] R. J. C. Spreeuw, D. Voigt, B. T. Wolschrijn, and H. B. van Linden van den Heuvell. *Creating a low-dimensional quantum gas using dark states in an inelastic evanescent-wave mirror.* Phys. Rev. A **61**, 053604 (2000).
- [138] B. T. Wolschrijn *et al.* *Stochastic rainbow caustic observed with cold atoms.* Phys. Rev. A **64**, 065403 (2001).
- [139] M.-O. Mewes *et al.* *Output coupler for Bose-Einstein condensed atoms.* Phys. Rev. Lett. **78**, 582–585 (1997).
- [140] B. P. Anderson and M. Kasevich. *Macroscopic quantum interference from atomic tunnel arrays.* Science **282**, 1686 (1998).
- [141] E. W. Hagley *et al.* *A well-collimated quasi-continuous atom laser.* Science **283**, 1706 (1999).
- [142] I. Bloch, T. W. Hänsch, and T. Esslinger. *Atom laser with a cw output coupler.* Phys. Rev. Lett. **82**, 3008–3011 (1999).
- [143] I. Bloch *et al.* *Optics with an atom laser beam.* Phys. Rev. Lett. **87**, 030401 (2001).
- [144] Y. Le Coq *et al.* *Atom laser divergence.* Phys. Rev. Lett. **87**, 170403 (2001).
- [145] F. Gerbier, P. Bouyer, and A. Aspect. *Quasicontinuous atom laser in the presence of gravity.* Phys. Rev. Lett. **86**, 4729–4732 (2001).

- [146] J. F. Riou *et al.* *Beam quality of a nonideal atom laser*. Phys. Rev. Lett. **96**, 070404 (2006).
- [147] W. Guerin *et al.* *Guided quasicontinuous atom laser*. Phys. Rev. Lett. **97**, 200402 (2006).
- [148] J.-F. Riou. *Étude des propriétés de propagation d'un laser à atomes*. PhD thesis Université Paris-sud XI (2006).
- [149] C. J. Bordé. *Fundamental Systems in Quantum Optics, Les Houches* chapter Session LIII, p. 287. Elsevier Science Publishers B. V. (1990).
- [150] C. Bordé. *Theoretical tools for atom optics and interferometry*. Comptes Rendus de l'Académie des Sciences - Series IV - Physics **2**, 509 (2001).
- [151] J. Clauser. *Ultra-high sensitivity accelerometers and gyroscopes using neutral atom matter-wave interferometry*. Physica B+C **1-2**, 265 (1988).
- [152] D. W. Keith, C. R. Ekstrom, Q. A. Turchette, and D. E. Pritchard. *An interferometer for atoms*. Phys. Rev. Lett. **66**, 2693–2696 (1991).
- [153] C. Buggle. *Collective and Collisional Properties of the Rubidium Quantum Gas*. PhD thesis University of Amsterdam (2005).
- [154] M. J. Bastiaans. *The Wigner distribution function applied to optical signals and systems*. Opt. Commun. **25**, 26 (1978).
- [155] M. Bastiaans. *Propagation laws for the 2nd-order moments of the Wigner distribution function in 1st-order optical-systems*. Optik **82**, 173–181 (1989).
- [156] Y. Castin and R. Dum. *Bose-Einstein condensates in time dependent traps*. Phys. Rev. Lett. **77**, 5315–5319 (1996).
- [157] Y. Kagan, E. L. Surkov, and G. V. Shlyapnikov. *Evolution of a Bose-condensed gas under variations of the confining potential*. Phys. Rev. A **54**, R1753–R1756 (1996).
- [158] Y. Kagan, E. L. Surkov, and G. V. Shlyapnikov. *Evolution of a Bose gas in anisotropic time-dependent traps*. Phys. Rev. A **55**, R18–R21 (1997).
- [159] A. Siegman. *Defining the effective radius of curvature for a nonideal optical beam*. IEEE J. Quant. Electron. **27**, 1146 (1991).
- [160] P. A. Bélanger. *Beam propagation and the ABCD ray matrices*. Opt. Lett. **16**, 196 (1991).
- [161] F. J. Pedrotti and L. S. Pedrotti. *Introduction to optics*. Prentice-Hall Englewood Cliffs, New Jersey second edition edition (1993).
- [162] G. Brooker. *Modern Classical Optics*. Oxford University Press Oxford (2003).

- [163] E. Wigner. *On the quantum correction for thermodynamic equilibrium*. Phys. Rev. **40**, 749–759 (1932).
- [164] K. Imre, E. Özizmir, M. Rosenbaum, and P. F. Zweifel. *Wigner method in quantum statistical mechanics*. J. Math. Phys. **8**, 1097 (1967).
- [165] L. Mandel and E. Wolf. *Optical coherence and quantum optics*. Cambridge university press (1995).
- [166] V. Namias. *The fractional order Fourier transform and its application to quantum mechanics*. IMA J. Appl. Math. **25**, 241 (1980).
- [167] D. Mendlovic and H. M. Ozaktas. *Fractional Fourier transforms and their optical implementation: I*. J. Opt. Soc. Am. **10**, 1875 (1993).
- [168] A. W. Lohmann. *Image rotation, Wigner rotation, and the fractional Fourier transform*. J. Opt. Soc. Am. **10**, 2181 (1993).
- [169] F. Gerbier *et al.* *Momentum distribution and correlation function of quasicondensates in elongated traps*. Phys. Rev. A **67**, 051602(R) (2003).
- [170] L. Pitaevskii. *Bose-Einstein condensation in magnetic traps. Introduction to the theory*. Phys. Usp. **41**, 569 (1998).
- [171] S. Dettmer *et al.* *Observation of phase fluctuations in elongated Bose-Einstein condensates*. Phys. Rev. Lett. **87**, 160406 (2001).
- [172] S. Richard *et al.* *Momentum spectroscopy of 1D phase fluctuations in Bose-Einstein condensates*. Phys. Rev. Lett. **91**, 010405 (2003).
- [173] M. Hugbart *et al.* *Coherence length of an elongated condensate*. Eur. Phys. J. D **35**, 155 (2005).
- [174] M. J. Bastiaans and K. B. Wolf. *Phase reconstruction from intensity measurements in linear systems*. J. Opt. Soc. Am. A **20**, 1046 (2003).
- [175] K. A. Nugent and D. Paganin. *Matter-wave phase measurement: A noninterferometric approach*. Phys. Rev. A **61**, 063614 (2000).
- [176] C. Paré and P. A. Bélanger. *Beam propagation in a linear or nonlinear lens-like medium using ABCD ray matrices: the method of moments*. Opt. & Quant. Electr. **24**, S1051 (1992).
- [177] F. Impens and C. J. Bordé. *Generalized ABCD propagation for interacting atomic clouds*. arXiv:0709.3381v2 [cond-mat.other] (2007).
- [178] H. Moritz, T. Stöferle, M. Köhl, and T. Esslinger. *Exiting collective oscillations in a trapped 1D gas*. Phys. Rev. Lett. **91**, 250402 (2003).
- [179] J. O. Andersen, U. Al Khawaja, and H. T. C. Stoof. *Phase fluctuations in atomic Bose gases*. Phys. Rev. Lett. **88**, 070407 (2002).

- [180] G. E. Astrakharchik and S. Giorgini. *Quantum Monte Carlo study of the three-to one-dimensional crossover for a trapped Bose gas*. Phys. Rev. A **66**, 053614 (2002).
- [181] M. A. Cazalilla. *One-dimensional optical lattices and impenetrable bosons*. Phys. Rev. A **67**, 053606 (2003).

Summary

This thesis describes the study of an ultracold gas of bosonic atoms that is magnetically confined to a one-dimensional (1D) geometry. The confining field is generated with a micro-electronic circuit. This microtrap for atoms or ‘atom chip’ is particularly suited to generate a tight waveguide for atoms close to the chip surface.

Systems of ultracold bosons are interesting because in 3D a phase transition occurs to a Bose-Einstein condensate (BEC) when the sample is cooled to the point where the de Broglie wavelengths are comparable to the average interparticle separation. The quantum-mechanical ground state becomes macroscopically occupied and a BEC is formed that is characterized by long-range phase coherence. This long-range order is the origin of macroscopic phenomena in many-body quantum systems like superconductivity and superfluidity. In 2D and 1D systems, at finite temperature, long-range order is destroyed due to a large population of excited states.

In this thesis we investigate the (coherence) properties of a finite-temperature 1D Bose gas with repulsive interactions. This system is of particular interest because it forms the textbook example for the many-body quantum-mechanical systems that can be exactly solved using the Bethe Ansatz. Moreover, using a method developed by Yang and Yang, exact expressions for the thermodynamics of this system of repulsive bosons in 1D can be given. The method by Yang and Yang is of wide relevance because it is the simplest example for obtaining the thermodynamics of the complete class of exactly solvable models for many-body quantum mechanical systems in 1D, e.g. the Heisenberg spin chain and the Hubbard model.

In experiments described in this thesis we cool a gas of ^{87}Rb that is trapped in a waveguide to a temperature below 160 nK corresponding to the level splitting of the confining potential in the radial direction. Then, the gas of a few thousand atoms is confined to one dimension because radial motion is frozen. We find excellent agreement between measurements of the equation of state of a trapped gas of ^{87}Rb atoms and numerical solutions to the exact Yang-Yang thermodynamics.

In our 1D-gas samples thermally-driven fluctuations of the phase result in a reduced coherence length. The axial momentum distribution is the Fourier transform of the spatial correlation function and can therefore be used as a probe for the coherence in the gas. We use the technique of Bose gas focusing, that is equivalent to the action of a lens in optics, to measure the momentum distribution of the gas in the Fourier plane. This method allows us to probe correlations that go beyond the Yang-Yang description. At the time of writing the first theoretical calculations of the correlations are being performed that can be compared with our experimental observations.

Part of this thesis describes how we have constructed the microtrap for the

realization of BEC and the attainment of the 1D regime. Design considerations and analysis of the thermal properties of the microtrap, when a relatively high current is sent through tiny wires, are presented.

Samenvatting

Dit proefschrift beschrijft het experimentele onderzoek naar een extreem koude gaswolk van atomen. De koude atomen zitten opgesloten in een magneetveld in een vacuümomgeving zodat ze niet in aanraking komen met een warme wand. Voor dit onderzoek ontwikkelden we een miniatuur atoomval; zeer kleine stroomdraden op een chip zorgen voor het benodigde magneetveldminimum vlak boven die chip zoals te zien is in Fig. 1.1 in de inleiding. Deze ‘atoomchip’ maakt het mogelijk een langwerpige atoomwolk zo strak samen te knijpen dat er een lijn van atomen ontstaat: een eendimensionaal gas op een chip.

Als we materie afkoelen tot dicht bij het absolute nulpunt in temperatuur, -273°C (of nul Kelvin), kunnen uitzonderlijke verschijnselen optreden. Zo ontdekte Heike Kamerlingh-Onnes al in 1911 in zijn lab in Leiden dat wanneer hij het metaal kwik tot 4 K afkoelde een elektrische stroom door het kwik geen weerstand meer ondervond. Hij noemde het fenomeen supergeleiding. Ook bleek aan het eind van de jaren dertig dat vloeibaar helium dat tot 2 K is afgekoeld stroomt zonder enige frictie; het wordt supervloeibaar. In de loop van de twintigste eeuw is duidelijk geworden dat deze “super” fenomenen verklaard kunnen worden met behulp van een theorie die in 1924 werd geformuleerd. In dat jaar ontdekte Albert Einstein dat een zeer koud gas van bosonen (deeltjes met heeltallige spin) een fase overgang kan doormaken naar een Bose-Einstein condensaat (BEC). Atomen in zo’n condensaat gedragen zich als golven. Deze golven worden beschreven door de quantummechanica. Omdat in het BEC alle atoomgolven samen vallen (coherent zijn) kun je zeggen dat er een superatoom ontstaat. Zo’n superatoom werd voor het eerst gezien in twee labs in de VS in 1995. Je kunt een BEC, ter grootte van een tiende millimeter, afbeelden met een geavanceerde camera. De wereld van de natuurkundigen stond op zijn kop. Meer dan tien jaar later zijn er meer dan 50 labs over de hele wereld waar Bose-Einstein condensaten gemaakt worden. In ons Amsterdamse lab op de vijfde verdieping recht boven het water van de Nieuwe Achtergracht maakten we in 2006, na drie en een half jaar bouwen aan de opstelling, ons eerste Bose-Einstein condensaat. We gebruikten hiervoor de vernieuwende atoomchip techniek.

In de experimenten die beschreven worden in dit proefschrift maken we een extreem koud gas van ongeveer tienduizend atomen. Het gaswolkje is opgesloten in een langgerekte magneetval op de genoemde atoomchip, de wolk is ongeveer 0.2 mm lang en heeft een diameter van slechts 0.0004 mm. Het gas bestaat uit atomen van het metaal rubidium dat vergelijkbaar is met natrium dat bijvoorbeeld zorgt voor het gele licht uit de lampen boven de snelweg. We koelen het rubidium gas af tot een temperatuur beneden 160 nK (honderdzestig miljardste Kelvin). Bij die temperatuur hebben de atomen te weinig energie om te kunnen bewegen in de richting van strakke opsluiting van de val en kunnen ze alleen nog maar vrij bewegen

langs de as, hierdoor ontstaat effectief een eendimensionaal (1D) gas.

Dit proefschrift beschrijft vervolgens onze studie naar de eigenschappen van het extreem koude, eendimensionale gas. Het gas gedraagt zich in 1D anders dan in drie dimensies, waar je een geheel coherent BEC hebt, omdat in 1D trillingen langs de as de coherentie van de wolk verstoren. Het Bose gas in 1D is extra bijzonder omdat, alleen in 1D, het quantum-mechanisch gedrag van alle atomen in het gas exact te berekenen is. Zo laten we voor het eerst zien dat experimentele waarnemingen goed overeen komen met exacte berekeningen vanuit theorie die al in 1969 was ontwikkeld door de Nobelprijswinnaar C.N. Yang en zijn broer C.P. Yang.

Het bestuderen van de (gereduceerde) coherentie in 1D is interessant omdat deze coherentie juist het essentiële ingrediënt is voor de “super” fenomenen zoals supervloeibaarheid en supergeleiding in systemen die met behulp van de theorie van Bose en Einstein beschreven worden. Als we het 1D gas beter begrijpen leidt dat misschien tot een beter inzicht in het complexe gedrag van veel (gedeeltelijk) coherente deeltjes in hogere dimensies.

We maken in onze experimenten gebruik van de directe analogie tussen lichtgolven zoals die beschreven worden in de klassieke optica en de materiegolven van de quantum-mechanica. Om de coherentie in onze langgerekte gaswolken te bepalen gebruiken we een truc uit de optica: we focuseren onze materiegolf en meten de breedte in het focus; hoe breder het focus hoe minder coherentie. Op deze manier kunnen we extra informatie over het 1D gas krijgen die niet uit de Yang-Yang theorie komt.

Een groot deel van het werk dat ten grondslag ligt aan dit proefschrift bestond uit het bouwen van een *state of the art* experimentele opstelling. Het meest innovatieve onderdeel daarvan is onze specifieke manier om de atoomchip te maken en te combineren met dunne draadjes (0.3 mm doorsnede) onder de chip. We beschrijven hier hoe we deze micro-atoomval ontwierpen en bouwden.

Nawoord

Veel mensen in het Van der Waals-Zeeman instituut en daarbuiten hebben op vele manieren bijgedragen aan het onderzoek waarvan dit proefschrift het verslag is. Op deze plaats wil ik al die mensen bedanken.

En passant, hoorde ik van Robert in de nazomer van 2002 dat Klaasjan naar de UvA zou komen en nog een promovendus zocht voor zijn nieuwe project. Daarnaast zou Jook met zijn groep terugkomen naar het WZI om de Quantum gassen groep te versterken. Met in de ene hand een recent artikel, waarin handige Duitsers beschrijven hoe ze voor het eerst een BEC op een chip maakten, en in de andere hand de Vidi beurs wist Klaasjan direct mijn interesse te wekken: dat konden wij ook; en wel binnen een jaar Tijdens de eerste voortgangsbespreking leidde deze ambitie tot een glimlach op het gezicht van Jook, die ons overigens wijselijk in de waan liet. In de lente van 2006, na drie en een half jaar non stop bouwen en experimenteren, zouden we ons eerste BEC op een chip maken.

Ten eerste wil ik Klaasjan bedanken, voor het grote vertrouwen dat hij in mij stelde bij het ontwerp en de bouw van het experiment. En zeker ook voor de consciëntieuze manier waarop hij mij opleidde als natuurkundige, met oog voor detail. Jook wil ik bedanken voor zijn uitstekende supervisie. Met enthousiaste en welgemikte vragen legde hij de kern bloot van de problemen waarmee wij worstelden. Of het nu de verdeling van bosonen betrof of een trillingsdempende kunststof. Jan-Joris schreef de *software for atom chips* (en bleef schijnbaar ongestoord ondanks mijn onophoudelijke vragen om “een kleine verbetering”), ook fabriceerde hij de chips (niet alleen nummer 94) en de geavanceerde RF bron waarmee het experimentele apparaat uiteindelijk groeide tot een gesmeerde machine. Leuk ook om een aantal “van Es” clean-room kneepjes te kunnen leren. Philipp wens ik veel succes met het doen van nieuwe experimenten (zonder al te veel te hoeven bouwen).

Praktisch alles over diodelasers en hoe je daarmee atomen koelt leerde ik tijdens mijn afstuderen van Ronald. Ik had de mazzel dat hij ook nog de *hands-on* kennis van Dirk Voigt, Bas Wolschrijn, Rik Jansen, Nandini Bhattacharya, en degenen die voor hen kwamen aan mij doorgaf. Mijn fascinatie voor het vakgebied is absoluut gewekt, tijdens de bijeenkomsten van de kletsclub (om met Cor te spreken). Ik mocht meedoen met het gesprek tussen de generaties wetenschappers die de ideale onderzoeksschool vormden, comfortabel gezeten tussen Flateriaanse stapels papierwerk in de ruime (pre asbest) professors kamer van Ben. Ik wil Ben en Robert bedanken voor het bieden van een omgeving op topniveau zonder pretenties. Cor, in het leer gestoken rondscheurend op een zware motor, verloor nooit de bravoure van de natuurkunde van de jaren vijftig. Ook ontsloot hij het zware houten kabinet zodat ik nog een Babinet-Soleil compensator op een neoklassiek voetstuk, van de oude Zeeman zelf, heb kunnen gebruiken voor een spectroscopie experiment (helaas

bleken de oppervlakken niet vlak genoeg voor laserlicht).

Het tweelingexperiment dat met een vergelijkbaar doel als het onze werd opgebouwd aan de andere zijde van een zwaar gordijn in dezelfde labruimte C5.13 vormde de afgelopen jaren een belangrijke stimulans. *Many thanks for the companionship to Iuliana, René, Thomas en Shannon. Further thanks for Vlad, the stoical warrior in the freezing lab with the big lasers.* De jongens van de werkplaats, waar ik maanden heb doorgebracht, leverden een cruciale bijdrage aan de experimentele opstelling. Onder andere droegen bij: Harry, Fred, Diederik, Joost, Cees en bovenal Wim, die met zijn precisie het Leidse instrumentmakers ambacht wist te koppelen aan de eisen van de nanotechnologie. In de elektronische werkplaats bedank ik in het bijzonder Hans en het onafscheidbare duo Johan en Alof. In het constructie bureau tekenden Ron en Hans sneller dan ik met nieuwe ideetjes kwam terwijl Eric de thermische analyse van de atoomchip deed. In de voetsporen van Bert Zwart, doolde ik door ongekende ruimtes en daalde ik af langs geheime trappen in de kelders van het instituut. Op zoek naar de juiste flens of een (op een koopje van Philips overgenomen) flowkast. Paul Vlaanderen, ik denk met plezier terug aan mijn jaren als practicum assistent. Op het practicum maakte ik later ook kennis met de verfrissende experimenten van Tom Hijmans die ik al waardeerde om zijn ongezouten kritiek op maffiose onderzoeksclans of hele vakgebieden die, naar zijn mening, onzin produceren.

I would like to acknowledge the collaboration with the theory section of the Quantum Gases Group: Dima Petrov, Micha Baranov and Gora Shlyapnikov thanks for clear and sure answers to all theory related questions. Many thanks to Karen Kheruntsyan for the nice collaboration over the last year that culminated in the Yang-Yang article. Jean-Sébastien Caux wil ik bedanken voor de introductie in de exact oplosbare wereld die hij Klaasjan en mij gaf (met 300 km/u richting Parijs snellend). Ik bedank Wim Vassen en alle leden van zijn groep voor de goede discussies tijdens de bijeenkomsten van het *Amsterdam Quantum Collective*. Tobias, die ik de afgelopen jaren vreemd genoeg vooral in het weekend op een feest of in het café sprak, wil ik veel succes wensen met zijn kunststuk. Dank aan de andere afstudeerders, promovendi, postdocs en gasten met wie ik in de loop der jaren samenwerkte: Tycho Huussen, Paul Cleary, Yu Tao Xing, Steve Gensemer (one day cities will be full of green robotic vehicles), Carolijn van Ditzhuijzen, Antje Ludewig, Sebastian Kraft, Piotr Deuar, Femius Koenderink, Liza Huijze en alle anderen. Mark Golden en Luuk Lusink thanks voor de (financiële) ondersteuning. Dank ook aan Rita Vinig en anderen op het secretariaat. Mirjam “studioboven” Wilbrink verzorgde het omslag ontwerp.

Tenslotte, alle vrienden hartelijk dank; Kanne bedankt; Akke veel dank voor de steun. Helaas kan Jan mijn promotie niet meer meemaken. Van hem leerde ik klussen. Ik heb veel aan hem te danken. Esmee, bedankt voor je eindeloze support, goede raad en liefde, terwijl ik vaak met het experiment in slaap viel, ervan droomde, en er weer mee opstond. Zonder jou was het nooit gelukt.